POWER SYSTEMS RESEARCH AT MSFC

July 27, 1967

By

Richard Acker
Richard J. Boehme
William L. Crabtree
Walter H. Goodhue
Charles B. Graff
Roy Lanier
Jimmy L. Miller
John R. Morgan
Leighton Young

9

INTRODUCTION TO ELECTRICAL POWER SYSTEMS RESEARCH AT MSFC

By Richard J. Boehme

LIST OF ILLUSTRATIONS

ZINC-OXYGEN PRIMARY BATTERY

By Charles B. Graff

LIST OF ILLUSTRATIONS

FUEL CELL SYSTEMS

Page

By Walter H. Goodhue

LIST OF ILLUSTRATIONS

FUEL CELL TECHNOLOGY

Page

By John R. Morgan

LIST OF TABLES

LIST OF ILLUSTRATIONS

CONTENTS (Continued)...

STUDY OF RADIOISOTOPE POWER FOR SATURN APPLICATIONS

By Jimmy L. Miller

LIST OF ILLUSTRATIONS

CONTENTS (Continued) . . .

STUDY OF SOLAR POWER WITH GRAVITY GRADIENT STABILIZATION

By Leighton Young

LIST OF ILLUSTRATIONS

METAL-ARC ILLUMINATOR FOR SOLAR ARRAY TESTING

By William L. Crabtree

CONTENTS (Continued) . . .

LIST OF ILLUSTRATIONS

ELECTRICAL POWER CONVERSION SYSTEM FOR MANNED EARTH ORBITAL VEHICLE

By Richard Acker

LIST OF TABLES

LIST OF ILLUSTRATIONS

CONTENTS (Concluded)...

INVERTERS FOR MOTORS

By Roy Lanier

LIST OF TABLES

LIST OF ILLUSTRATIONS

INTRODUCTION TO ELECTRICAL POWER SYSTEMS RESEARCH AT MSFC

By

Richard J. Boehme

SUMMARY

To successfully complete space vehicle missions, research efforts at the Marshall Space Flight Center (MSFC) have produced significant achievements in developing electrical power systems. Even more stringent mission demands will be imposed on future power systems. This introduction outlines the power systems R&D program, including program effectiveness and organization, and the program planning to assure future success.

PRESENT R&D PROGRAM

The Marshall Center R&D program in electrical power systems has been conducted primarily by the Electrical Systems Division of the Astrionics Laboratory. Emphasis in the past has been on battery systems because they have served as the power workhorse and will see extensive service in the future. Recent efforts have been made to diversify the program without sacrificing effectiveness, and to concentrate on requirements that represent limitations or significant problem areas for future mission systems.

The need for revitalized efforts in developing space power systems was well summarized recently by William Woodward, Acting Director for Nuclear Systems and Space Power, Office of Advanced Research and Technology (OART). In his introductory statement to a Congressional Subcommittee, he said, "Current space power system technology is not yet satisfactory for such future missions as high power communications satellites, science probes and orbiters to distant planets, and for long-duration, manned, earth-orbit, lunar, and planetary missions."

The major part of the MSFC program is sponsored by OART, and R&D work is being performed in support of the MSFC vehicles and study missions. The "Electrolysis Systems" and "Advanced Electrochemical Systems" are new projects in which basic research work has just started.

Previous R&D efforts have been quite successful as shown by the most notable, recent achievement of the technology readiness status reached by the fuel cell system. The remainder of the fuel cell work started in FY 67 will carry the system into a technology utilization and verification phase. This phase of work is being assumed by the Manned Spacecraft Center (MSC) at Houston to adapt the system to their advanced Apollo Applications Program (AAP) missions.

ORGANIZATION

Because of the serious need for advanced technology in power and energy systems, the Power Branch was established under the Electrical Systems Division (Fig. 1) of the Astrionics Laboratory. To emphasize and expand R&D efforts in this critical field, subdivision of the Power Branch has been by

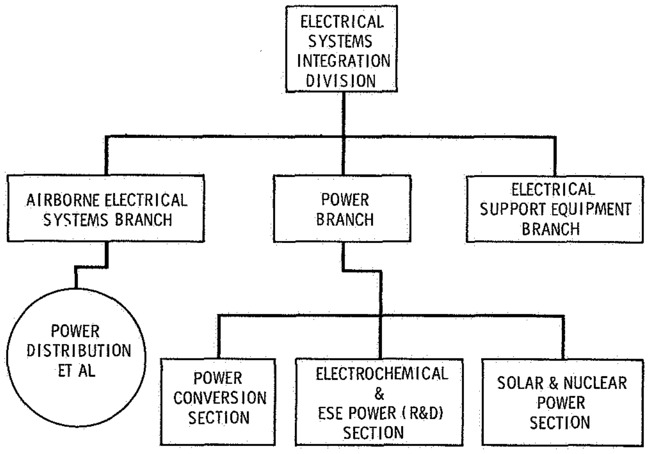

FIGURE 1. ORGANIZATION FOR ELECTRICAL POWER

technical discipline rather than by project. The three sections presently in operation are as follows:

1. The Power Conversion Section
2. The Electrochemical & ESE Power Section
3. The Solar and Nuclear Power Section

Advanced R&D will be performed under the same groups which are responsible for the design and development work for vehicle missions. Program aims are (1) to emphasize R&D in space power, (2) to increase the number of competent persons in the field, and (3) to consolidate efforts and thereby increase the percentage of available resources for advanced R&D.

POWER IN THE FUTURE

Surveys have been made of various future mission requirements for advanced power systems and equipment. Recent technology forecasts by OART and other agencies have also been reviewed. A brief summary of the R&D job to be accomplished for electrical power systems of the future is as follows:

1. Power and energy systems must possess vastly expanded capabilities for successful future space exploration. Large improvements in technology are needed so that the conceptual missions of today will become realities in the next decade. As one example, the requirements in supplying electrical power to electrically propelled vehicles become synonymous with those of generating propulsion power.

2. Improved electrochemical systems will be required for energy storage and short term power. This need extends for several decades.

3. Larger, higher performance solar cell arrays with lighter weight mounting structures are needed. Solar arrays will be used extensively in the next decade for long-duration power. Fifty kilowatt ratings appear quite reasonable for the early 1970 period.

4. Even though technology readiness may be achieved for large nuclear power systems, practical systems will remain in their infancy in the 1970's. Small radioisotope thermoelectric units of several hundred watts will be used extensively. Radioisotope Brayton-Cycle or thermionic systems may find limited application in the later 1970's, but they will be restricted by fuel and installation costs and non-technical factors.

5. The use of large reactor systems in space appears to be reserved for the 1980's. Nuclear systems require better materials, higher conversion efficiencies, and reasonable solutions to thermal dissipation, shielding, and safety constraints.

The MSFC program will be oriented to solving these power systems requirements, especially in the applied research and system integration areas.

PROGRAM ORIENTATION

To support R&D programs coordinated toward one or more common missions, a conceptual mission has been selected as a future baseline toward which most of the power and energy conversion R&D projects will be oriented. Such programing assists in coordinating overall programs and is technically sound, providing that the baseline is properly selected and that a reasonable amount of unconstrained basic research is authorized.

A lunar-surface exploration mission primarily founded on a lunar base concept will serve as the fundamental guide for the power system R&D work. It is assumed that this mission will be established in the mid 1970's for the purpose of conducting extensive lunar surface exploration and scientific investigations. It is further projected that, during the assumed mission, additional programs will be added to evaluate technology, equipment, and capabilities for establishing large, hard bases to support subsequent missions. Thus the lunar surface exploration mission should progressively phase into a hard base mission to provide a permanent lunar installation to sustain continuous operations. As conceived, such missions could (1) permit exploitation of lunar resources, (2) serve as a logistics base for interplanetary exploration, (3) provide expanded, long-term, scientific bases for astronomy, and (4) provide communications relaying and advanced monitoring of space operations. This concept was derived from many studies performed for the government, and the results of these studies will be used extensively in the program. The technology requirements are expected to be quite demanding, and in meeting these demands a capability to fulfill the needs of most any mission expected in the 1970's will be provided.

Figure 2 shows a block diagram of the general system for the selected baseline mission. After a standby mode of up to 6 months, the operation is started upon command through the telemetry station system. A small radioisotope generator (RTG) is used in the secondary power subsystem to provide standby and activation power.

Lunar-surface exploration will begin with the arrival of the base crew and the mobile vehicles. Mobile vehicles powered by H_2/O_2 fuel cells provide the means of exploring vast regions about the base station. These vehicles will carry scientific instruments and geological equipment as well as life support equipment. Initially, the vehicles are furnished with cryogenic reactants, and a means is provided to collect by-product water from the fuel cells during mobile operations. Two week (1 lunar day) sorties have been envisioned and appear feasible. A sortie is completed upon return of the vehicle to the base station for resupply. During resupply, standby electrical power requirements of the vehicles are furnished by the regulation and control subsystem of the base. Reactant loading and unloading of the by-product water from the mobile vehicles are done by base station personnel using the unloading and scavenging equipment in the electrolytic reactants production subsystem. This equipment is also used to receive water from the environmental control system (ECS) and fuel cell systems at the base station. The electrolytic subsystem converts the water to reactants (H_2 and O_2) and delivers gases to liquefaction subsystems or to storage, as required, for reuse. The storage subsystem supplies reactants to reload vehicles and to the base power subsystem to permit fuel cells to operate through the lunar night. The storage subsystem can supply back-up oxygen to the environmental control system of the base or to the vehicles as needed.

Solar arrays sized to 50 kW have been assumed to be available under the lunar equipment primary electrical power system (LEPEPS) to power the base and to operate the electrolysis systems during the lunar day. Later, nuclear reactor power systems could be added to the base complex as a primary power source when expanded operations are desired.

With the requirements for a limited three man base station outlined, investigation continues on the means to expand this station into a complex for a 12 man operation for extended periods.

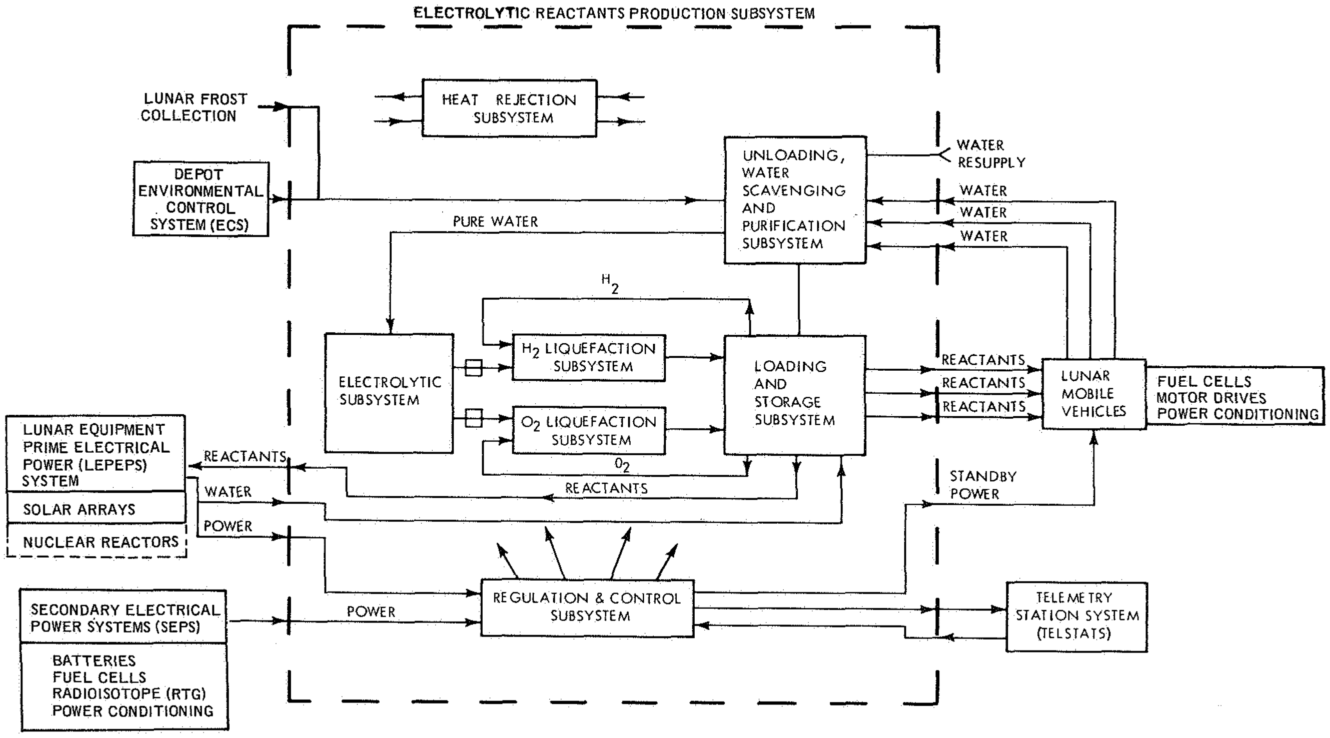

FIGURE 2. SYSTEM FOR R&D BASELINE MISSION

ZINC-OXYGEN PRIMARY BATTERY

By

Charles B. Graff

INTRODUCTION

Development work has been progressing for several years toward a reliable metal-air primary battery system that will be an auxiliary power source in space vehicle applications. One of the most promising systems uses the zinc-oxygen ($Zn - O_2$) battery that yields energy densities far in excess of existing primary batteries. The power source had to meet the following specifications:

Voltage regulation from 20% to full rated load	28 ±2 V
Maximum load	50 A
Minimum load	10 A
Minimum discharge time (full load)	8 hr
Capacity	400 A-hr
Energy density	264 W-hr/kg (120 W-hr/lb) (minimum value)

To meet these goals, Leesona Moos Laboratory (LML) began development of a scale model 6 V, 70 A-hr battery containing cells with the exact electrode configuration and size that will be required for the 28 V, 400 A-hr vehicle power system

DESIGN DATA

The LML zinc-oxygen battery consists of a porous zinc anode, a lightweight, efficient, stable oxygen cathode, an alkaline (KOH) electrolyte, and a supply of oxygen (Fig. 1). The best design of a high-energy density zinc-oxygen battery has a maximum ratio of active or usable zinc weight to total battery weight. An efficient design to obtain the maximum zinc area per unit weight is a bicell construction. The bicell consists of two cathodes connected in parallel and supported by a suitable frame. The zinc anode is wrapped in separator material and inserted into the frame between the two cathodes. Intimate contact between the anode, separator, and cathode is achieved by proper cell support and stacking. Only an amount of electrolyte sufficient to saturate the anode structure and separator material is used. The electrolyte provides a continuous ionic path.

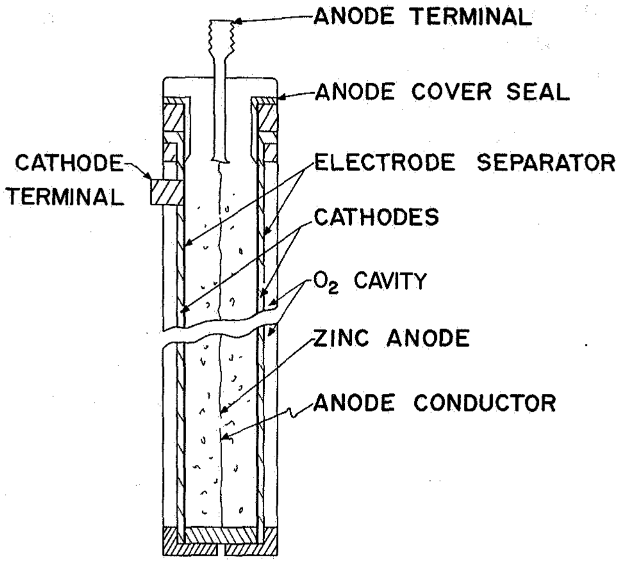

FIGURE 1. $Zn - O_2$ SINGLE CELL CROSS SECTION

The cathode establishes an active medium between the oxygen, catalyst, and electrolyte. The cathode consists of a semi-permeable film which permits oxygen to pass through to the catalyst side to be reduced, and yet retains the electrolyte within the cell. The oxygen cathode does not undergo any physical or chemical change in the course of producing power.

The electrochemical process occurring within the cell is shown below. The cell reactions are:

Anode: $Zn + 4OH^- \rightarrow ZnO_2^{=} + 2H_2O + 2e^-$

Cathode: $\frac{1}{2}O_2 + H_2O + 2e^- \rightarrow 2OH^-$

Cell: $Zn + \frac{1}{2}O_2 + 2OH^- \rightarrow ZnO_2^{=} + H_2O$

$Zn + \frac{1}{2}O_2 \rightarrow ZnO$

The zinc is oxidized at the anode, with electrons being released to the external circuit during the process. The electrons are received from the external circuit at the cathode and take part in the reduction of oxygen to hydroxyl ions at this electrode. The total cell reaction then results in oxidation of zinc. The anode reaction proceeds at a potential of + 1.216 V. The cathode potential is - 0.401 V. Overall cell potential is 1.617 V.

The ultimate energy density of a zinc-oxygen system is dependent upon the ratio of usable zinc to total battery weight and operating voltage according to the equation:

$$\text{Energy Density (W-hr/kg)} = \text{Operating Voltage (V)} \times \text{Zn utilization (\%)} \times 818 \text{ A-hr/kg} \times \text{Zn wt(kg)/Battery wt(kg)} \quad (1)$$

Zinc has an electrochemical equivalent of 818 A-hr/kg zinc (371 A-hr/lb zinc). In a cell operating at 1.25 V, it is theoretically possible to obtain 1020 W-hr/kg (464 W-hr/lb) based upon the weight of zinc alone. Faradic efficiency, cathode weight, electrolyte, and supporting structure limitations reduce this value. Figure 2 is a comparison of the energy density of the zinc-oxygen battery with that of a silver-zinc battery.

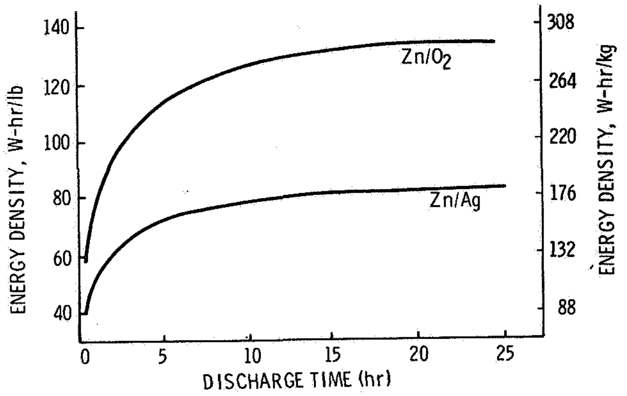

FIGURE 2. Zn - O_2 VS Zn - Ag

The variation of zinc utilization as a function of discharge current density at various anode thicknesses is shown in Figure 3. At low discharge rates, zinc utilization is practically independent of anode thickness. At higher current densities, efficiency

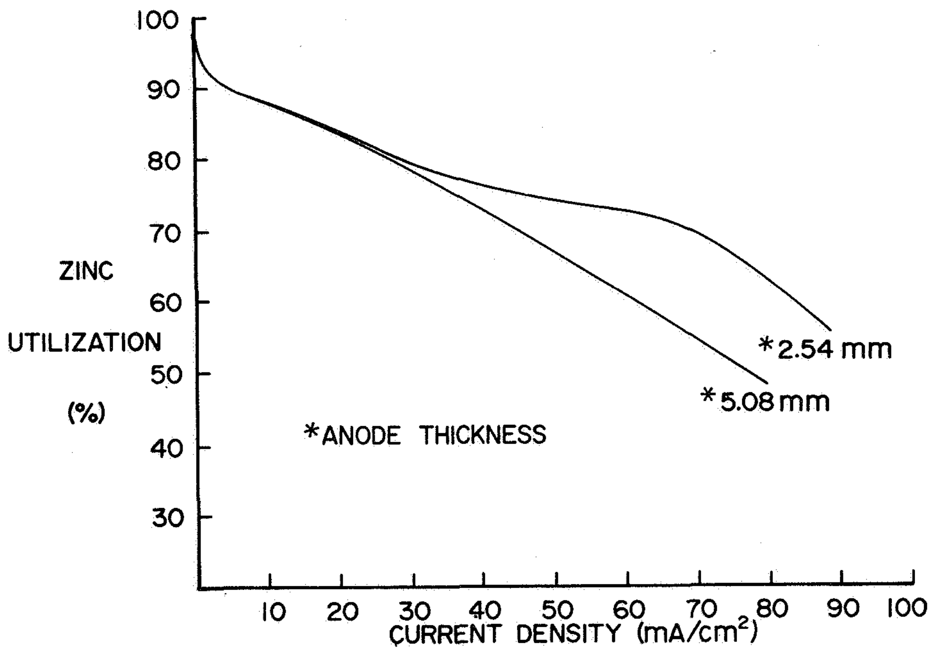

FIGURE 3. ZINC UTILIZATION

decreases with anode thickness. Therefore, low discharge rate batteries can use the thicker anode, and higher discharge rate batteries must incorporate the thinner anodes or the bicell construction.

A typical cathode polarization curve is shown in Figure 4. Current densities up to 350 mA/cm² can be supported using oxygen at atmospheric pressure. It can be concluded from the information shown in Figures 3 and 4 that the operating current of the battery is limited by the effect of zinc utilization efficiencies.

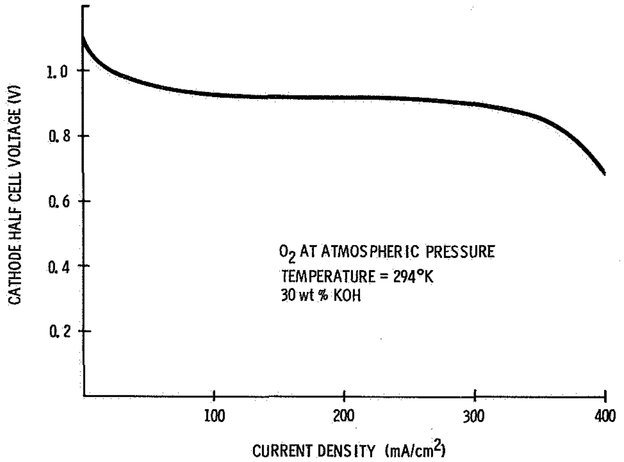

FIGURE 4. ELECTROCHEMICAL PERFORMANCE OF OXYGEN CATHODE

The current-voltage relationship of a fuel cell is flat over a broad region and permits good voltage regulation over a widely varying power profile. Figure 5 illustrates the voltage-time characteristics of a 6 V, 100 A-hr battery at the 8, 16, and 24 hr rates.

ANALYSIS AND DEVELOPMENT

Studies were made of various cell and anode configurations that yielded the maximum ratio of active component weight to frame weight, were easy to manufacture, and were simple to integrate into the battery system. On this basis a square, bicell configuration was selected. A parametric and failure analysis was performed to establish the optimum number of cells and stacking configuration required to yield the maximum energy density and overall system reliability. On the basis of this analysis, maximum energy densities occur when the cells are

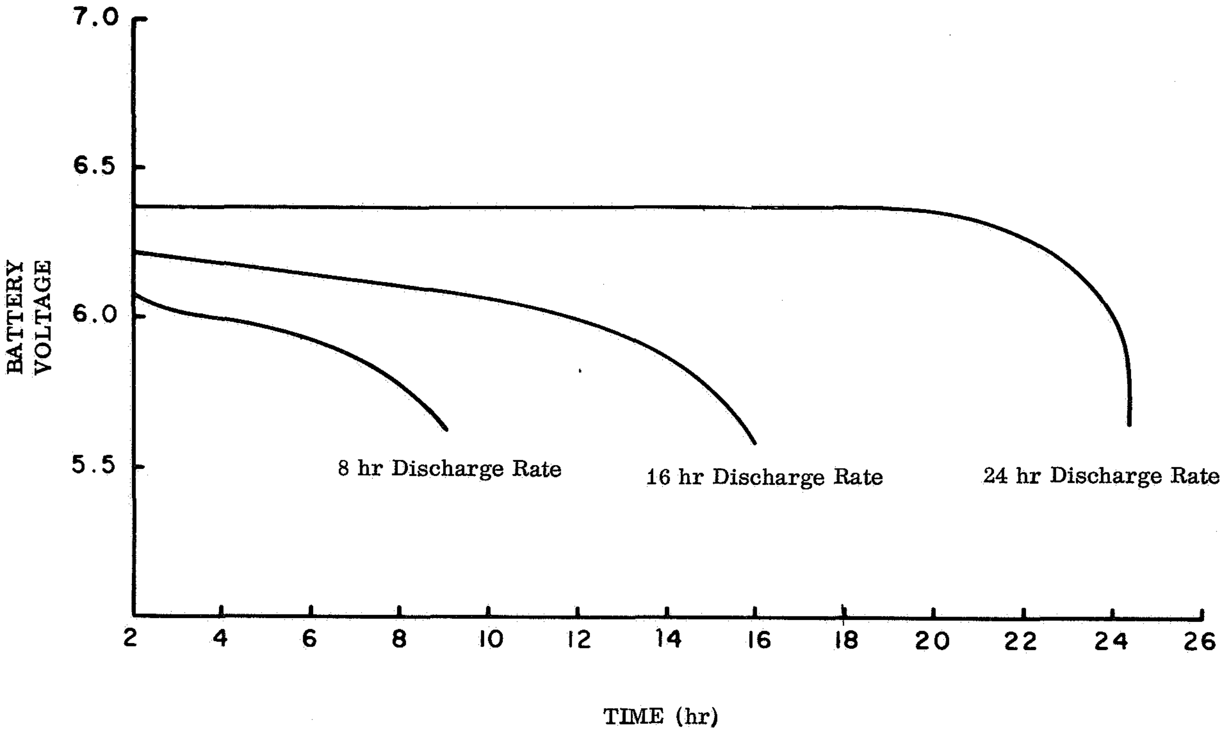

FIGURE 5. BATTERY VOLTAGE VS DISCHARGE TIME

designed to operate at current densities of 30 mA/ cm^2. Maximum reliability and minimum system weight are achieved using a stacking configuration of 23 series-connected modules with 6 parallel-connected cells per module. A total of 138 series/ parallel connected cells will be required for the final 28 V battery system.

An analysis was made to characterize the degree of heat dissipation. Using the heat of reaction of the zinc-to-zinc oxide process and Faraday's Laws of Electrolysis, the difference between the heat of reaction and useful electrical energy output was calculated as the heat to be rejected to stabilize internal battery temperatures. A new heat removal technique was designed in which the intercell separators are used as the means for heat removal. Figure 6 shows a schematic of the heat removal system. This concept uses corrugated magnesium intercell separators that are positioned between the cells, contacting the cathode surfaces and extending outward to achieve thermal contact with the battery case. The intercell separator actually performs four functions as follows:

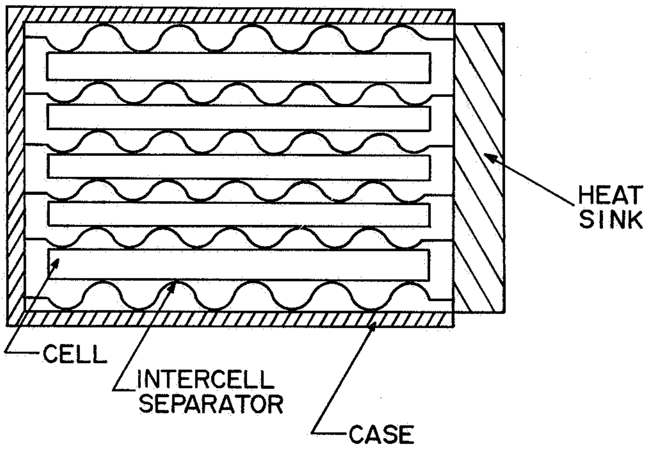

FIGURE 6. HEAT REJECTION SCHEMATIC

1. Allows oxygen to reach the cathode by providing a space between the cells.

2. Maintains intimate contact between the cathode, separator material, and anode.

3. Prevents growth of anodes during discharge.

4. Acts as the means for heat rejection.

Five series-connected cells, intercell separators, stack-support systems, and battery cases have been successfully integrated into a 6 V battery system. Evaluation of this system has demonstrated that its performance exceeds the minimum requirements projected for the 28 V system as shown below:

- Cell voltage regulation from 1.13 V to 1.3 V in excess of 8 hr at 30 mA/cm^2.
- Anode efficiencies in excess of 75%.
- Repeatability of results.
- Stabilization of internal battery temperatures at the 8 hr rate throughout the discharge period.
- Capability of withstanding a 5 to 2000 Hz, 6 to 10 g vibration and acceleration environment.

FUTURE EFFORTS

On the basis of the evaluation of the 6 V battery system, the outlook for successful fabrication of a reliable, constant 28 V, 400 A-hr battery system is excellent. A follow on program was initiated to accomplish this task. The work effort was divided into four phases as follows: (1) systems analysis and design studies, (2) engineering design, (3) fabrication and assembly of hardware, and (4) test and evaluation. The first phase is essentially complete and the second phase is in progress.

Figure 7 summarizes the projected 28 V battery and cell operating characteristics. The cell characteristics are based upon a projected stacking configuration of 6 parallel cells per module and 23 series modules. The first prototype battery to be developed under this program is scheduled for completion in May 1968. An extensive test program is planned to verify design and provide technical data for evaluation.

DISCHARGE TIME (Hr)	CURRENT (A)		CELL CURRENT DENSITY (mA/cm^2)	VOLTAGE			
				SYSTEM		CELL	
	SYSTEM	CELL		MAX.	MIN. (CUT-OFF)	MAX.	MIN. (CUT-OFF)
8	50(RATED)	8.33	30.5	30	26	1.3	1.13
16	25	4.17	15.25				
24	16.7	2.78	10.2				
40	10 (20%RATED)	1.67	6.1				

FIGURE 7. 28 V BATTERY SYSTEM OPERATING CHARACTERISTICS

FUEL CELL SYSTEMS

By

Walter H. Goodhue

SUMMARY

A significant effort has been made by MSFC to develop a capillary matrix closed-loop fuel cell system for space applications. Contracts with Allis-Chalmers Corporation have produced systems that can support a 3 kW continuous load for more than 1500 hr. A 5 kW load was sustained for periods of 1 min. Basic development work resulted in the fabrication of a design verification test (DVT) fuel cell system for qualification on space missions. This effort was performed in conjunction with Manned Spacecraft Center.

INTRODUCTION

Investigation of fuel cell technology and its application to space vehicles began in 1958 at Marshall Space Flight Center (MSFC). In 1964, Manned Spacecraft Center (MSC) became interested in the Allis-Chalmers fuel cell being developed by Marshall as a backup power supply for the Apollo Command Module and Lunar Module. Research Achievement Review Series No. 14, given in November 1965, outlined progress on fuel cell technology up to that time. This report covers the achievements to the present.

A fuel cell is an electrochemical power source that has definite application in space and lunar vehicles. Figure 1 shows the area where fuel cells can make a contribution in the space vehicle power spectrum.

Fuel cells of current technology offer great potential as power modules for 3 to 4 month missions and as energy storage devices for all power systems presently under consideration. Fuel cells are the only power source that produces water as a byproduct .

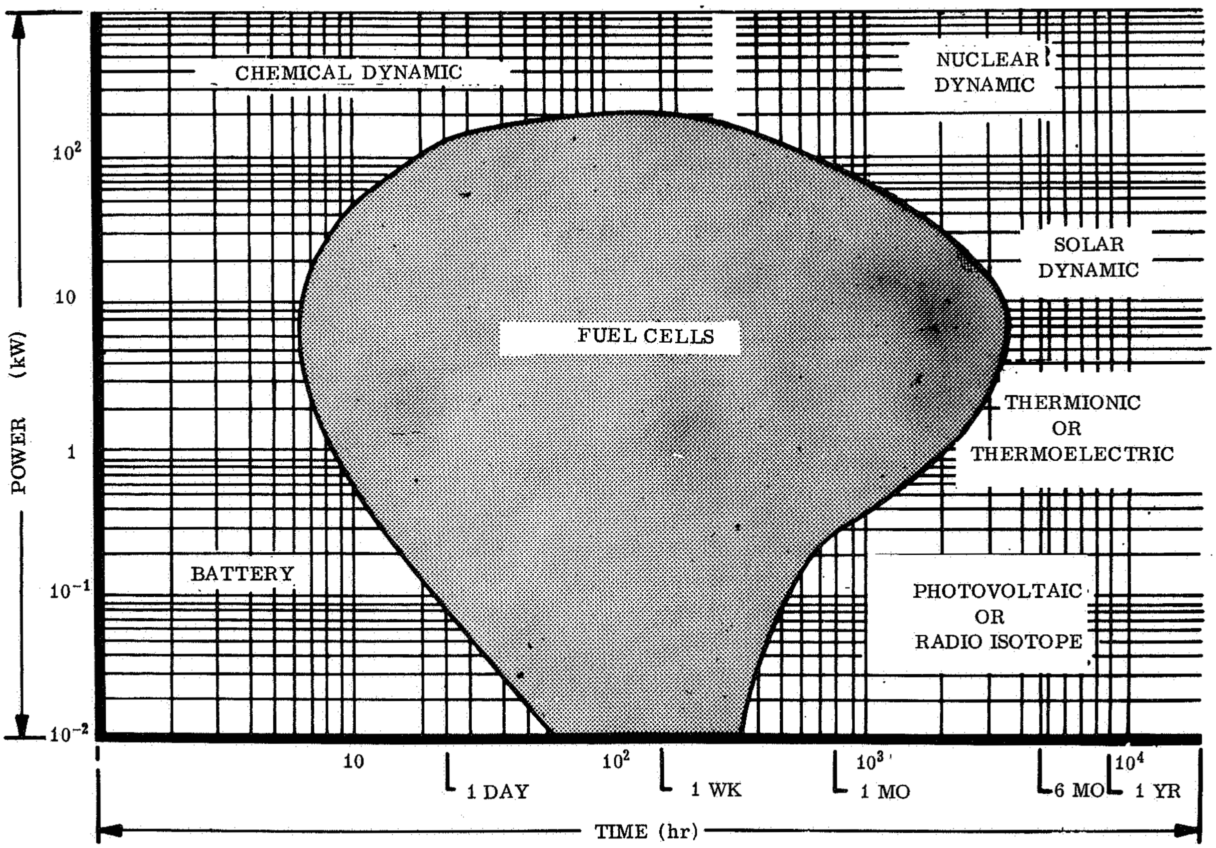

FIGURE 1. ANTICIPATED FUEL CELL RANGE

MSFC FUEL CELL

The fuel cell under development by MSFC is a capillary matrix (alkaline) cell. A fuel cell consumes gaseous hydrogen and oxygen to produce electricity, water, and heat (Fig. 2). The process requires a suitable electrolyte and catalyst. The ionization of hydrogen at the anode produces electrons, and the ionization of oxygen at the cathode consumes electrons. In the electrode reactions, water is produced at the anode and consumed at the cathode. Hydroxyl ions are produced at the cathode and consumed at the anode.

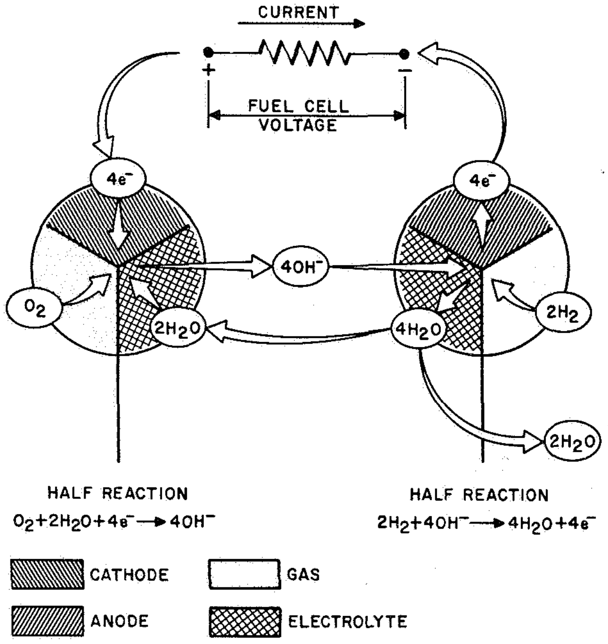

FIGURE 2. SIMPLIFIED FUEL CELL REACTIONS

Figure 3 is an artist's conception of basic fuel cell hardware. Reactants are fed through cavities in the oxygen and hydrogen manifold feed plates. The electrolyte is contained in an asbestos matrix which is sandwiched between the electrodes. Water, which is produced at the hydrogen electrode, is removed from a water removal plate through the water transport matrix. Power pick-off tabs are provided on the reactant plates. This is a completely static system, the only moving parts being the regulating valves. The system readily lends itself to zero gravity conditions because fluid transfer occurs only in the gaseous state, and there are no free liquids or components dependent upon gravity.

The basic fuel cell hardware is shown in Figure 4. The plates are gold plated magnesium with silver and platinum catalysts. Asbestos is used as membrane material. Synthetic gasket material is used to form a seal between plates and cavities.

Figure 5 shows a 2 kW fuel cell stack construction. Each cell has an effective reaction area of 186 cm^2. Stack cooling is accomplished by circulating helium gas through a duct, heat-exchanger subsystem contained within the metal enclosure, or canister.

Figure 6 shows the methods used to electrically interconnect individual cells. Cells are connected in parallel to form sections, and these sections are then connected in series to provide a nominal 29 V output.

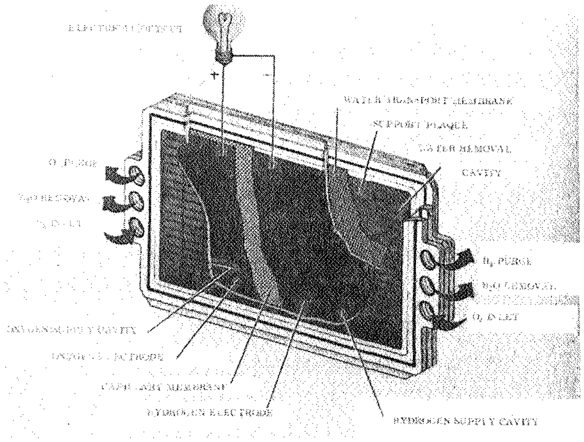

FIGURE 3. FUEL CELL SYSTEM

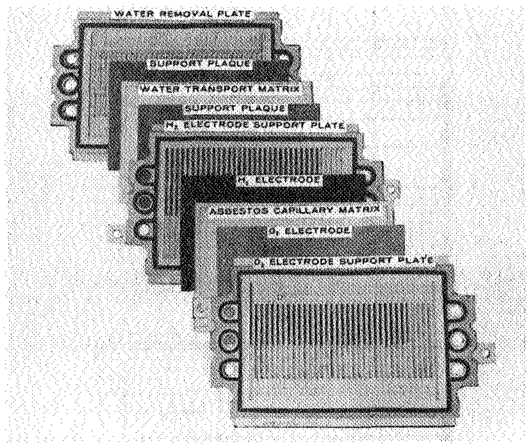

FIGURE 4. BASIC CELL HARDWARE

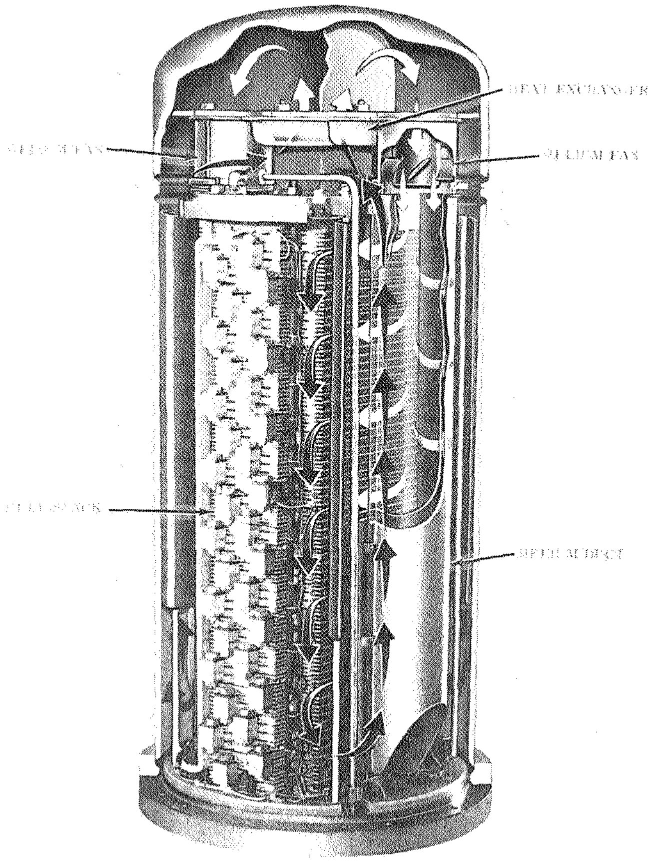

FIGURE 5. FUEL CELL COMPONENTS

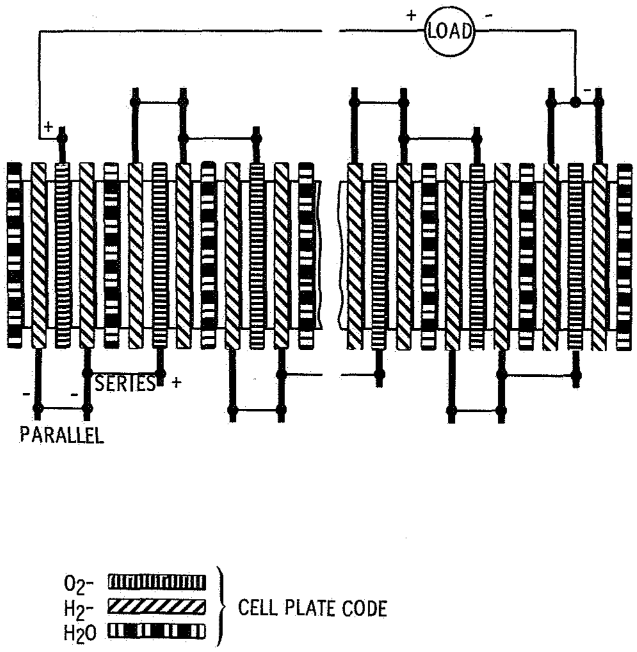

FIGURE 6. SIMPLIFIED SCHEMATIC OF CELL ELECTRICAL CONNECTIONS

FUEL CELL DEVELOPMENT

Allis-Chalmers Corporation of Milwaukee, Wisconsin, developed fuel cells under contract NAS8-2696, "Fuel Cell Systems." The original contract had three categories of effort: (1) research and technology tasks, (2) breadboard systems and laboratory support, and (3) engineering model systems. The goal of the program is to develop an efficient, reliable power source to replace batteries and other portable electrical power generating devices in the 2 kW, 28 V range.

The fuel cell module developed for NASA by Allis-Chalmers can be divided into five subsystems (Fig. 7). These subsystems and their functions are as follows:

1. Stack Subsystem
    - a. Electrochemically produces power
    - b. Produces water
    - c. Produces heat
2. Reactant Control and Conditioning Subsystem
    - a. Supplies reactant gas to stack
    - b. Purges impurities from stack
3. Thermal Control and Conditioning Subsystem
    - a. Provides start-up heating
    - b. Removes heat from stack, condenser, and inverter
4. Moisture Conditioning Subsystem
    - a. Removes product water from stack
    - b. Controls KOH concentration of stack
    - c. Condenses and transfers product water to storage
    - d. Provides open or closed loop operation
5. Electrical Monitoring and Control Assembly
    - a. Provides start temperature control
    - b. Provides reactant value control
    - c. Provides purge control
    - d. Provides moisture cavity control
    - e. Provides water recovery control

NOMINAL POWER RATING	2000 W
OVERLOAD	3300 W FOR 30 S
VOLTAGE REGULATION	29 ± 2 V LOAD RANGE, 800 TO 2000 W
MIN. VOLTAGE AT OVERLOAD	21 V
REACTANT INLET PRESSURE	68.9 to 276 N/cm^2 (100 to 400 psia)
REACTANT INLET TEMPERATURE	255°K to 339°K
REACTANT PURITY (EXPECTED)	99.9%
THERMAL EFFICIENCY	55-65%
ENDURANCE	720 hr UNDER LOAD
COOLANT	60% METHYL ALCOHOL, 40% WATER, BY WEIGHT
COOLANT SUPPLY	113.4 kg/hr (250 lb/hr) AT 15 ± 3°K
COOLANT PRESSURE DROP	3.4 N/cm^2 (5.0 psi)
START-UP AND SHUT-DOWN	1 hr FROM 255°K
ENVIRONMENT (DESIGN CRITERIA ONLY)	MOTION AND THERMAL VACUUM REQUIREMENTS

FIGURE 7. FUEL CELL MODULE SCHEMATIC

Figure 8 shows the initial requirements outlined for the fuel cell system at the beginning of the development. Modifications to the basic contract were made to perform research and development on materials and processes for establishing criteria to design an operational fuel cell power system for space

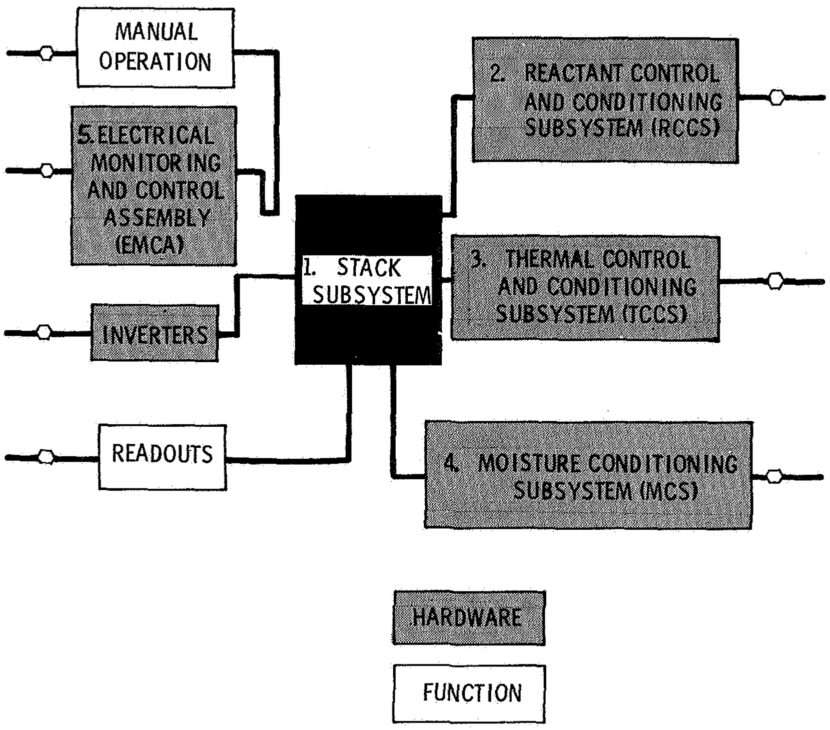

FIGURE 8. FUEL CELL POWER SYSTEM REQUIREMENTS

applications. This program was supplemented by thermal and heat flow studies. Significant progress was made toward development of a 2 kW system with a load life of 720 hr. Upgrading of a manually controlled system to full automatic operation was achieved. Eight test systems were fabricated; four of these were used for verification and endurance testing. Over 3300 hours of integrated system test history were compiled during these tests. Average power produced under the system load profile varied from 1.2 to 1.4 kW. The fuel cell systems have shown exceptional stability under steady state and transient load operation. Responses to load changes between 12 and 90 A were less than 100 ms.

A parallel development program was conducted to achieve the following objectives: (1) develop a closed loop (water recovery) fuel cell system packaged into a flight type configuration to include verification testing of subsystems and components, (2) optimize the system toward 1250 hr flight qualification and 1500 hr life demonstration, and (3) freeze the design and fabricate a flight prototype system and qualify this system for flight. This program produced the fuel cell shown in Figure 9. The DVT fuel cell system contained such design improvements as (1) an integrated reactant control and conditioning subsystem, (2) reactant preheater system, (3) updated moisture conditioning system, (4) water recovery system, and (5) refinements in the electrical monitoring and control system. The DVT fuel cell system also combined results from analyses of a water purification study and a heat exchanger development and study.

MSC increased their support of the Allis-Chalmers fuel cell development and a joint effort was initiated to develop systems that would qualify for AAP applications. Endurance testing of fuel systems to ultimate limits has shown the extreme ruggedness and versatility of the basic system and has defined component limitations. Anticipating their AAP requirements, MSC initiated a contract in October 1966 to develop flight prototype systems, using Contract 2696 model systems as the initial baseline. MSFC efforts were redirected toward providing research support and reliability testing of stacks. The system developed, the Design Verification Test (DVT), is shown in Figure 10. The DVT system may be mounted on any plane. The overall dimensions are 35.6 by 53.4 by 81.3 cm (14 by 21 by 32 in.). The module

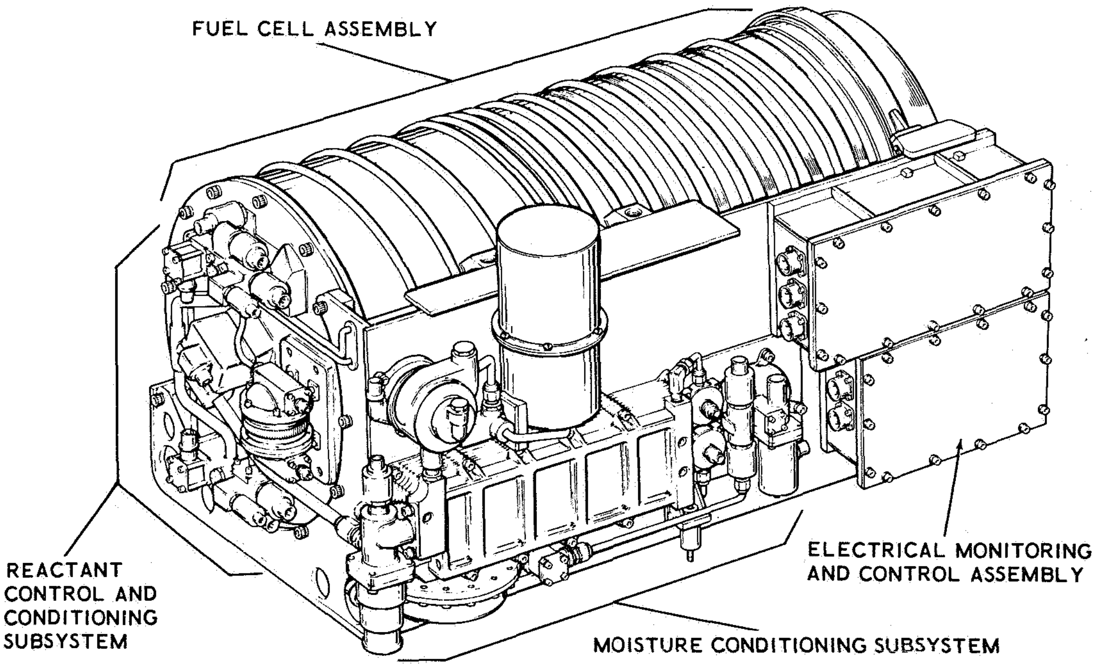

FIGURE 9. ALLIS-CHALMERS DVT FUEL CELL MODULE

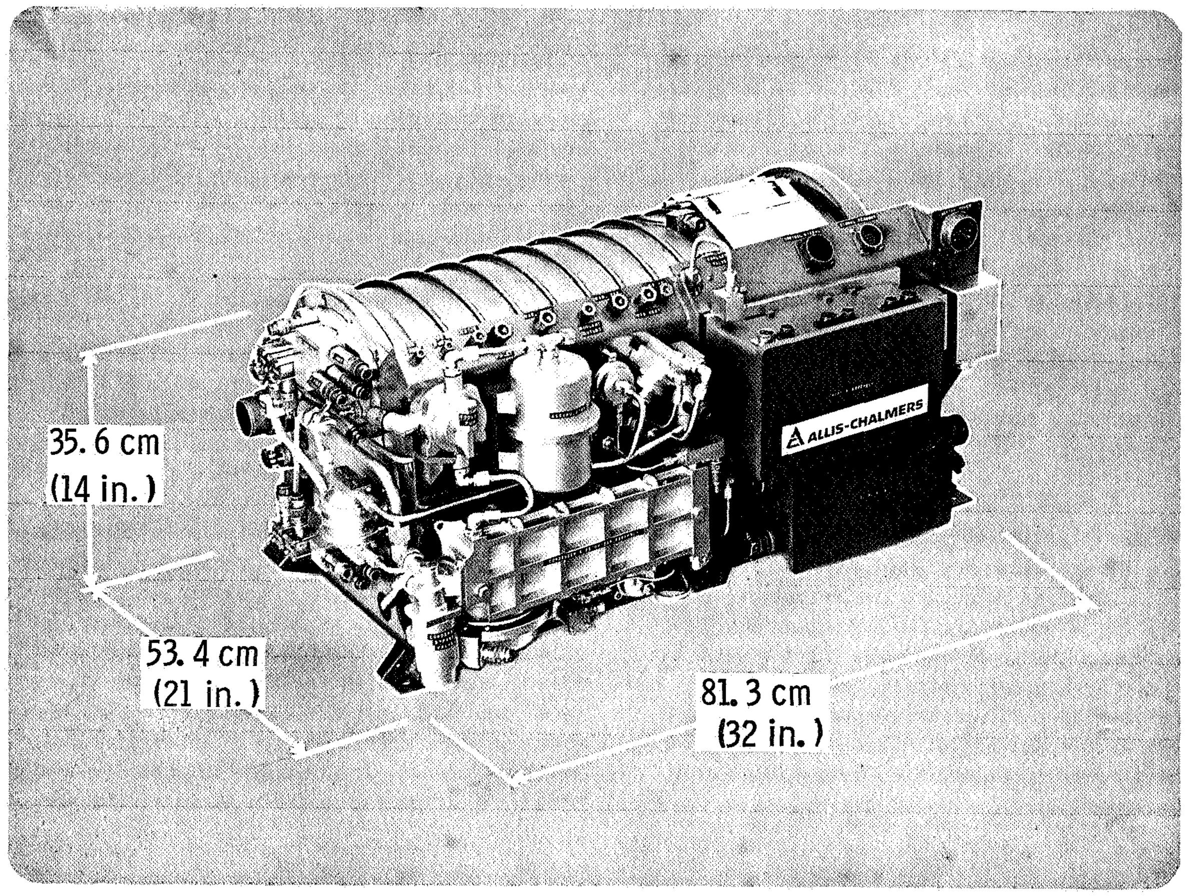

FIGURE 10. NASA 2 kW FUEL CELL MODULE

weight is 76.6 kg (169 lb). Figure 11 shows the voltage-power curves which the DVT unit is expected to meet. An engineering design system has passed 1500 hr testing and is exceeding the performance specified under the DVT contract.

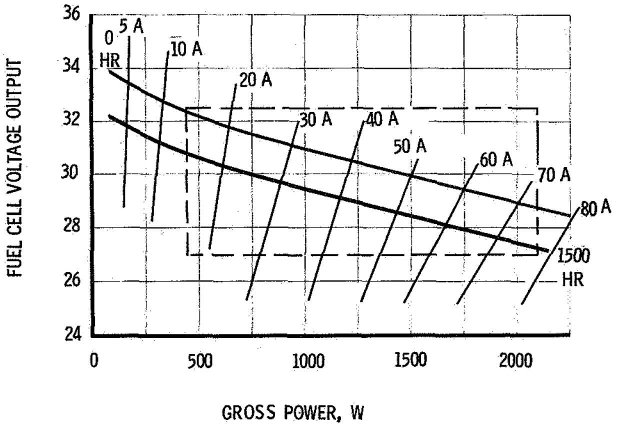

FIGURE 11. MODULE DVT ELECTRICAL PERFORMANCE

FUEL CELL TESTING PROGRAM

A stack testing program, "Fuel Cell Reliability Assessment," was directed toward determining fuel cell stack performance under high stress conditions and toward establishing reliable, operating limitations. The test units were to be eight complete fuel cell stacks of the existing centerline design. The goals were to establish the limits of operating temperature, reactant pressure and pressure differential, and water unbalance. In addition, the performance under continuous overload, high-spiked load, repetitive startup, hot standby, and continuous high power load were studied and evaluated. Figure 12 shows the tests which were to be run on the related fuel cell stacks. At present, testing of the first five stacks has been completed, while testing of the last three stacks is in progress. Total hours of test are as shown.

The construction parameters of the eight stacks were frozen prior to testing to assure uniformity of test data. However, a provision was made for including centerline design changes in the last three stacks.

FUEL CELL STACK NO.	TYPE OF TEST	TOTAL HR TESTED
131	LOAD FAILURE TEST	640.7
132	REACTANT PRESSURE TEST	774.8
133	LOW POWER LIFE TEST	1507.5
134	STARTUP TEST	1535.0
135	LOAD CYCLE TEST	575.1
136	LOW POWER LIFE TEST	ON TEST
137	THERMAL CYCLE TEST	
138	HIGH POWER LIFE TEST	

FIGURE 12. FUEL CELL RELIABILITY ASSESSMENT

Data obtained in operation of the first five stacks were analyzed, and centerline design changes were made in the last three stacks constructed.

Each of the stacks underwent acceptance testing for 40 hr and the optimum KOH concentration was determined during that period. Following the acceptance test, each stack was run at a continuous 40 A load for a 200 hr performance evaluation test. Operating conditions were made as identical as possible during the acceptance and performance evaluation tests. The reliability testing and off-limits testing followed the performance evaluation tests.

The first five stacks (131 through 135) were assembled with the electrolyte being applied individually to the matrices during stacking. This is called the wet stacking method.

The last three stacks (136 through 138) of this program have been loaded with electrolyte by means of a recently developed vacuum loading technique. These stacks have demonstrated a significant improvement in stability over the first five stacks which were filled with electrolyte using the wet stacking method.

The vacuum loading technique eliminates a problem of "crossleaks," which developed when the Cyanamid AB-40 electrodes tended to dry out in spots and perform erratically. The new vacuum loading technique supersaturates the electrode and overcomes an inherent water repellancy. After 750, 1500, and 800 hr of testing, the last three stacks were completely free of crossleaks. Also, a significant improvement in the voltage degradation rate for the vacuum loaded stacks over the wet stacked cells was evident.

Stack 131, which was the Load Failure Test, was operated for a total of 640.7 hr. The stack produced currents in excess of 400 A and 5 kW. Because of heat removal limitations, periods of high power output were limited to 15 s to prevent over-heating the stack. The cooling system was capable of thermal control at a steady state current of 120 A. Figure 13 shows a summary of the high power capability of the stack. Final failure was caused by water transport matrix leakage, resulting from a lack of control in water removal.

TEST RESULTS

LOAD LEVEL Amperes	LOAD LEVEL kW	DURATION min		NO. OF OCCURRENCES
100 - 200	2.5 - 4.5	5.0		21
201 - 250	4.5 - 4.8	2.0		7
251 - 350	4.8 - 5.0	1.0		20
351 - 450	5.0 - 3.0	0.25		10
			TOTAL	58

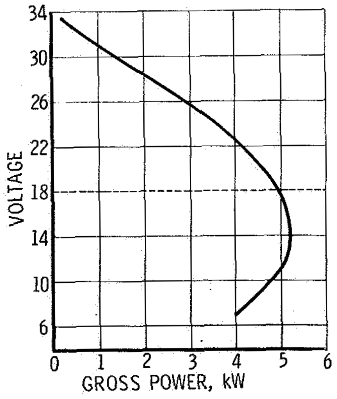

FIGURE 13. MODULE OVERLOAD PERFORMANCE

Stack 132, the Reactant Pressure Test, was operated for a total of 774 hr. Failure resulted indirectly from operation at a pressure of 36.5 N/cm^2 (53 psi). The canister was maintained at a helium pressure several kilograms above the reactants. This caused six of the gaskets to be forced into manifold bores, which resulted in canister to stack leakage.

Stack 133, the Low Power Life Test, was operated at a steady load of 40 A for 1500 hr. Difficulty with purging and cross leakage strongly indicated the need for an increased amount of electrolyte and stabilization of the AB-40 anodes.

Stack 134, used in start-up experiments, was subjected to more than 50 start-stop cycles.

Start-up of the fuel cell stack requires heating the stack to approximately 356° K (180° F). This is done by heaters placed on the stack and obtaining power from an outside source or by "bootstrap" starts (self heating of the stack). Bootstrap starts from 299 to 356° K (78 to 180° F) operating temperature were accomplished in times as short as seven minutes. Figure 14 illustrates the warmup characteristics of the module when terminal voltage was maintained at 27.5 V and shows heatup curves for constant current curves of 100 and 250 A respectively.

TEST RESULTS

ELECTRICAL OUTPUT LIMIT	WARM UP TIME, min
27.5 V	59
100 A	26.5
250 A	6.5

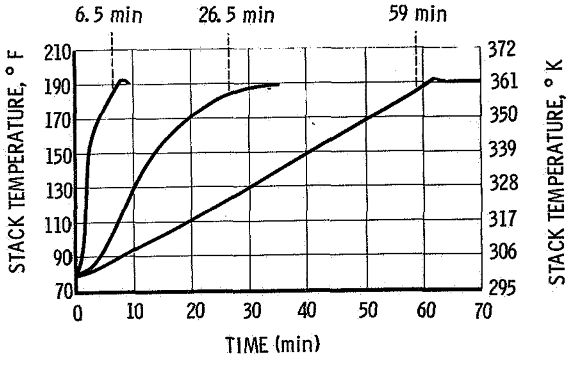

FIGURE 14. BOOTSTRAP CAPABILITY

RESULTS

Stack 135, the Load Cycle Test, was tested under a cyclic load condition for 575 hr. Development of cross leakage resulted in a decision to terminate the testing of the stack. The behavior of this stack was further evidence of the deficiency of electrolyte in the Wet Stacked Group. Figure 15 shows the number of fuel cell stacks tested and gives an indication of hours tested.

From the tests described earlier the following capabilities of the fuel cell system have been demonstrated:

1. Capability of sustaining a continuous load in excess of 3 kW.
2. Brief (1 min) power output capabilities above 5 kW.
3. Brief (15 s) current output capabilities in excess of 400 A.

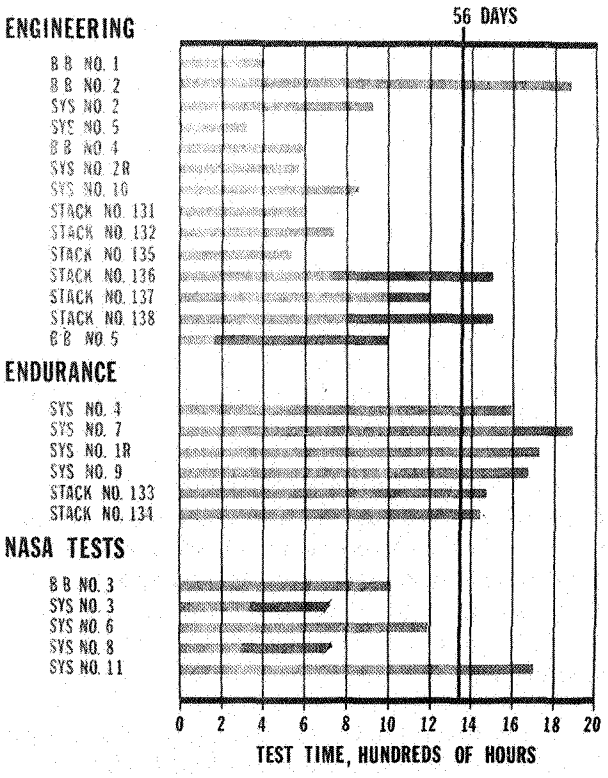

FIGURE 15. NASA HISTORY OF FUEL CELL TESTING

4. Capability of over 1000 hr of continuous on-line power production at a 1200 W level.
5. Capability of over 40 start-up cycles without detrimental effect upon performance.
6. Bootstrap start-up capability from room temperature to operating temperature in less than 7 min.
7. Useful lifetime in excess of 1500 hr.

FUTURE PLANS

Future fuel cell development effort is outlined below and pertains to the general program. This R&D effort extends beyond technology readiness and will demonstrate flightworthiness. It has objectives as follows:

1. Development and Test
   a. Develop a closed cycle 2kW H_2-O_2 fuel cell system for space missions to 90 days.
   b. Complete development of 1500 hr fuel cell system for DVT testing by NASA and Allis-Chalmers. Continue design effort towards a 2500 hr system.
2. Technology
   a. Perform analysis and conduct tests to develop technology for long life, high performance, and reliable fuel cell systems for space applications.
   b. Perform studies and conduct tests on electrodes, matrices, electrolytes, scale-up effects, purging, cooling techniques and operating variables.
3. Reliability Assessment
   a. Evaluation of 2 kW fuel cell performance capability under both normal and overstress conditions, to establish operating limitations for reliable operation.
   b. Perform endurance and off-limits tests to assess reliability.

FUEL CELL TECHNOLOGY

by

John R. Morgan

SUMMARY

The development of fuel cell technology at Marshall Space Flight Center is described. Research was conducted in electrodes and electrolytes at the basic research level and in cooling systems and environmental testing at the systems' analysis level.

INTRODUCTION

NASA research contracts have resulted in a progressive series of fuel cell system research and development efforts. Information obtained from experimental tests performed during 1966 was applied to systems fabricated under the system development contract, NAS 8-2696.

Research contracts are investigating cooling systems that permit a higher radiator temperature, circulating electrolyte, and reduction in size of the radiator, electrodes, catalysts, and electrolytes.

THERMAL ANALYSIS STUDIES

The primary goal of the thermal analysis studies was to develop improved techniques for thermal control of fuel cell systems. The four approaches considered were cold plate cooling, heat pipe cooling, cooling with gases other than helium, and liquid cooling with direct fin contact. The first concept (cold plate cooling) was selected as the approach to be considered for a breadboard fuel cell (Fig. 1).

A cold plate was designed and fabricated for application to a fuel cell stack. After system operation under load in excess of 100 hr, indications are that the cold plate design decreases the temperature differential between the stack and the coolant by a factor of two, thereby increasing the radiator temperature and resulting in a more efficient radiator. A problem area was the selection of an electrically insulating heat transfer material between the fuel cell plate edges and the cold plate. The material finally selected was a silastic adhesive with magnesium oxide added for increased thermal conductivity.

An alternate cold plate configuration, chosen for a second thermal breadboard concept, was to place cold plates between individual cells (Fig. 2). For engineering evaluation, the stack was designed with 9 cells rather than the 32 cells of a full system. The cold plate is fabricated from two separate plates that are stacked to form a sealed cavity containing a separate coolant matrix. The thermal control schematic is given in Figure 3. The coolant is supplied under pressure to one side of the coolant matrix. The coolant is removed in a vapor from the other side of the matrix. The coolant flow rate is controlled by the pressure differential between the inlet and outlet manifolds.

ELECTRODE EVALUATION

To date, 32 single sections have been tested for a total of more than 40,000 hr to evaluate electrodes and catalysts. Twenty-six sections were operated to evaluate the cyanamid AB-40 anode. Six tests were conducted to evaluate a silver-platinum anode. The factors evaluated included construction parameters, operating conditions effects, and electrode conditioning.

Twelve single sections were tested to evaluate variations in assembly procedures. These tests indicated that the AB-40 anode approach was sound and represented a technological improvement over previously used anodes. The construction parameters of a configuration considered acceptable for centerline technology are given in Table I.

Using this centerline technology, 14 modules were fabricated to evaluate operating conditions effects. These tests indicated that voltage degradation rates were higher at higher temperatures and were much lower when the modules were operated at a high current density during the first segment of the test.

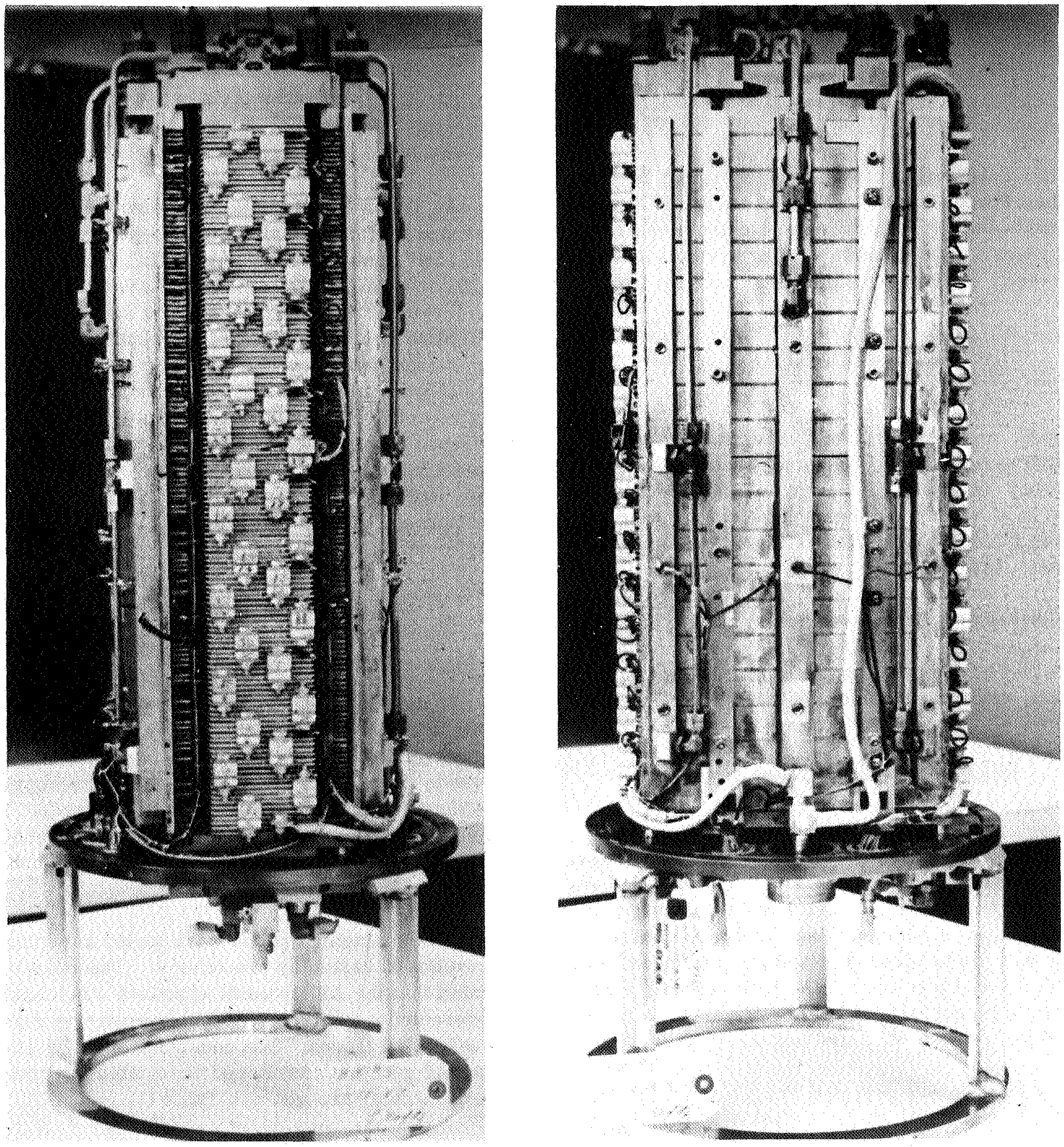

FIGURE 1. COLD PLATE BREADBOARD FUEL CELL SYSTEM

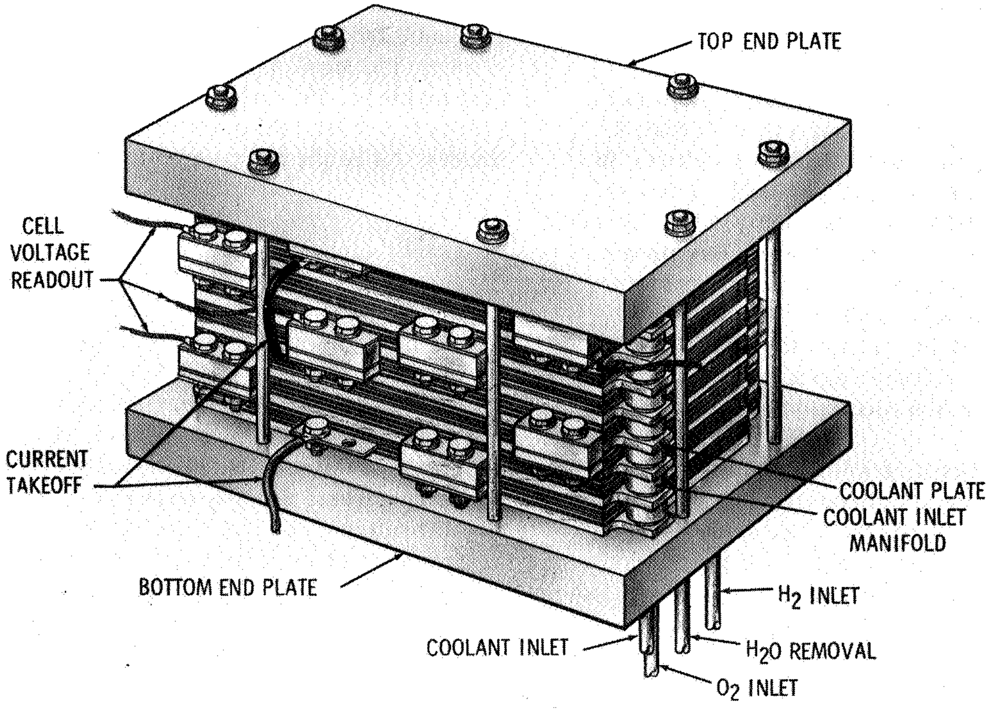

FIGURE 2. ADVANCED COLD PLATE BREADBOARD

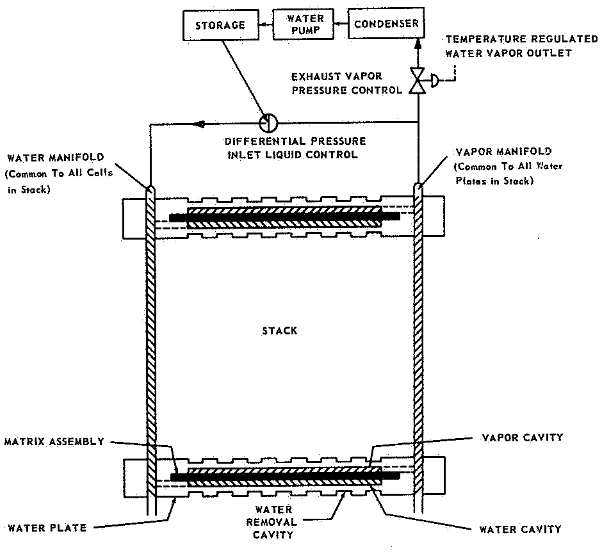

FIGURE 3. INTERNAL COLD PLATE CONTROL

TABLE I. CENTERLINE TECHNOLOGY CONSTRUCTION PARAMETERS

ANODE	CYANAMID AB-40
ELECTRODE	HYSAC - 8
WATER CAVITY MATRIX THICKNESS	1.27 mm (0.050 in.)
REACTANT CAVITY MATRIX THICKNESS	0.75 mm (0.030 in.)
SPACER THICKNESS	1.65 mm (0.065 in.)

An analysis of the operating data for the cells that failed indicated that insufficient electrolyte at the electrodes could have been the direct cause of, or a contributing factor to, failure. As a result, modified methods of loading the electrolyte into the matrix were investigated. The AB-40 anode exhibits limited wettability to the electrolyte and tends to retain trapped gases in the electrode pores, when previous procedures are used. Modules were constructed with this wetting or preconditioning of the electrode being accomplished by vacuum loading the electrode and by flushing a completed module with electrolyte after fabrication. Both methods appear to yield equally favorable results.

Voltage life characteristics of two typical cells with preconditioned anodes are shown in Figure 4. For a 32 cell stack, the system's lower voltage limit of 27 V is equivalent to 845 mV per cell. After an average load time at 1500 hr, the non-preconditioned anode cells degraded below this level. For preconditioned cells, this average load time has been increased to approximately 2500 hr. Compared with non-preconditioned cells, cells with conditioned anodes exhibit lower voltage degradation rates and a more consistent optimum electrolyte concentration.

The wetting difficulties associated with the AB-40 anode make the mechanical properties of the silver-platinum anode more desirable. Six modules were constructed to evaluate performance of these anodes. The catalyst loading varied densities of platinum and a combination of platinum and palladium. All modules were operated under the same conditions. Testing of the silver-platinum anode indicated that the voltage-life characteristics of these cells were inferior to cells fabricated with the AB-40 anodes. Figure 5 is a comparison of voltage envelopes of the silver-platinum anodes with the AB-40 anodes in similarly constructed small modules. With comparable catalyst loadings, the initial cell voltages for the silver-platinum anodes are lower than that of the AB-40 anodes, as is the average voltage degradation rate.

ELECTROLYTE EVALUATION

One degradation mechanism of a fuel cell is the formation of potassium carbonate, K_2CO_3, caused by exposure of the electrolyte to carbon dioxide in the reactant gases. Studies were initiated to investigate the alteration of the vapor pressure-temperature relationship of the electrolyte caused by the presence of K_2CO_3. The studies indicated that the reaction of carbon dioxide with the electrolyte tends to increase the vapor pressure required for constant potassium concentration; however, the effect is not sufficient to induce errors with the existing control methods.

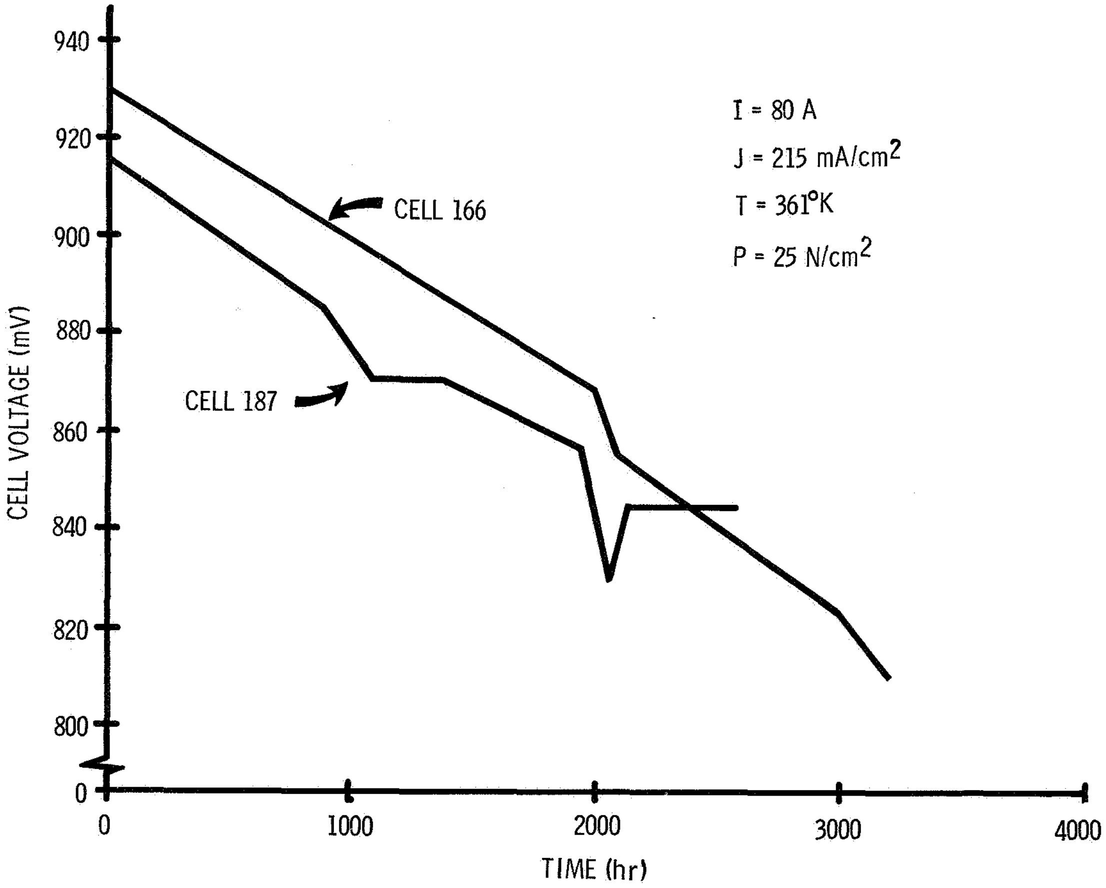

FIGURE 4. TYPICAL PRECONDITIONED ANODE CELL LIFE CHARACTERISTICS

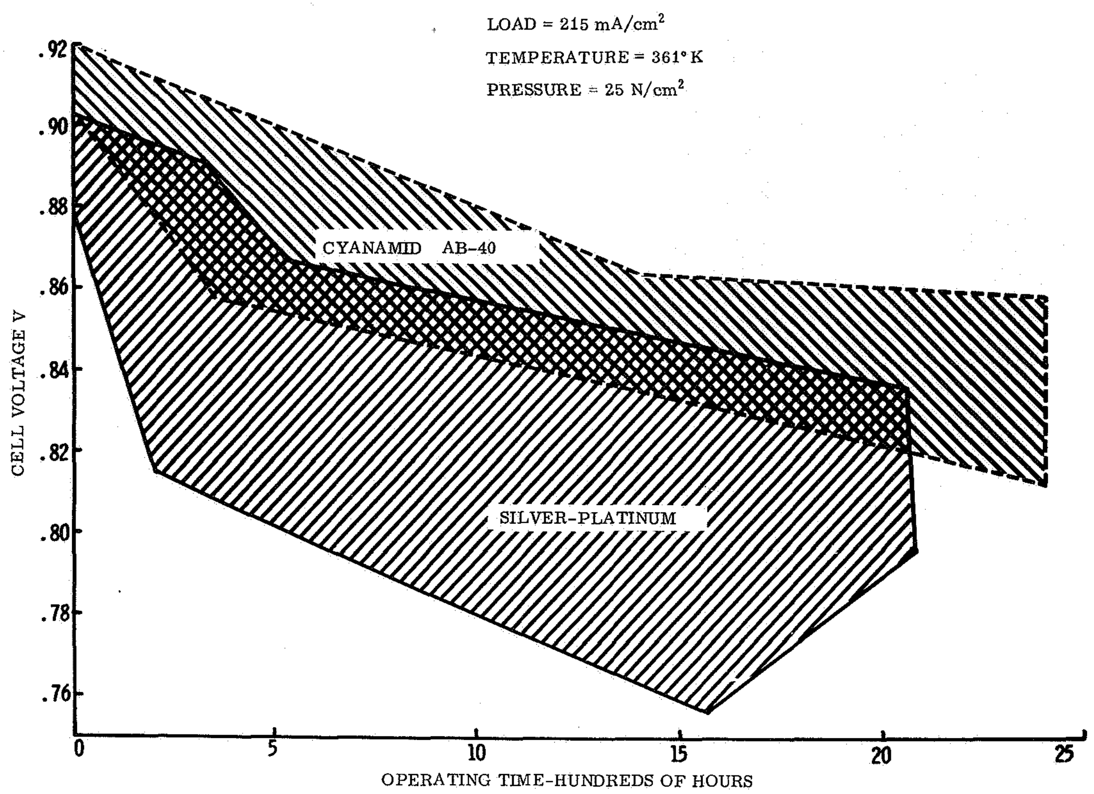

FIGURE 5. CYANAMID AB-40 VS SILVER-PLATINUM ANODE

A test of cesium hydroxide as a fuel cell electrolyte was conducted using two single sections. One section was operated for 2000 hr, the other for 550 hr. As a result of these tests, the following comparisons with potassium hydroxide electrolyte cells have been made: voltage degradation is lower for cells with cesium hydroxide electrolyte, initial voltage at loading is lower, and operating cavity pressure is higher.

INHOUSE TESTING

Inhouse achievements are as follows: completion of a series of environmental tests using Allis-Chalmers system number eight, completion of an electrical monitoring and control system design, initiation of a single cell testing program, and completion of design and construction of a parallel system test console.

The first portion of the environmental test sequence was a thermal-vacuum test. Fuel cell system number eight was mounted in the thermal vacuum chamber with auxiliary test equipment installed nearby (Fig. 6). The fuel cell was operated at a minimum sustaining power level with the chamber wall temperatures down to 188°K, and at a 2 kW power level with the chamber wall temperature up to 358°K.

The fuel cell, installed on a 7.32 m (24 ft) centrifuge for the acceleration testing, is shown in Figure 7. The reactant bottles were packaged on the opposite end of the arm, with fluid and gaseous control equipment placed near the center of the centrifuge. The fuel cell was subjected to three, six, and twelve g's acceleration. At each level, the reactant cavities of the system were filled with an inert gas to detect possible leakage. After verification that leaks did not exist, the system was operated at a load of 40A and 80A while under acceleration. This sequence of acceleration testing was performed with the direction of acceleration in each of the three axes of the fuel cell stack.

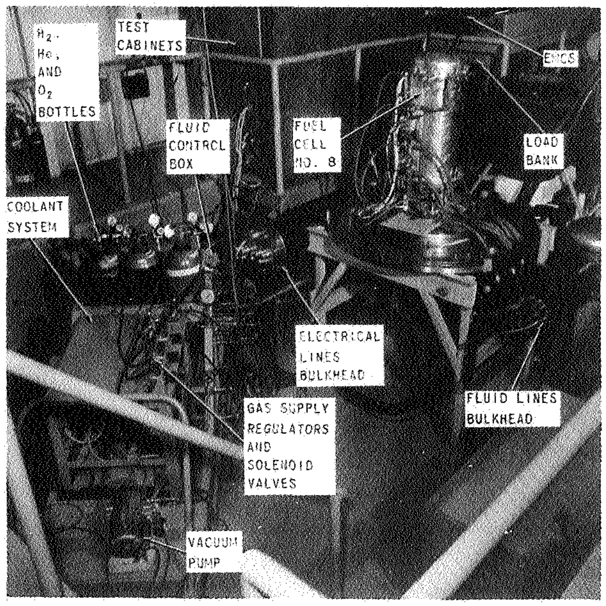

FIGURE 6. THERMAL-VACUUM TEST AREA

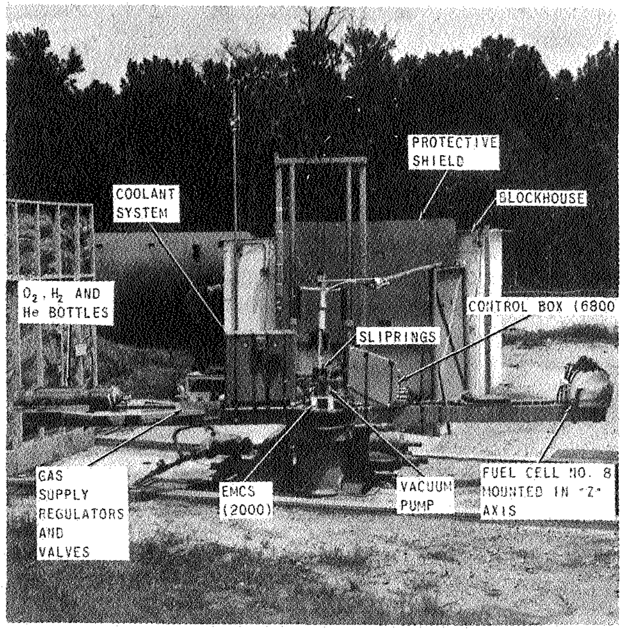

FIGURE 7. CENTRIFUGE TEST AREA

Following the acceleration test, the fuel cell system was mounted on a vibration slip table. The auxiliary control equipment remained on the centrifuge arm. The test set-up is shown in Figure 8. The reactant interface was accomplished by use of flexible hosing. The system was subjected to vibration levels of three and six g's in each axis of the fuel cell stack with the system filled with inert gases and with the system under load.

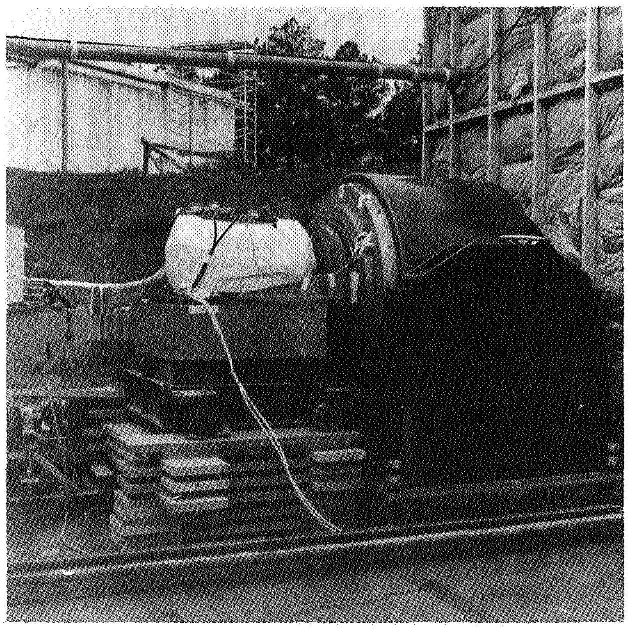

FIGURE 8. VIBRATION TEST AREA

The sequence of environmental tests yielded valuable information concerning instrumentation and control of fuel systems under adverse conditions. The major problem area encountered was auxiliary equipment failure. Several instrumentation wires were broken as illustrated in Figures 9 and 10. These failures did not impair the system operation; secondary instrumentation revealed that the event was an instrumentation failure rather than fuel cell stack failure.

During the vibration sequence, the hydrogen and oxygen pressure transducers and the coolant solenoid on the reactant control and conditioning subsystem (RCCS) plate experienced excessive vibration loads. To reduce these loads, the RCCS plate was modified as shown in Figure 11.

Using the information gained, a new series of acceleration and vibration tests have been initiated to gain more data on fuel cell operation under these conditions. More reliable instrumentation is incorporated in the new set-up. The removal of the RCCS from the canister to prevent component failure during environmental tests is illustrated in Figure 12. Again, the gas bottles are mounted on the centrifuge arm opposite the fuel cell assembly, with all the control equipment located near the center.

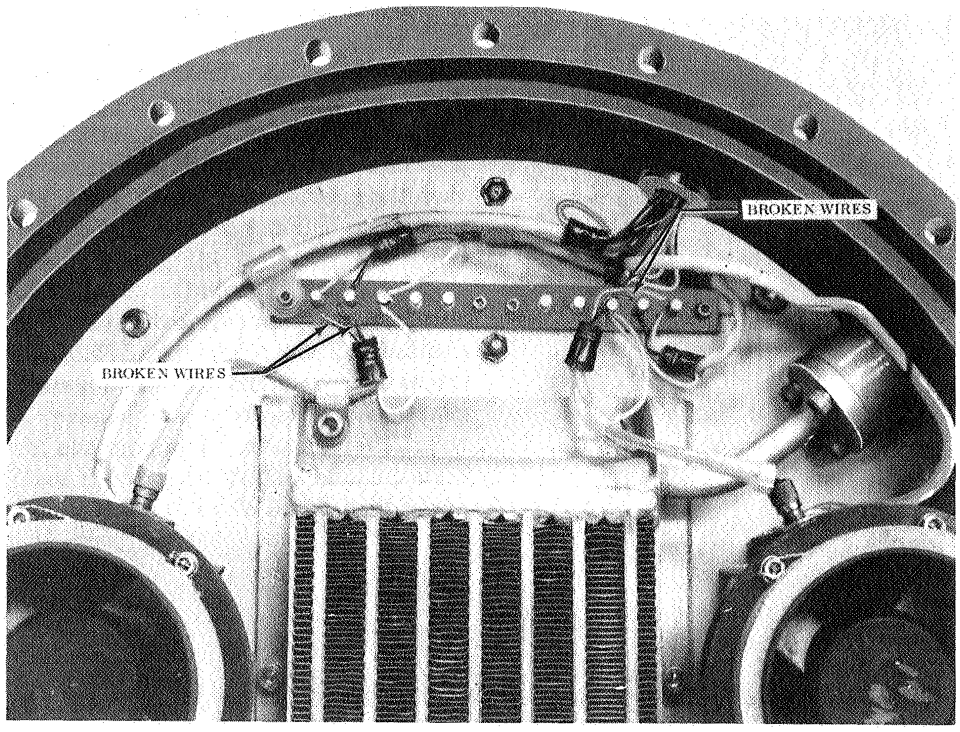

FIGURE 9. FAN RPM READOUT FAILURE

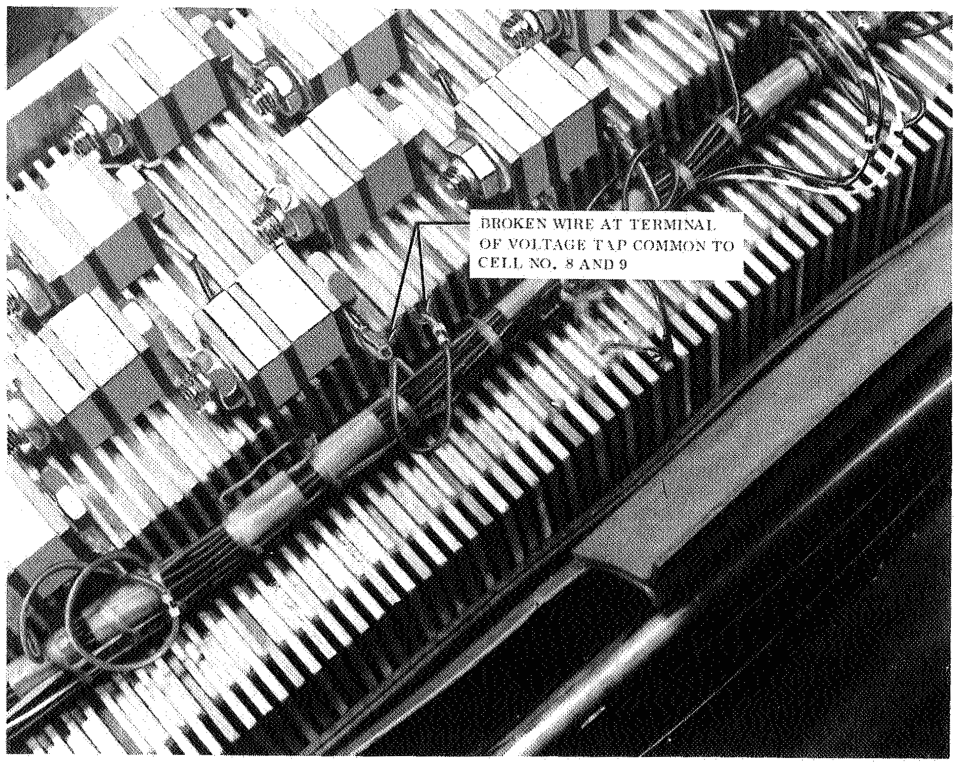

FIGURE 10. CELL VOLTAGE READOUT FAILURE

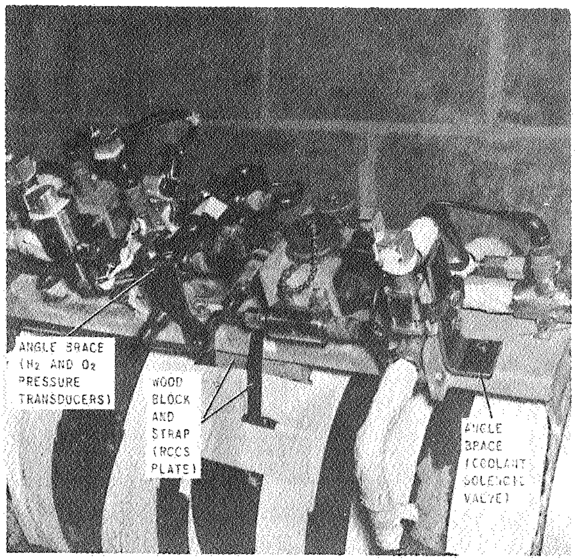

FIGURE 11. RCCS PLATE AND COMPONENTS MODIFICATION

During the environmental test, the electrical control system proved to be highly sensitive to noise, temperature, and humidity. To eliminate these problems, a new flight-oriented control system was designed and evaluated. Preliminary indications are that this control system will prove to be more rugged than the previous package. Presently, the control system is being constructed in a flight-type package.

A control console for parallel operation of two systems has been fabricated (Fig. 13). This console contains all the reactant and fluid controls, the electrical controls, and the data acquisition system. Strip chart recorders and a data scanner comprise the data acquisition system. Future plans for the parallel tests include load sharing and transient response analysis of parallel operated fuel cells.

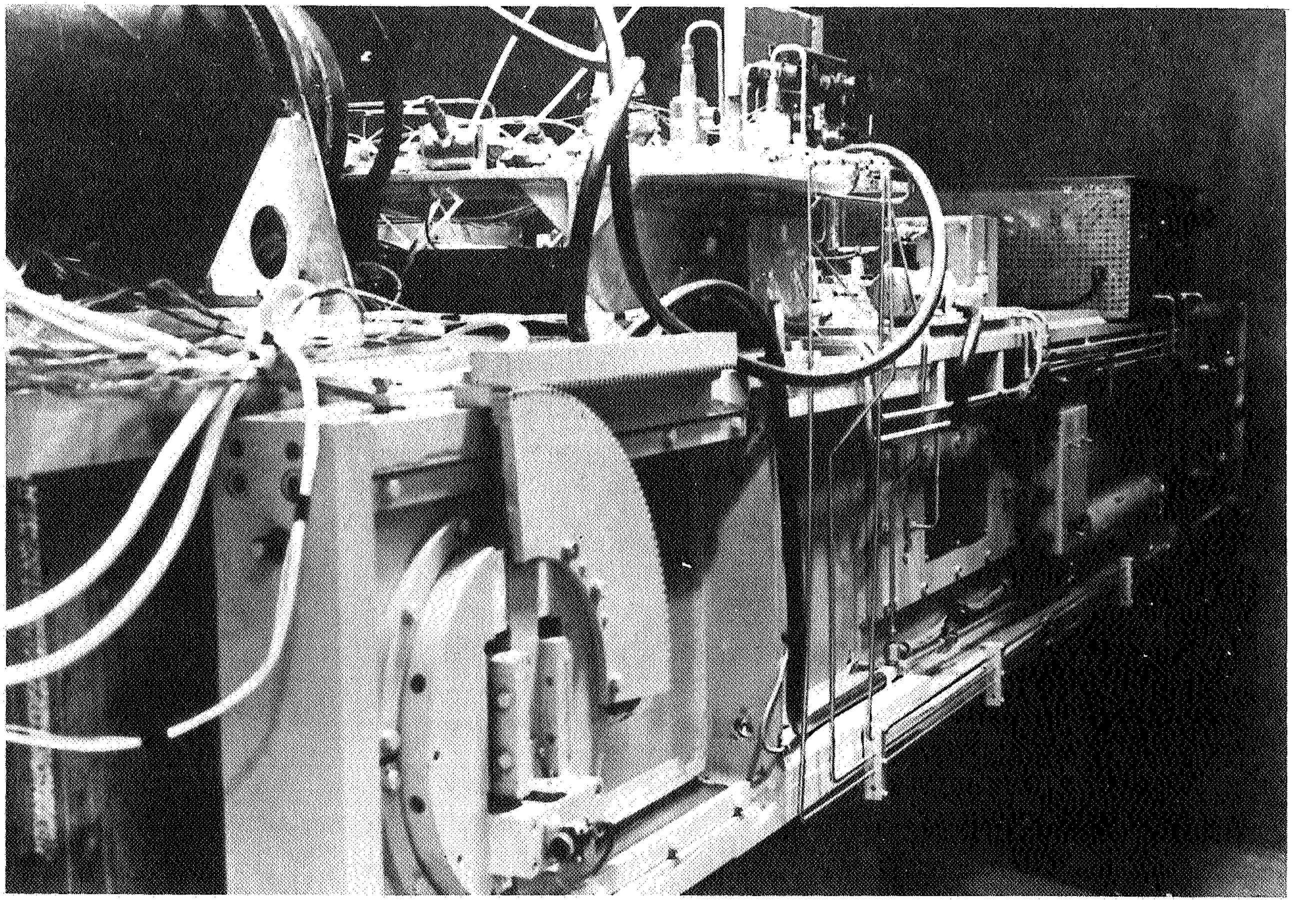

FIGURE 12. IMPROVED CENTRIFUGE TEST AREA

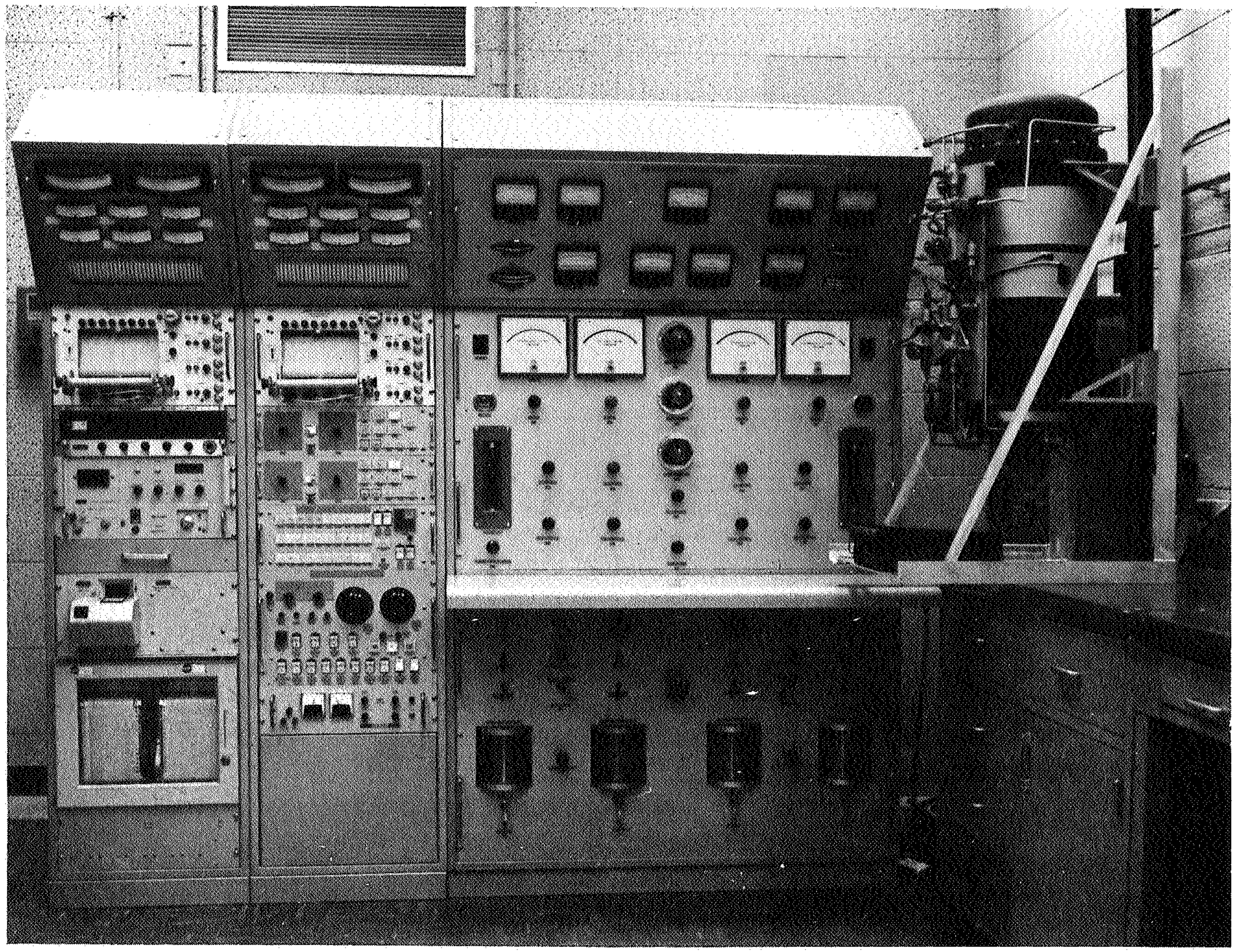

FIGURE 13. PARALLEL TEST CONSOLE

ADVANCED SYSTEM CONCEPT

The single cell optimization study combines several design concepts from different manufacturers. A concept that is basically a modified Allis-Chalmers system is illustrated by Figure 14. This system is compact, self-contained, and requires only coolant and power connections. Presently, this system is in a definition and design phase and has not been implemented into a hardware phase.

The cell is composed of three subassemblies that are stacked in sequence (Fig. 15). The sequence is then reversed and the process is repeated until a unit of the desired rating is constructed. Water removal plate, matrix plate, and coolant plate are the three subassemblies. The control and component subassembly is located at the top of the stack for convenient access. The reactant tanks are mounted around the circumference of the module where rejected heat might be used to supply cryogenic boiloff for reactant pressure. The cell base is provided with access ports, which make a partial interior inspection possible without disassembling the system. All spacer plates are machined with hydrogen, oxygen, water removal, and coolant manifolds to provide a continuous fluid path through the cell.

The matrix spacer, shown in Figure 16, will be fabricated from a filled teflon material to provide insulation and maintain chemical inertness. The electrodes are edge bonded to the matrix. The matrix electrode package is bonded into the spacer. The size of the manifolds and the number of the gas supply ports are intended to prevent any possible plugging of the stack and eliminate a possible variation in gas flow. The hydrogen porting arrangement

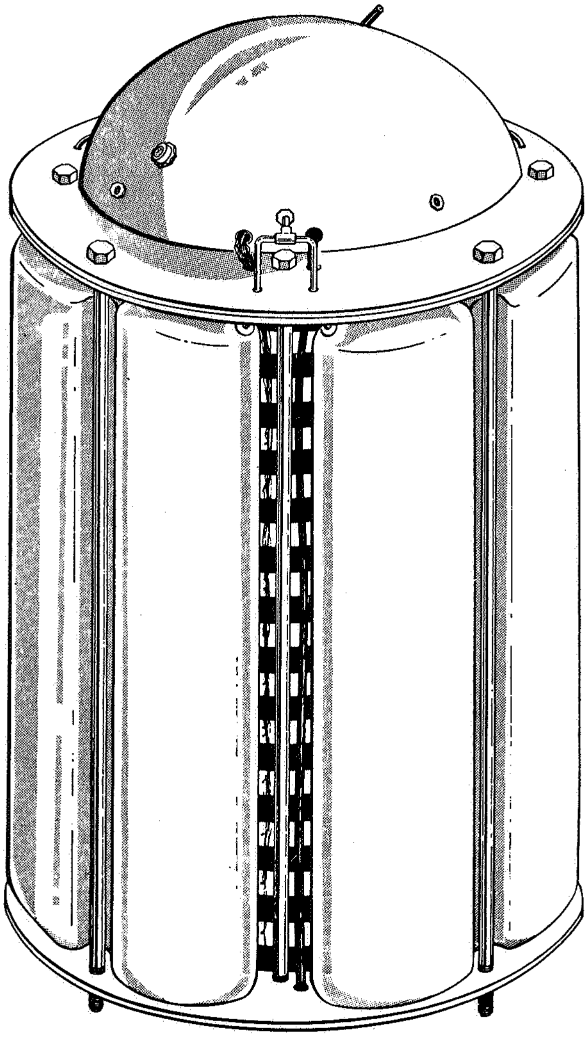

FIGURE 14. ADVANCED SYSTEM CONCEPT

is shown in Figure 16. The oxygen porting is on the underside of the plate edges, perpendicular to the hydrogen porting and identical to it in construction.

The system is intended to employ the static water removal mechanism developed by Allis-Chalmers. In this system a vapor pressure is maintained in the plate cavity, which corresponds to the equilibrium vapor pressure for the electrolyte concentration in the cell. By-product water is removed in this manner, thereby maintaining the desired electrolyte concentration. The water removal spacer will be fabricated from magnesium to save weight (Fig. 17). The matrix is covered by the back-up plate and supported by a corrugated or honeycomb configuration. The back-up plate is dimpled sheet metal with perforations.

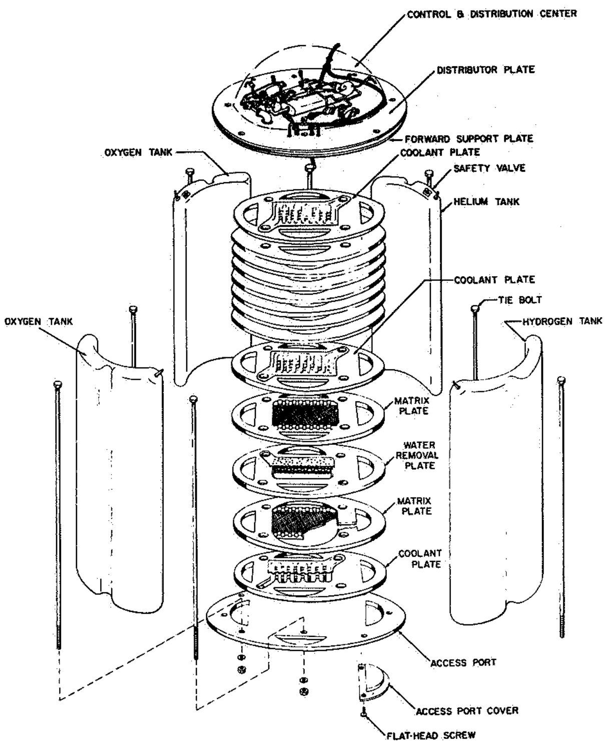

FIGURE 15. EXPLODED VIEW OF ADVANCED SYSTEM CONCEPT

The dimples insure good electrical contact with the electrode. The perforations provide channels between the water vapor in the reactant cavity and water removal cavity. The cavity is vented to the water removal manifold through two opposed corner ports under the welded arm of the back-up plates.

The cell will be cooled by internal cold plates mounted between each set of opposed matrix spacers on the oxygen side. The simplicity of the cold plates is shown in Figure 18. Coolant is circulated through the coolant passage and allowed to evaporate in this space. This spacer is also magnesium, but it is gold plated to protect against corrosion because the environment of the oxygen cavity is more corrosive than that of the hydrogen cavity. The oxygen back-up plate is sheet metal, which is welded around the edges and along the ribs of the coolant plate.

The overall schematic of the system given in Figure 19 illustrates the simplicity of the system. The system as shown must use either reactant gases or helium, precluding the possibility of air or impurities entering during a changeover of gas supplies. All external connections are made through quick

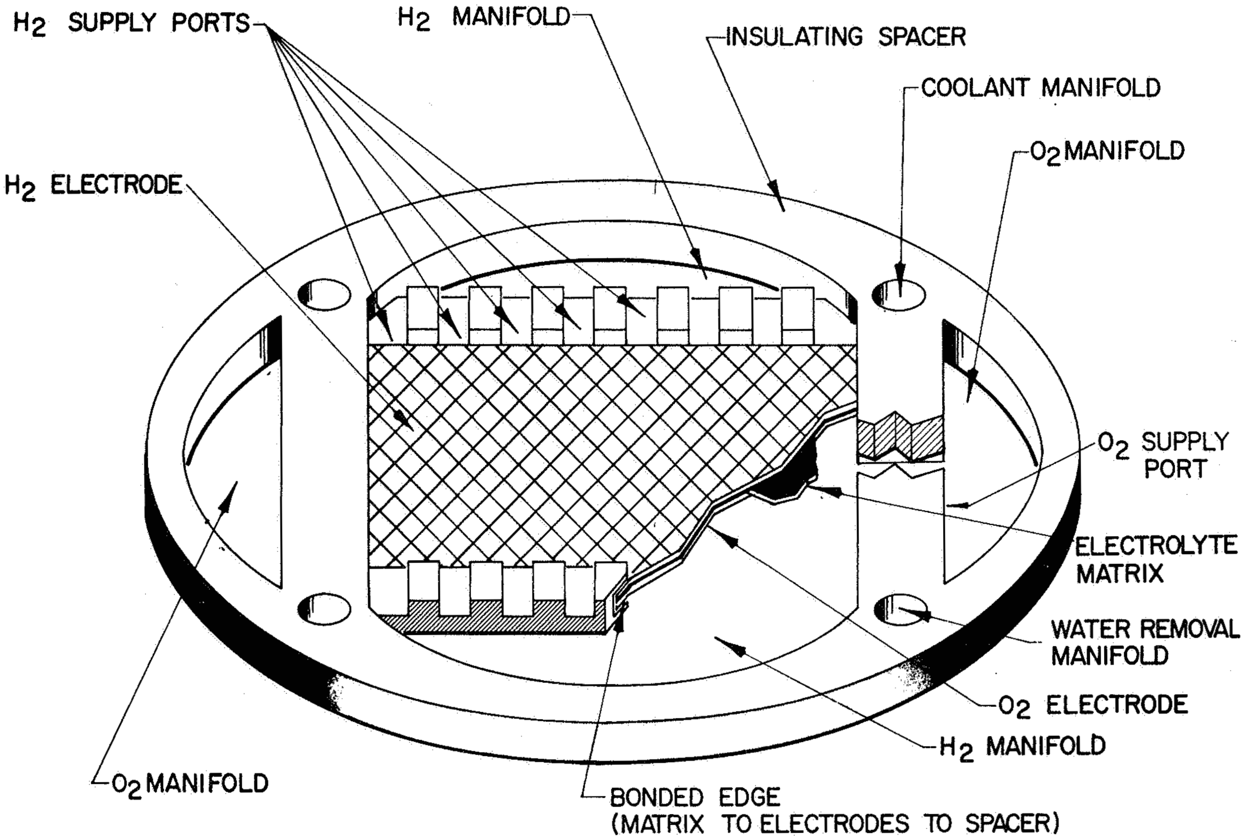

FIGURE 16. MATRIX SPACER

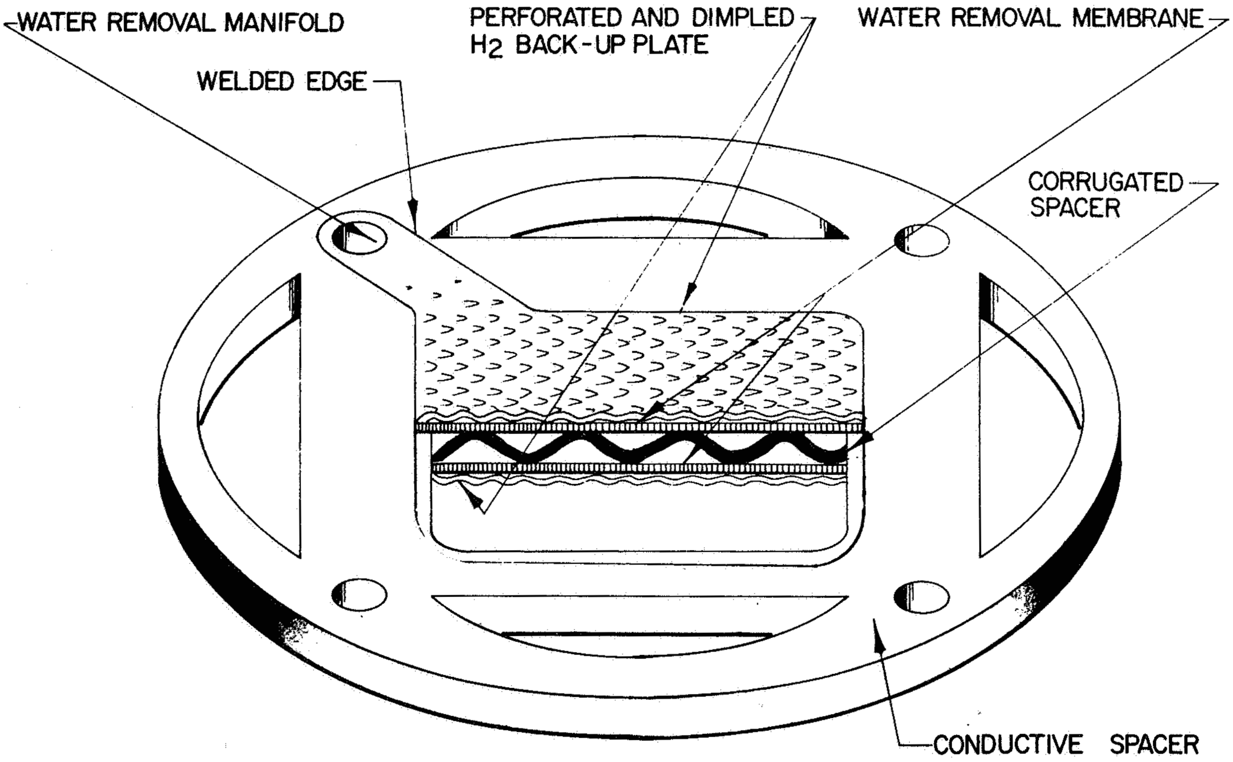

FIGURE 17. WATER REMOVAL SPACER

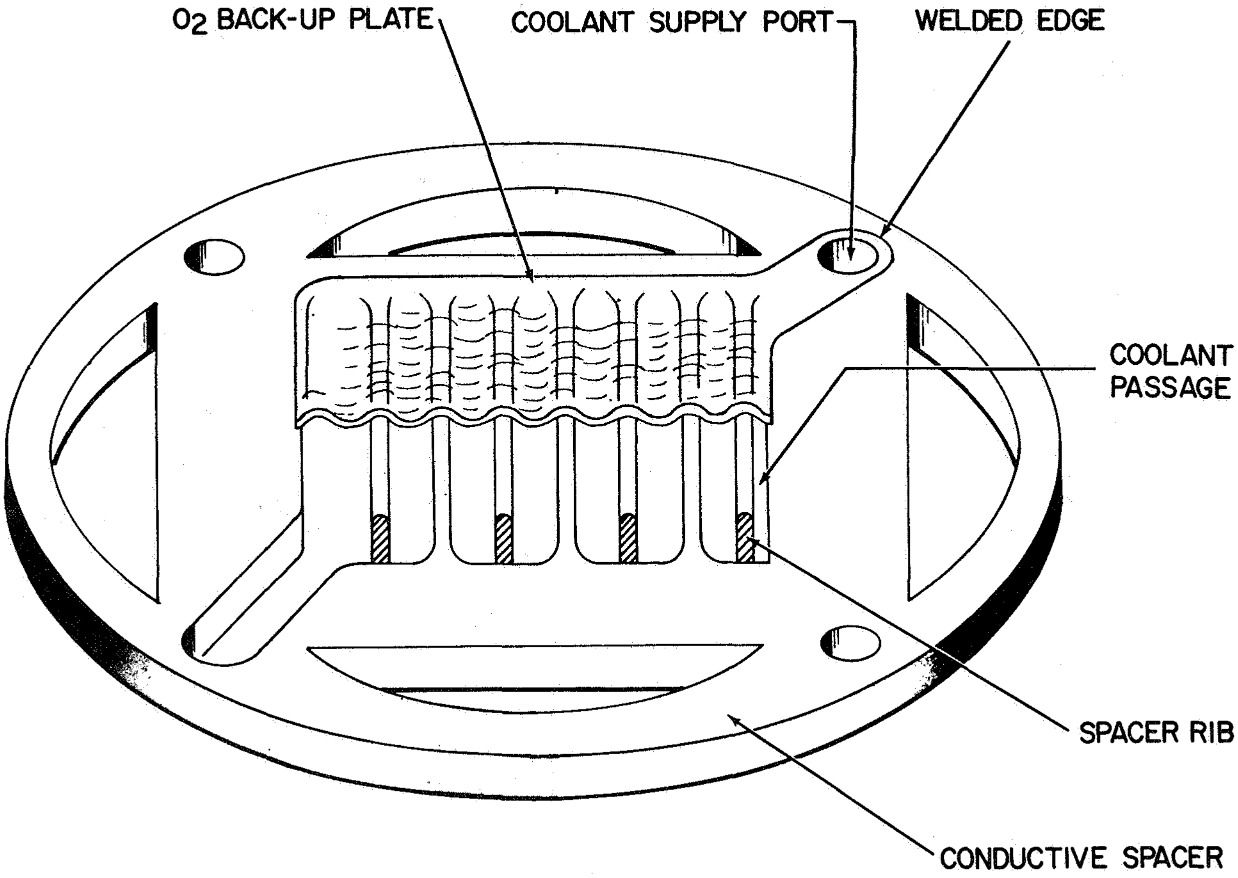

FIGURE 18. COOLANT SPACER

disconnect bulkhead fittings. The hydrogen and oxygen pressure regulators are referenced to the helium pressure regulator, as is the coolant system, and the helium regulator is referenced to the water cavity vacuum. This prevents over-pressurization of any cavity with respect to any other system cavity. The reactant cavities can both be purged with helium through a three-way solenoid on the vent side of the cell. One side of the supply line is opened to ambient pressure for purging. A similar device flushes the water removal cavity. The system warm-up is by means of an electrical in-line heater on the coolant system.

FUTURE PLANS

Future plans in the cell optimization study are to examine any possible improvements in performance obtained by changes in operational concepts. A cell operating on the cycle shown in Figure 20 uses product water to saturate the incoming oxygen. This should eliminate a shortage of water at the oxygen reaction zone, which appears to be a current limiting phenomenon. A single cell test stand has been designed and fabricated to evaluate this operational concept. The goal of the first test sequence is to evaluate the changes in polarization losses caused by saturation of the reactants with water. If water saturation of the inlet oxygen proves to be advantageous, a feasibility study will be initiated to investigate applying this operational concept to a full system.

A continuation of the environmental test program, initiating the load sharing analysis of the parallel test, and configuration of the single cell optimization study are future plans for inhouse testing. A continuation of the cold plate design evaluation, final design and fabrication of a fuel cell stack using a recirculating electrolyte, further analysis of electrode preconditioning techniques, and investigation of new concepts are future plans for contract research.

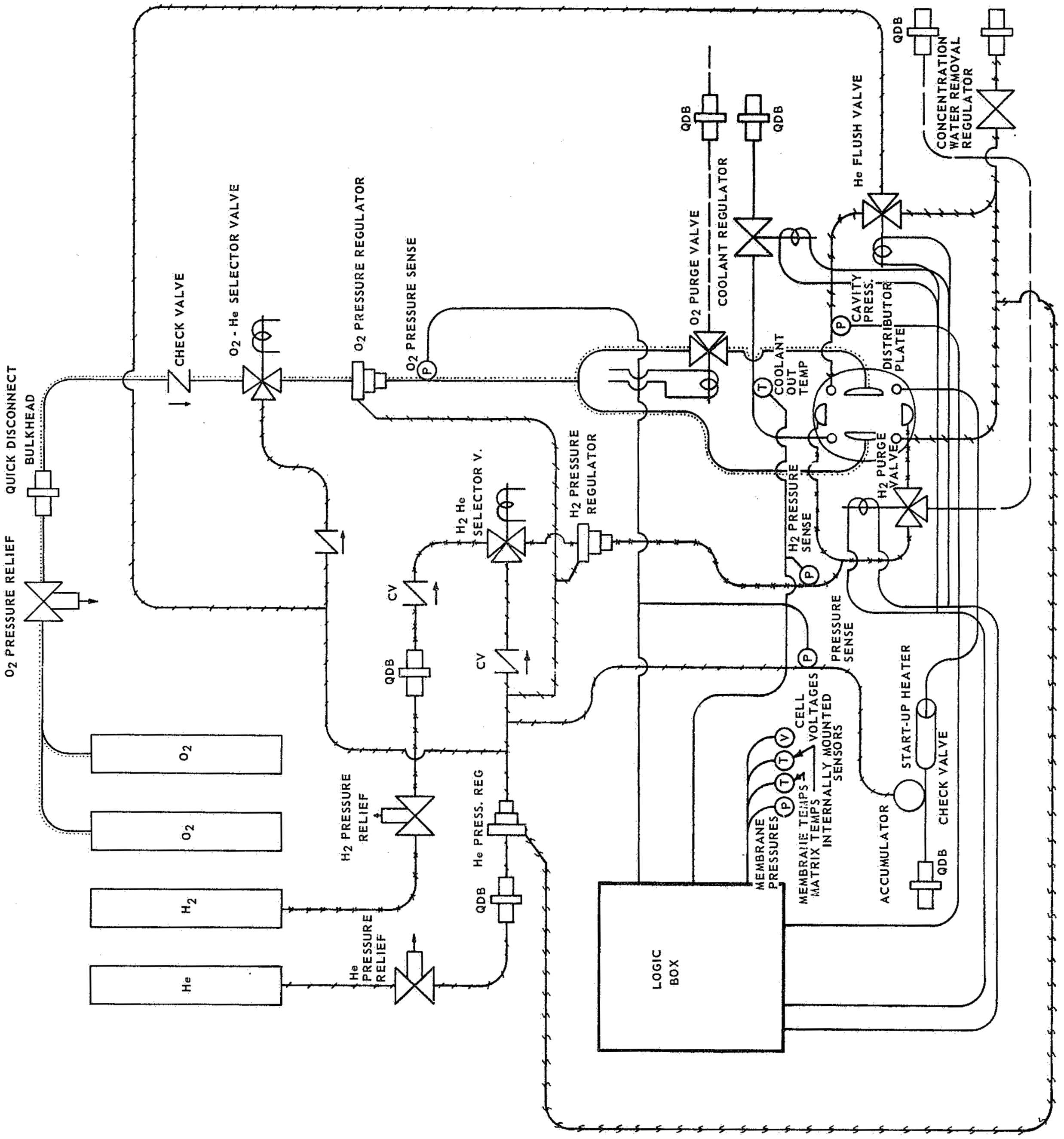
O2 PRESSURE RELIEF
QUICK DISCONNECT BULKHEAD
CHECK VALVE
O2 - He SELECTOR VALVE
O2 PRESSURE REGULATOR
O2 PRESSURE SENSE
O2 PURGE VALVE
COOLANT REGULATOR
QDB
QDB
He FLUSH VALVE
QDB
CONCENTRATION WATER REMOVAL REGULATOR
CAVITY PRESS.
DISTRIBUTOR PLATE
COOLANT OUT TEMP
H2 PURGE VALVE
H2 PRESSURE SENSE
H2 PRESSURE REGULATOR
H2 He SELECTOR V.
CV
CV
QDB
PRESSURE SENSE
START-UP HEATER
CHECK VALVE
QDB
ACCUMULATOR
CELL VOLTAGES
MEMBRANE TEMPS
MATRIX TEMPS
INTERNALLY MOUNTED SENSORS
MEMBRANE PRESSURES
P
T
T
V
P
T
P
P
P
LOGIC BOX
O2
O2
H2
He
H2 PRESSURE RELIEF
He PRESS. REG
QDB
He PRESSURE RELIEF

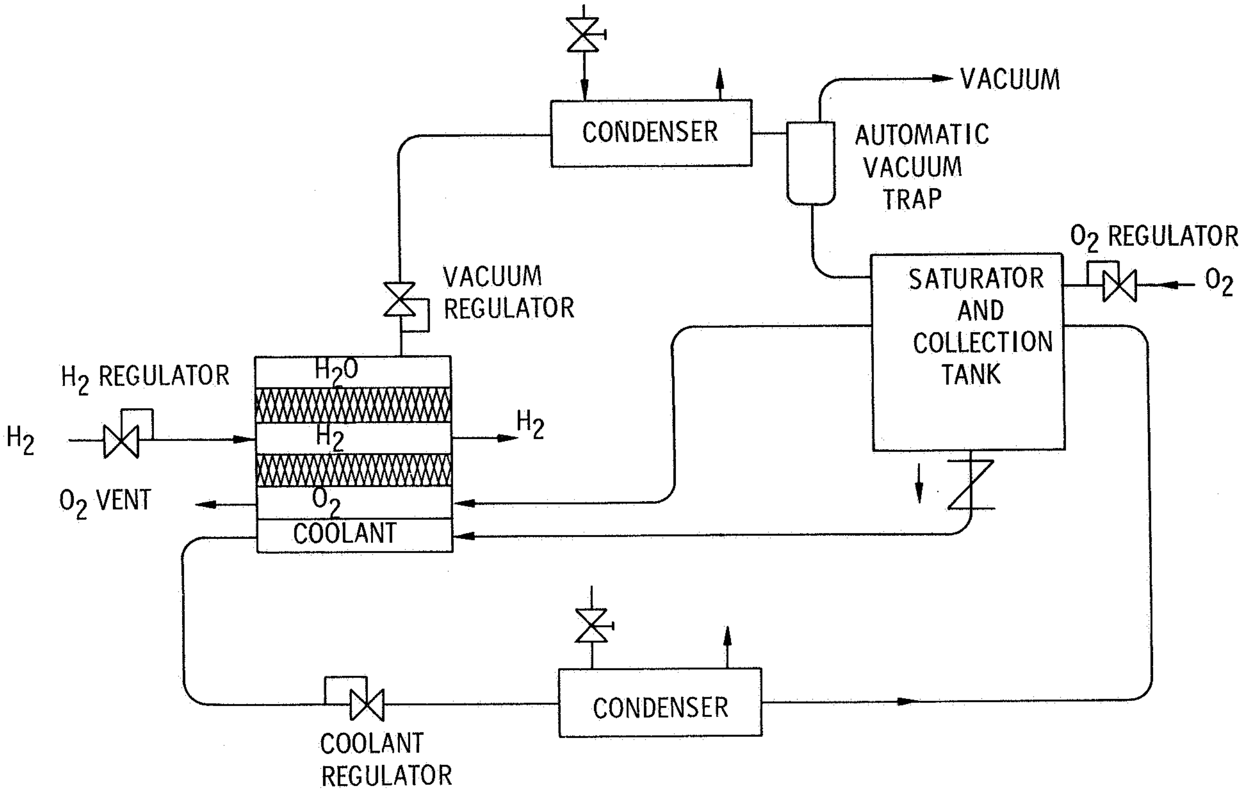

FIGURE 20. ADVANCED OPERATIONAL CONCEPT SCHEMATIC

STUDY OF RADIOISOTOPE POWER FOR SATURN APPLICATIONS

By

Jimmy L. Miller

INTRODUCTION

The operating capability of the present Saturn Instrument Unit (IU) is limited by the 6-1/2 hr lifetime of the primary battery power source. This powered interval for the IU is adequate for Apollo lunar missions as they are presently defined. However, considering the vast amount of guidance and communication gear contained within the IU and carried into orbit, the flexibility offered by a longer life power system such as a radioisotope power system would permit significant upgrading of mission concepts.

Radioisotope thermoelectric power systems ranging from a few tens of watts to a few hundred watts are under development in AEC sponsored programs and will become flight qualified in the next 3 to 5 years. Depending upon progress in fuel form technology, radioisotope thermionics may or may not ever become available in any size. Reactor thermionics in larger sizes (100 kW or larger) will undoubtedly become available in the late 1970's.

POWER REQUIREMENTS

A feasibility study was conducted in 1965 to determine if radioisotopically generated electrical power would be suitable for space vehicle applications. The present peak IU electrical load during launch is slightly in excess of 3 kW, and peak load for the orbital workshop is approximately 2 kW. Based on these criteria, the requirement for a radioisotope power source of 2 kW was established. This would essentially provide the total power requirement for missions like the 56-day workshop, with the possible advantage of direct radioisotope thermal energy for heating. The 2 kW power level would increase Apollo mission flexibility by extending the IU operational lifetime in earth orbit. The primary battery would only be used when supplying the peak loads (above 2 kW required during the launch phase).

In choosing a location on the Saturn vehicle for the radioisotope system, there were three primary considerations: (1) space available for radiators, (2) allowable heat loss to the Saturn vehicle, and (3) ease of nuclear shielding. Tradeoff studies quickly revealed that the aft Saturn Lem Adapter (SLA) was the most feasible location for the radioisotope system. There was sufficient area at this point to support large radiators, and the heat loss into the Saturn systems may be maintained within allowable limits. The SLA location minimizes the major hazards that would exist if the heat source were located adjacent to the S-IVB LOX or liquid hydrogen tanks. In addition, the SLA is adjacent to the IU and may logically remain attached to it in any mission which uses the radioisotope power system.

In terms of converter system selection, the 2 kW power level required large system technology. The SNAP 29 system was chosen as the basis for the study because of its desirable geometry, high power, and advanced state of development.

SNAP 29 GENERATOR

The SNAP 29, shown in Figure 1, is a 500 W generator using Po^{210} fuel and is under development by the Martin Company. It is designed to have an operational life of 104 days. This life span will provide a 90-day space life after operation at the launch pad for up to 14 days.

There are essentially five subsystems composing the SNAP 29.

1. Heat source fuel block contains the Po^{210} and measures approximately 83. 9 by 94. 0 by 2. 54 cm (33 by 37 by 1 in.). The fuel block is designed for intact reentry and containment of the fuel under normal atmospheric reentry or for any abort situation. It will also withstand impact against any substance and burial in any location without loss of radioactive material.

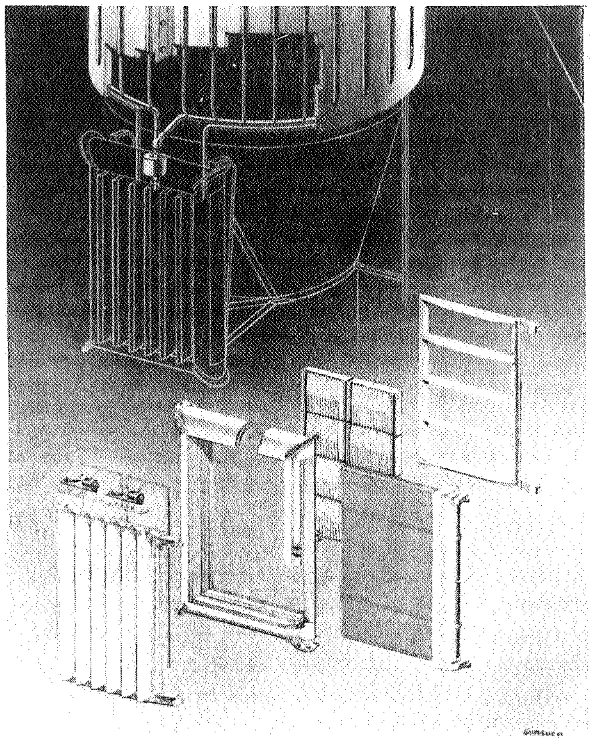

FIGURE 1. SNAP 29 COMPONENTS

2. Thermoelectric conversion subsystem consists of eight modules, each of which produces 62.5 W of electrical power. Each module contains 82 Pb Te conversion elements and has dimensions 38.1 by 20.3 by 6.35 cm (15 by 8 by 2.5 in.).

3. Thermal control subsystem consists of six thermal shutters with mechanical linkage to an actuating device. This temperature sensing actuation device is driven by NaK fluid coupled to the hot plate of the module. Contraction and expansion of the NaK through a bellows-piston mechanism operates the shutters. As the fuel ages and produces less heat, the shutters are gradually closed to maintain a constant electrical output.

4. Heat rejection subsystem consists of about 7.9 m^2 (85 ft^2) of radiator surface and a NaK coolant loop driven by electromagnetic (EM) pumps. The radiator geometry may be tailored to fit the spacecraft configuration.

5. Structural subsystem consists primarily of a frame that will break apart during reentry to allow the fuel block to reenter separately.

Four SNAP 29 systems mounted on the aft SLA almost fill the entire SLA area with radiator (Fig. 2). Each system will be located in the center of its radiator quadrant with one half of the NaK flow going through each side of the radiator. The net electrical power will be 2 kW.

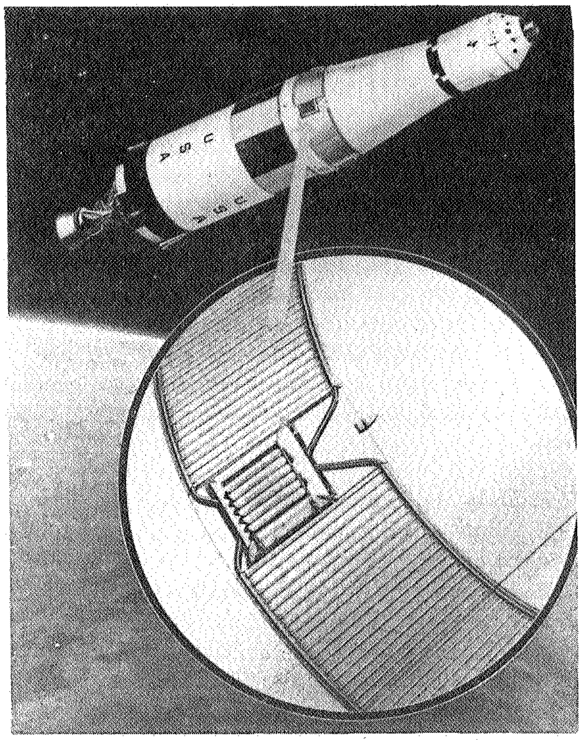

FIGURE 2. RADIOISOTOPE POWER SUPPLY ON SATURN VEHICLE

SYSTEM ANALYSIS AND DESCRIPTION

Valid analytical data are obtained when engineering analysis and computer results are verified by detailed design, fabrication, and testing. The objectives of the present program are to (1) complete a design of the selected approach, (2) fabricate a simulation test article, (3) demonstrate the feasibility of the approach by testing, and (4) define criteria unique to RTG applications which directly influence their use.

Certain basic assumptions that reflected directly upon the design study were made. To assure the utility of the system, little or no modifications to the existing and flight qualified SLA structure should be needed. The design analysis should not decrease the load carrying capability or change the structural integrity of the system. The allowable thermal loss into the SLA honeycomb would be a maximum of 250 W per SNAP 29 system, or a maximum of 1000 W additional heat into the IU compartment. This insures that the SLA honeycomb will remain at a relatively low temperature. The system must withstand the prelaunch environment and launching stresses. The radiator must be operating for some period of time inside the service structure on the launch pad. This phase of operational considerations has not been extensively investigated to date, but will be the subject of a later study.

A requirement of the SNAP 29 system is that the fuel block must separate from the SLA during reentry. The SNAP 29 system will be mounted on the outside of the SLA to have the generator frame in the airstream so that it may break away and fall free of other hardware when aerodynamic heating begins. The aerodynamic design of the fuel block assures that it will reenter intact after it separates from the SLA. The only necessary SLA modifications are some mounting holes at the attachment points. The external location does require an aerodynamic shroud for vehicle launch, and this shroud must be jettisoned in orbit or in the event of launch abort.

Present mission definitions call for the forward SLA shrouds to be opened back 45 degrees. This position was assumed in the study to calculate the effective radiator view factor. Obviously the forward shrouds could not be folded back all the way because of their interference with the radiator. The most desirable situation is for the forward SLA panels to be jettisoned. Using these basic assumptions, a preliminary design has been worked out which locates the SNAP 29 and associated radiator on a quadrant of the aft SLA.

Figure 3 shows the split radiator sections with the generator system located between the radiator segments. The NaK loop flows into and returns from the radiator sections through 2.54 cm (1.0 in.) outside diameter, 2.44 cm ID (0.96 in. ID) header tubes. The vertical radiator tubes are 0.7938 cm (0.3125 in.) outside diameter, 0.6922 cm (0.2725 in.) ID and are

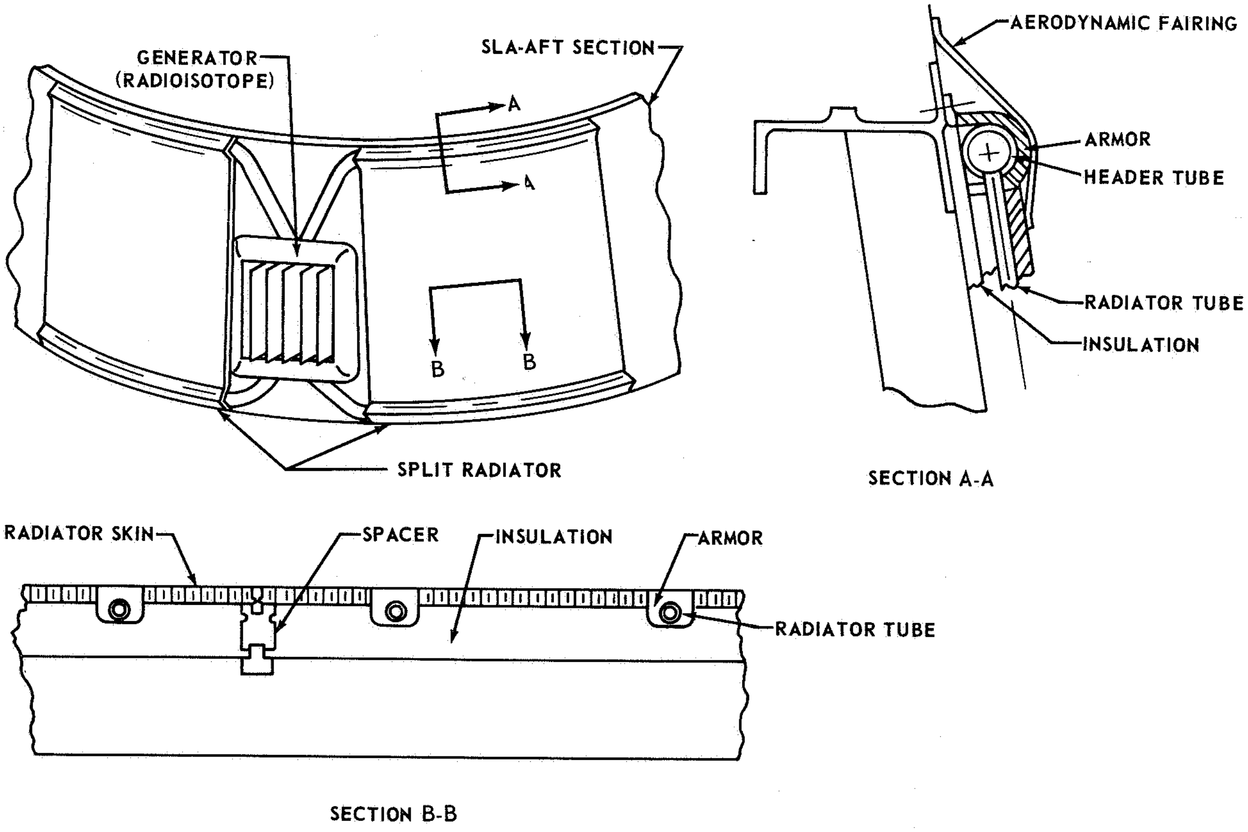

FIGURE 3. RADIATOR FLIGHT CONFIGURATION

spaced 11.8 cm (4.63 in.) between centers out of the top header. Because of the conical geometry of the radiator, the tube spacing increases down their 2.13 m (7 ft) length and enters the bottom header on 13.0 cm (5.11 in.) spacing between centers. The primary structural support for the radiator is through the bolting of the header armor brackets into the top and bottom SLA rings. The radiator skin is spaced away from the SLA skin by 40 insulated standoff fasteners. The total radiator thermal dissipation is approximately 10 kW, and the NaK flow rate required to accomplish this energy transfer is 2100 kg/hr (4620 lb/hr). The flow maldistribution down the radiator tubes is calculated to be ±3.5%, which is within a tolerable limit.

To meet the objective of 250 or less thermal watts lost to the SLA, an insulating material will be required between the radiator and SLA honeycomb.

A number of insulating materials were studied. Figure 4 shows a comparison among dimpled H-film, eccofoam, and thermoflex, which were three of the more promising materials. The insulating material needs to be lightweight and have a low coefficient of thermal conduction. Therefore, as a comparison basis, the product of thermal conductivity and density was used. Dimpled H-film appeared to be considerably superior.

MATERIAL	k $\frac{W}{m^2 \cdot {}^\circ K}$ 366°K $\left[k \left(\frac{Btu}{hr \cdot ft^2 \cdot {}^\circ F} \right) (200^\circ F) \right]$	ρ $\frac{kg}{m^3}$ 366°K $\left[\rho \left(\frac{lb}{ft^3} \right) (200^\circ F) \right]$	$k\rho$
DIMPLED H-FILM	0.00284 (0.0005)	43.3 (2.7)	0.123 (0.00135)
ECCOFOAM	0.068 (0.012)	32.0 (2.0)	2.18 (0.024)
THERMOFLEX	0.159 (0.028)	48.0 (3.0)	7.64 (0.0785)

FIGURE 4. RADIATOR INSULATION SELECTION

To maintain the SLA temperature at around 366°K (200°F) with the radiator at 450°K (350°F), the insulation must consist of 6 layers of dimpled H-film. This number of layers can be compressed into a blanket about 0.254 cm (0.1 in.) thick and placed between the radiator backside and the SLA skin as shown in Figure 5.

Two problems remain to be investigated. One is the method for removing heat on the launch pad where the dimpled H-film is filled with air and does not perform at its peak efficiency as an insulating blanket. The other is a potential problem of shifting or tearing of the H-film during launch when the insulating blanket is being evacuated. To investigate the second problem, a rapid pull-down vacuum test on a specimen is planned for some time in the future.

During the thermal cycle of the radiator, a differential expansion will take place between the radiator and SLA. Assuming a difference in temperature of 366°K (200°F) on the SLA to 450°K (350°F) on the radiator, the differential expansion could be as high as 0.726 cm (0.286 in.). To allow for this expansion, slotted mounting points were provided at the four corners at an angle with the horizontal that would allow proportional expansion in the vertical and horizontal directions. During launch, this mounting permits the aerodynamic loads to be transmitted to the SLA structure.

A loose fit between the top header and the header armor permits the differential expansion motion without strain. The problem in this design is that sheer stresses act on the weld between the header and radiator tubes.

The NaK radiator tubes must be stainless steel to contain the NaK, and the radiator and armor are aluminum. Therefore, a stainless steel to aluminum bond is required for the 2.13 m (7 ft) long radiator tubes. This is accomplished by nickel plating the stainless steel and then casting in aluminum. The casting is then machined into the cross-section, shown in Figure 6, and welded to the inside of the radiator plate.

For the thermal test model, a number of temperature channels as well as flow distribution channels will be provided. With the thermocouples placed in line (Fig. 6) effective thermal conductivities across the entire structure may be obtained.

Recent studies on the SNAP 29 heat rejection subsystem have resulted in direction by the AEC to switch the design from a circulating NaK loop to a multiple "water heat pipe" system. The radiator

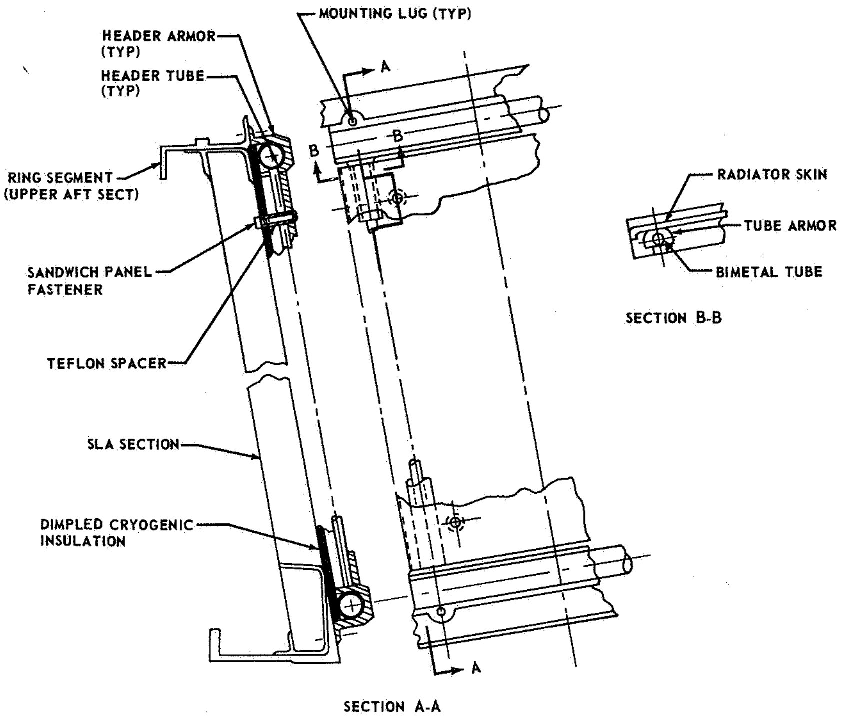

FIGURE 5. SATURN RADIATOR

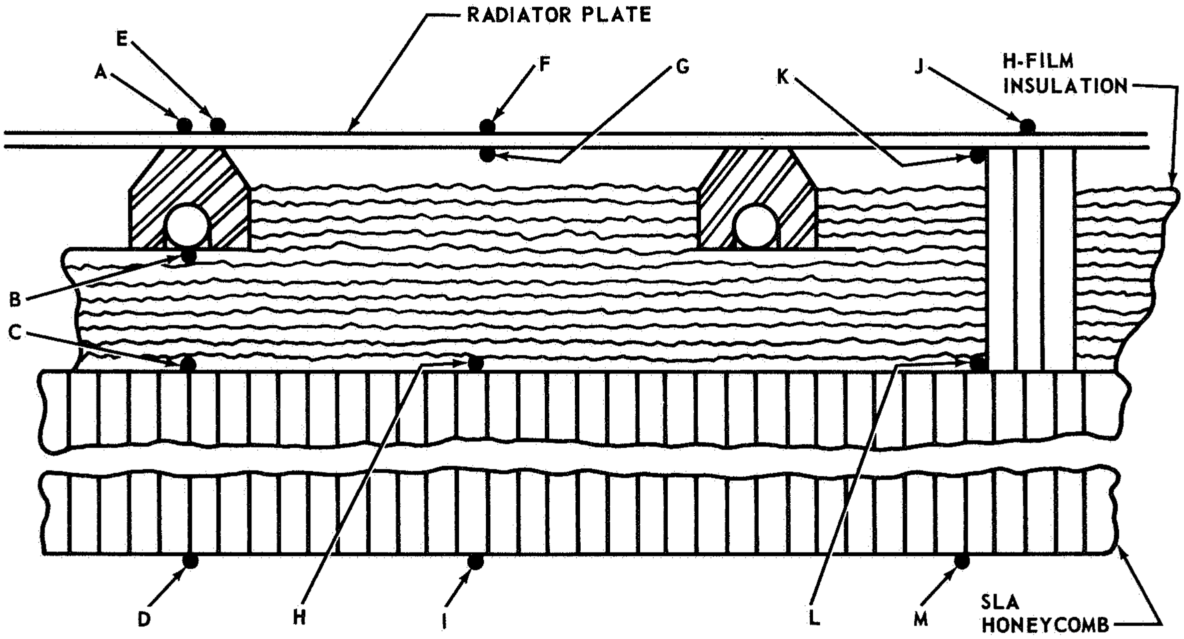

FIGURE 6. THERMOCOUPLE LOCATIONS ON RADIOISOTOPE POWER SUPPLY

area requirements will remain essentially unchanged, but the simple approach of using heat pipes will result in the elimination of header tubes. As a result, the problem of shear stresses between the header and radiator tubes is eliminated. The heat pipes will be essentially the same diameter as the radiator tubes, but instead of running vertically they will extend horizontally around the circumference of the radiator. Since each heat pipe functions independently of the others in the system, a high reliability factor may be achieved by adding redundant pipes and permitting a greater probability of puncture by meteoroids. This eliminates the requirement for meteoroid armor and will result in a much lighter system.

As the heat pipe design tradeoffs are completed, the results will be fed into the Saturn system study and the test article design will be modified. After all tradeoff decisions have been finalized, the radiator simulator will be fabricated. The unit will then be tested under ambient conditions and later under environmental conditions.

When a mission requirement for a radioisotope power system on Saturn vehicles is defined, the problem of vehicle launch operations will be investigated. Figure 7 shows one concept of a shielded fueling device. This device will weigh about 2720 kg (6,000 lb) and will consist of a tool for extracting the electrical checkout heaters from the SNAP 29 and inserting the Po^{210} fuel block. This operation is performed just prior to launch for obvious reasons of nuclear safety.

FUTURE PLANS

Future plans include the investigation of radioisotope handling and safety. The safety program will be extensive and will be performed for six event phases as follows: (1) handling, storage, and transportation, (2) launch pad, (3) launch and ascent, (4) orbit, (5) reentry, and (6) impact. Future plans will require investigating launch pad support equipment and operational problems. It is conceivable that a mission readiness date as early as fall of 1971 could be realized for a radioisotope electrical power system for Saturn vehicles.

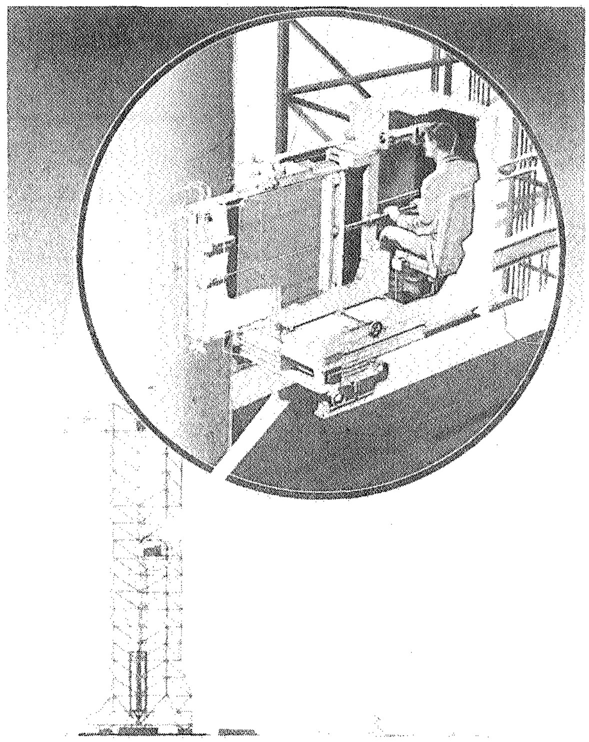

FIGURE 7. SNAP 29 FUELING DEVICE

STUDY OF SOLAR POWER WITH GRAVITY GRADIENT STABILIZATION

By

Leighton Young

SUMMARY

A method for predicting the amount of power available from a solar array in circular orbit and under gravity gradient stabilization is presented. Six possible solar array orientations are discussed. Equations derived can be modified to fit an infinite number of orientations. Oscillatory conditions are not investigated, but the equations derived can be helpful in determining useful solutions for such situations.

INTRODUCTION

Power from a solar array in "Air Mass 0" sunlight depends upon the electrical power rating of the array, array temperature, and the angle of incident sunlight, as summarized in the following equation:

$$P_0 = P_r \tau A \qquad (1)$$

where P_0 = output power (to be determined)

P_r = power rating of the array

τ = normalized temperature power coefficient

A = normalized effective array area

The array power rating is determined from design parameters. Three factors remain to be resolved before output power can be determined.

1. Temperature Effects - Array temperature variations must be known before τ (normalized temperature power coefficient) can be determined.

2. Angle of Incident Sunlight - The cosine of this angle is the normalized effective array area (A in eq. (1)).

3. Entrance and Exit Points into the Earth's Shadow - The period of orbit when the satellite is in the earth's shadow must be known so that solar array power can be equated to zero.

A detailed discussion of each of these controlling factors follows.

TEMPERATURE EFFECTS

Temperature variations experienced by a solar array in near earth orbit will be similar to those shown in Figure 1. For this range of temperatures, array power varies with temperature in an approximately linear fashion (0.5% per degree Kelvin) as shown in Figure 2. Here τ is normalized at 343°K and is read from the right ordinate of the curve. By taking temperatures from Figure 1, and obtaining the corresponding τ from Figure 2, a curve can be plotted for τ over the range of temperature experienced by the solar array.

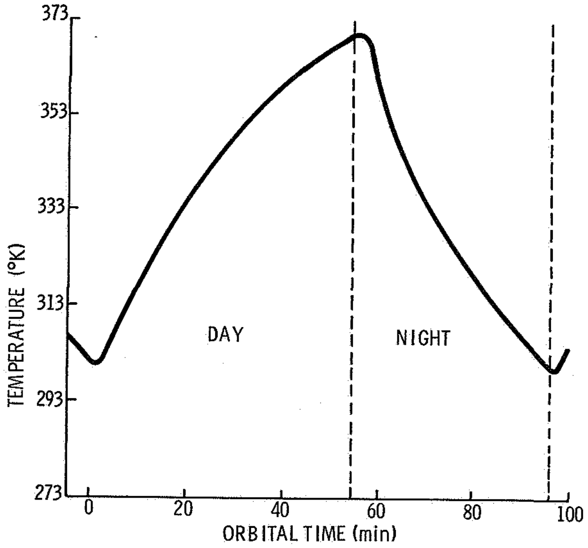

FIGURE 1. TEMPERATURE VS. ORBITAL TIME FOR A NOMINAL ORBIT

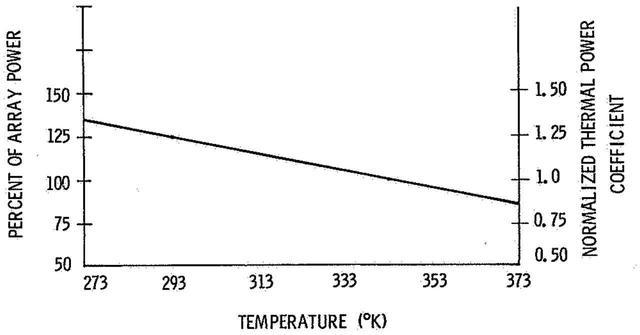

FIGURE 2. NORMALIZED THERMAL POWER COEFFICIENT

If τ is equated to zero during the time the array is in the earth's shadow, the curve will appear as shown in Figure 3. If average power is desired rather than instantaneous power, an average value for τ may be used in the formula $P_0 = P_r \tau A$.

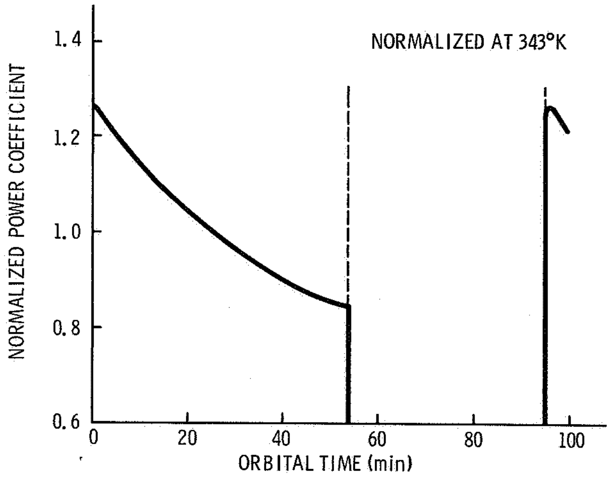

FIGURE 3. THERMAL POWER COEFFICIENT (τ)

DETERMINATION OF ANGLE OF INCIDENT SUNLIGHT

This method for determination of the angle of incident sunlight considers the satellite as being a cube in orbit with the possibility of the solar array being mounted on either of the cube's six surfaces as shown in Figure 4. The array could be pointed in either of six directions as described by vectors $\vec{N}_1$ through $\vec{N}_6$. The location of the satellite in relation to earth is defined by angles i, Ω, and Θ, which are referenced to the equatorial plane. The angle of inclination of the orbital plane is i, Ω is the angle between the X axis and the line of nodes (the line of nodes being the line drawn through the points where the satellite intersects the equatorial plane), and Θ is the angle between the line of nodes and the earth-satellite vector. To locate the satellite in reference to the sun, another angle must be used. This angle is called α and is measured from the vernal equinox as shown in Figure 5. Power available from a solar

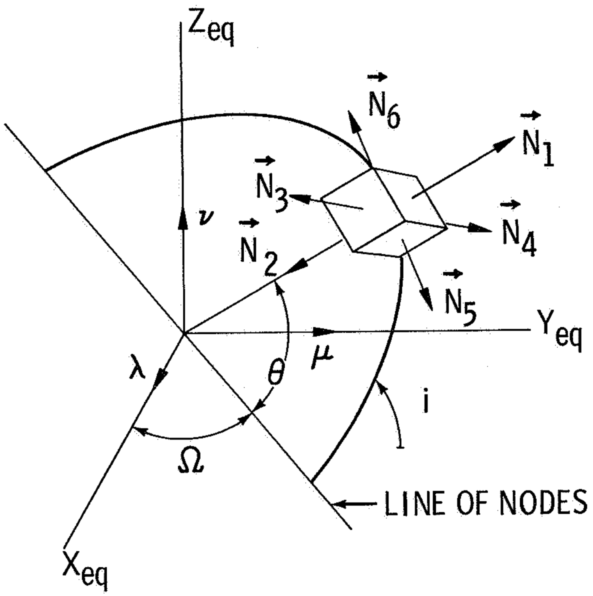

FIGURE 4. REFERENCE COORDINATES FOR CUBE IN EARTH ORBIT

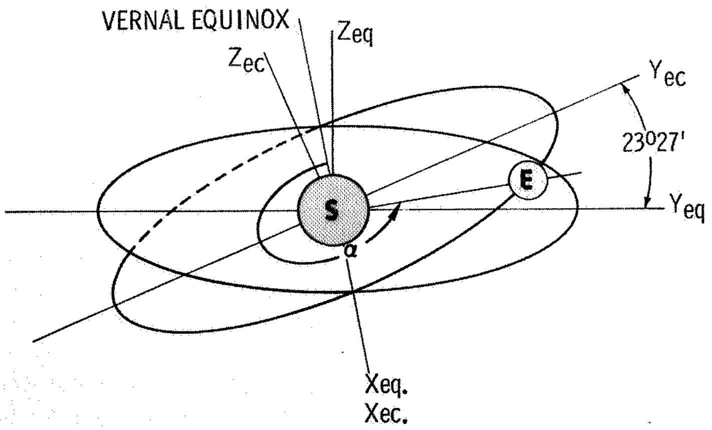

FIGURE 5. EQUATORIAL AND ECLIPTIC PLANES

array under gravity gradient stabilization in circular orbit of the earth is a function of α.

NORMALIZED EFFECTIVE ARRAY AREA

In the equation $P_0 = P_r \tau A$, P_r is the array power rating under the following conditions:

- "Air Mass 0."
- Temperature corresponding to the value 1.0 for τ (normalized temperature power coefficient).
- Direct incident sunlight - Sun vector normal to the surface of the solar array.

The normalized effective array area, A, is the cosine of the angle of incident sunlight. A method of solving for A is given by the dot product:

$$A_m = \vec{N}_m \cdot \vec{S}$$

$$\vec{N}_m \cdot \vec{S} = N_m S \cos\left(\angle \vec{N}_m \vec{S}\right) \qquad (2)$$

The value 1.0 is assigned to $N_m S$ since, by definition, A_m equals the cosine of the angle between the two vectors.

The steps necessary to arrive at A are as follows.

1. Mathematically define the relation between equatorial coordinates and ecliptic coordinates. From Figure 6 the following equations are obtained:

$$X_{eq} = X_{ec}$$

$$Y_{eq} = Y_{ec} \cos 23°27' - Z_{ec} \sin 23°27' \qquad (3)$$

$$Z_{eq} = Y_{ec} \sin 23°27' + Z_{ec} \cos 23°27'$$

$$\sin 23°27' = 0.39795$$

$$\cos 23°27' = 0.91741$$

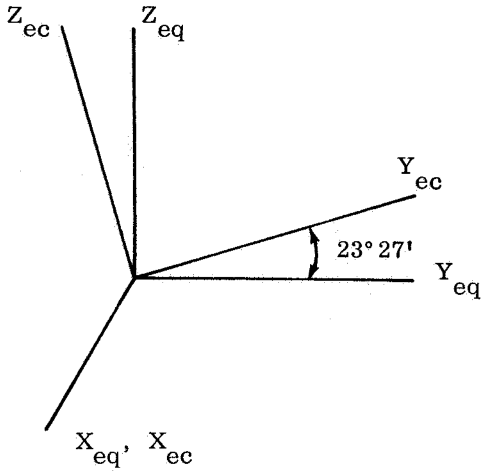

FIGURE 6. EQUATORIAL AND ECLIPTIC COORDINATES

In matrix form the relation becomes:

$$\begin{vmatrix} X_{eq} \\ Y_{eq} \\ Z_{eq} \end{vmatrix} = \begin{vmatrix} 1 & 0 & 0 \\ 0 & 0.9174 & -0.3979 \\ 0 & 0.3979 & 0.9174 \end{vmatrix} \begin{vmatrix} X_{ec} \\ Y_{ec} \\ Z_{ec} \end{vmatrix} \qquad (4)$$

2. Define the sun vector in terms of rectangular component vectors using equatorial coordinates. The following equations, obtained from Figure 7, define the sun vector in terms of its rectangular component in the ecliptic plane.

$$S_{X_{ec}} = S \cos \alpha$$

$$S_{Y_{ec}} = S \sin \alpha \qquad (5)$$

$$S_{Z_{ec}} = 0$$

The transformation to equatorial coordinates is shown by the following relations:

$$\begin{vmatrix} S_{X_{eq}} \\ S_{Y_{eq}} \\ S_{Z_{eq}} \end{vmatrix} = \begin{vmatrix} 1 & 0 & 0 \\ 0 & 0.9174 & -0.3979 \\ 0 & 0.3979 & 0.9174 \end{vmatrix} \begin{vmatrix} S_{X_{ec}} \\ S_{Y_{ec}} \\ S_{Z_{ec}} \end{vmatrix} \qquad (6)$$

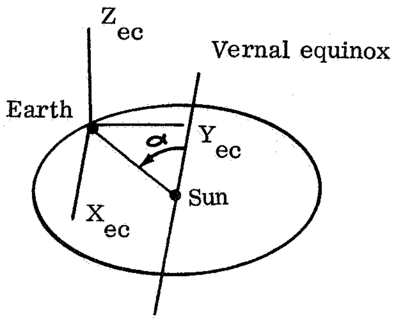

FIGURE 7. ECLIPTIC COORDINATE SYSTEM

Substituting for $S_{X_{ec}}$, $S_{Y_{ec}}$, and $S_{Z_{ec}}$:

$$\begin{vmatrix} S_{X_{eq}} \\ S_{Y_{eq}} \\ S_{Z_{eq}} \end{vmatrix} = \begin{vmatrix} 1 & 0 & 0 \\ 0 & 0.9174 & -0.3979 \\ 0 & 0.3979 & 0.9174 \end{vmatrix} \begin{vmatrix} S \cos \alpha \\ S \sin \alpha \\ 0 \end{vmatrix} \qquad (7)$$

$$\begin{aligned} S_{X_{eq}} &= S \cos \alpha \\ S_{Y_{eq}} &= 0.9174 \left(S \sin \alpha\right) \\ S_{Z_{eq}} &= 0.3979 \left(S \sin \alpha\right) \end{aligned} \qquad (8)$$

The sun vector described in the equatorial coordinate system is

$$\vec{S} = S_{X_{eq}} \vec{i} + S_{Y_{eq}} \vec{j} + S_{Z_{eq}} \vec{k} \qquad (9)$$

3. Define the vector normal to the solar array in terms of rectangular components using equatorial coordinates. Using λ_m, μ_m, and ν_m to represent the X, Y, and Z components respectively of $\vec{N}_m$ (Fig. 4), the following equations are obtained. The method used to obtain these equations is treated by Escobal [1].

For $\vec{N}_1$ and $\vec{N}_2$

$$\begin{aligned} \lambda_1 &= (\cos \Theta \cos \Omega - \sin \Theta \cos i \sin \Omega)\ N_1 \\ \mu_1 &= (\cos \Theta \sin \Omega + \sin \Theta \cos i \cos \Omega)\ N_1 \\ \nu_1 &= N_1 \sin \Theta \sin i \end{aligned} \qquad (10)$$

and since $\vec{N}_2 = -\vec{N}_1$

$$\begin{aligned} \lambda_2 &= (-\cos \Theta \cos \Omega + \sin \Theta \cos i \sin \Omega)\ N_1 \\ \mu_2 &= (-\cos \Theta \sin \Omega - \sin \Theta \cos i \cos \Omega)\ N_1 \\ \nu_2 &= -N_1 \sin \Theta \sin i. \end{aligned} \qquad (11)$$

For $\vec{N}_3$ and $\vec{N}_4$

$$\begin{aligned} \lambda_3 &= N_3 \sin i \sin \Omega \\ \mu_3 &= -N_3 \sin i \cos \Omega \\ \nu_3 &= N_3 \cos i \end{aligned} \qquad (12)$$

and since $\vec{N}_4 = -\vec{N}_3$

$$\begin{aligned} \lambda_4 &= -N_3 \sin i \sin \Omega \\ \mu_4 &= N_3 \sin i \cos \Omega \\ \nu_4 &= -N_3 \cos i. \end{aligned} \qquad (13)$$

For $\vec{N}_5$ and $\vec{N}_6$

$$\begin{aligned} \lambda_5 &= (\sin \Theta \cos \Omega + \cos \Theta \cos i \sin \Omega)\ N_5 \\ \mu_5 &= (\sin \Theta \sin \Omega - \cos \Theta \cos i \cos \Omega)\ N_5 \\ \nu_5 &= -N_5 \cos \Theta \sin i \end{aligned} \qquad (14)$$

and since $\vec{N}_6 = -\vec{N}_5$

$$\begin{aligned} \lambda_6 &= (-\sin \Theta \cos \Omega - \cos \Theta \cos i \sin \Omega)\ N_5 \\ \mu_6 &= (-\sin \Theta \sin \Omega + \cos \Theta \cos i \cos \Omega)\ N_5 \\ \nu_6 &= N_5 \cos \Theta \sin i. \end{aligned} \qquad (15)$$

4. Obtain the dot product of the sun vector and the vector normal to the solar array.

$$A_m = \vec{N}_m \cdot \vec{S} \qquad m = 1, 2, 3, 4, 5, 6 \qquad (2)$$

where $N_m = \lambda_m \vec{i} + \mu_m \vec{j} + \nu_m \vec{k}$

$$\vec{S} = S_X \vec{i} + S_Y \vec{j} + S_Z \vec{k}$$

$$A_m = \lambda_m S_X + \mu_m S_Y + \nu_m S_Z \qquad (16)$$

Example: Find the equation for the normalized effective area for a solar array mounted on surface five of the orbiting cube under consideration. Given that $A_5 = \vec{N}_5 \cdot \vec{S}$, where $\vec{N}_5 = \lambda_5 \vec{i} + \mu_5 \vec{j} + \nu_5 \vec{k}$, and the equations for λ_5, μ_5, and ν_5 are as given under 3 above, take

$$S_X = S \cos \alpha$$
$$S_Y = 0.9174 \left(S \sin \alpha \right) \qquad (17)$$
$$S_Z = 0.3979 \left(S \sin \alpha \right)$$

so that

$$\lambda_5 S_X = \left[\left(\sin \Theta \cos \Omega + \cos \Theta \cos i \sin \Omega \right) N_5 \right] S \cos \alpha$$
$$\mu_5 S_Y = \left[\left(\sin \Theta \sin \Omega - \cos \Theta \cos i \cos \Omega \right) N_5 \right] 0.9174 S \sin \alpha$$
$$\nu_5 S_Z = \left(- N_5 \cos \Theta \sin i \right) 0.3979 S \sin \alpha \qquad (18)$$

and $N_5 S = 1.0$ by definition,

then

$$A_5 = \lambda_5 S_X + \mu_5 S_Y + \nu_5 S_Z \qquad (19)$$

where

$$\lambda_5 S_X = \left(\sin \Theta \cos \Omega + \cos \Theta \cos i \sin \Omega \right) \cos \alpha$$
$$\mu_5 S_Y = \left(\sin \Theta \sin \Omega - \cos \Theta \cos i \cos \Omega \right) 0.9174 \sin \alpha$$
$$\nu_5 S_Z = \left(- \cos \Theta \sin i \right) 0.3979 \sin \alpha. \qquad (20)$$

Equation (19) yields the normalized effective area for a solar array mounted on surface five of the cube at a specific point in orbit. If the normalized effective area is desired as a function of time, the following substitutions may be made:

$$\Theta = \Theta_0 + \dot{\Theta} t$$
$$\Omega = \Omega_0 + \dot{\Omega} t \qquad (21)$$
$$\alpha = \alpha_0 + \dot{\alpha} t$$

where

Θ_0, Ω_0, α_0 = initial space coordinates

$\dot{\Theta}$ = satellite's angular velocity around earth

$\dot{\Omega}$ = rate of orbit precession

$\dot{\alpha}$ = earth's angular velocity around sun

t = time in orbit.

DETERMINATION OF PERIOD OF EARTH'S SHADOWING

Figure 8 illustrates a satellite in circular orbit around the earth. An extension to the line drawn from the center of the earth to the entrance or exit point has the same direction and position in space as $\vec{N}_1$. Therefore when A_1, the dot product of $\vec{N}_1$ and $\vec{S}$, equals cosine ψ, the satellite is at either the entrance or exit point. When $A_1 <$ cosine ψ, the satellite is in the shadow of the earth and the normalized effective array area (A_m) is set equal to zero. All negative values of A_m are also set equal to zero since this indicates that sunlight would be shining on the rear of the solar array.

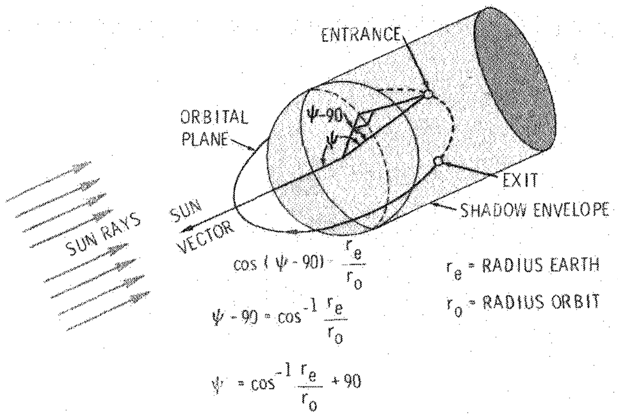

FIGURE 8. SATELLITE IN CIRCULAR ORBIT AROUND THE EARTH

Application to the Apollo Telescope Mount (ATM) of the method described in this paper over the period of one orbit gives results as shown in Figure 9. Sunlight shines on the rear of the solar array until t = 24 min and hence electrical power is not produced. At t = approximately 54 min the satellite reenters the shadow of the earth.

CONCLUSIONS

The equations that have been derived adapt well to a computer program. If the array orientation is at some attitude other than as defined by the faces of

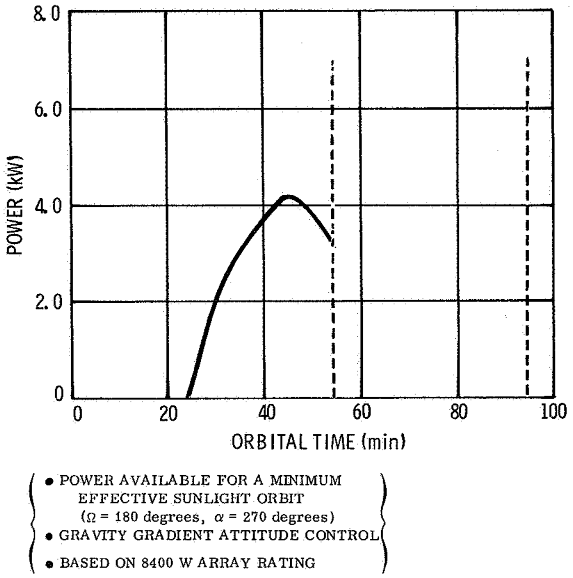

FIGURE 9. POWER CURVE FOR NOMINAL ORBIT

the cube, slight modifications to the equations must be made. Computer runs using ATM orbital parameters indicate that a solar array looking perpendicular to the plane of orbit could go for long periods of time without supplying any power. If the ATM should become gravity gradient stabilized with its solar array facing the earth, the solar array would be eclipsed by the earth during most of the time that it would normally be producing power. As different attitudes for ATM are given consideration, the method described in this paper is used to accurately determine the amount of solar array power available.

REFERENCE

1. Escobal, P. R.: Methods of Orbit Determination. John Wiley and Sons, Inc., New York, 1956.

METAL-ARC ILLUMINATOR FOR SOLAR ARRAY TESTING

By

William L. Crabtree

INTRODUCTION

Large area solar cell arrays are being designed to be an integral part of manned space vehicles. Solar arrays coupled with battery systems offer a reliable power supply for space vehicle applications.

Finding a method to obtain reliable test results to accurately predict solar cell array power outputs in space has long been a difficult problem for solar array design engineers. There are basically two approaches to the solution of this problem. The first approach makes use of a light source that accurately simulates the sun's spectrum and intensity at "Air Mass 0," which would be the condition at one astronomical unit in space. This type of source would actually cause the array to produce the same power that it would produce in space if it were located at one astronomical unit. Of the various types of sources that are used to accomplish this, probably the most successful is the mercury xenon lamp. Although mercury xenon does not provide the closest spectral match of any source, it does provide a reasonably good spectrum with a constant illumination, and this is difficult to obtain with light sources that more closely match the sun's spectrum.

The second approach makes use of a light source which simulates "Air Mass 1" conditions in the solar cell response region. This type of light source provides a simple, inexpensive means of determining the power output of the solar array without the need for the more expensive and usually more elaborate solar simulator. The power output of an array under this light source must be scaled up to determine the array's power output in space; this is usually done by relating the output of a primary standard cell (one which has flown in space) under this source to its output in space. The initial investigation of a light source of this type is the subject of this paper.

TUNGSTEN FILAMENT LAMP SOURCE

At present, the most widely accepted light source is the tungsten filament lamp. The problems associated with the use of the tungsten lamp are as follows:

1. Rapid Degradation - Normally, tungsten bulbs suited for solar array testing have a short lifetime, some as short as six hours; therefore, the bulbs must be replaced after only a few hours of operation.

2. Excessive Infrared Radiation - Tungsten lights have excessive emission near the infrared region, thus requiring a water filter to decrease this infrared before it reaches the test plane area.

3. High-Heat Generation - The excessive infrared generated by the tungsten lamp heats the simulator and requires that the water in the water filter be circulated to keep it cool.

Figure 1 shows the lamp that is presently being investigated as a potential light source for use in solar array testing. It is an arc discharge type of lamp containing the rare metal halide scandium iodide, which is contained in the quartz arc tube shown in the figure. These lamps are available in wattages of 175, 400, and 1000; those used in these initial investigations were the Sylvania 400 W type.

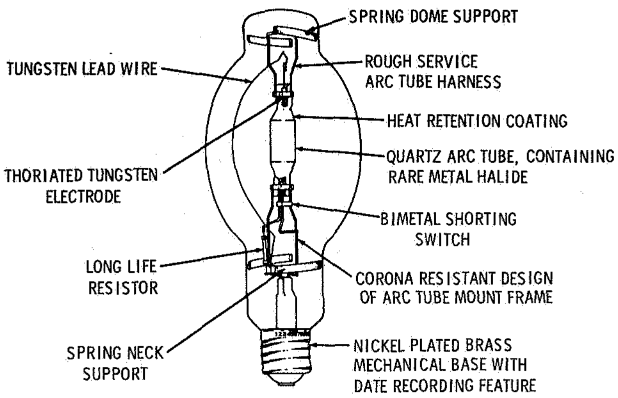

FIGURE 1. METAL-ARC LAMP

Figure 2 shows a comparison of spectral responses. The curve that begins at zero relative intensity and rises most rapidly is the sun's spectrum at "Air Mass 1," the curve with highest relative intensity is the tungsten spectrum unfiltered, and the curve under the filtered area shows the result of filtering

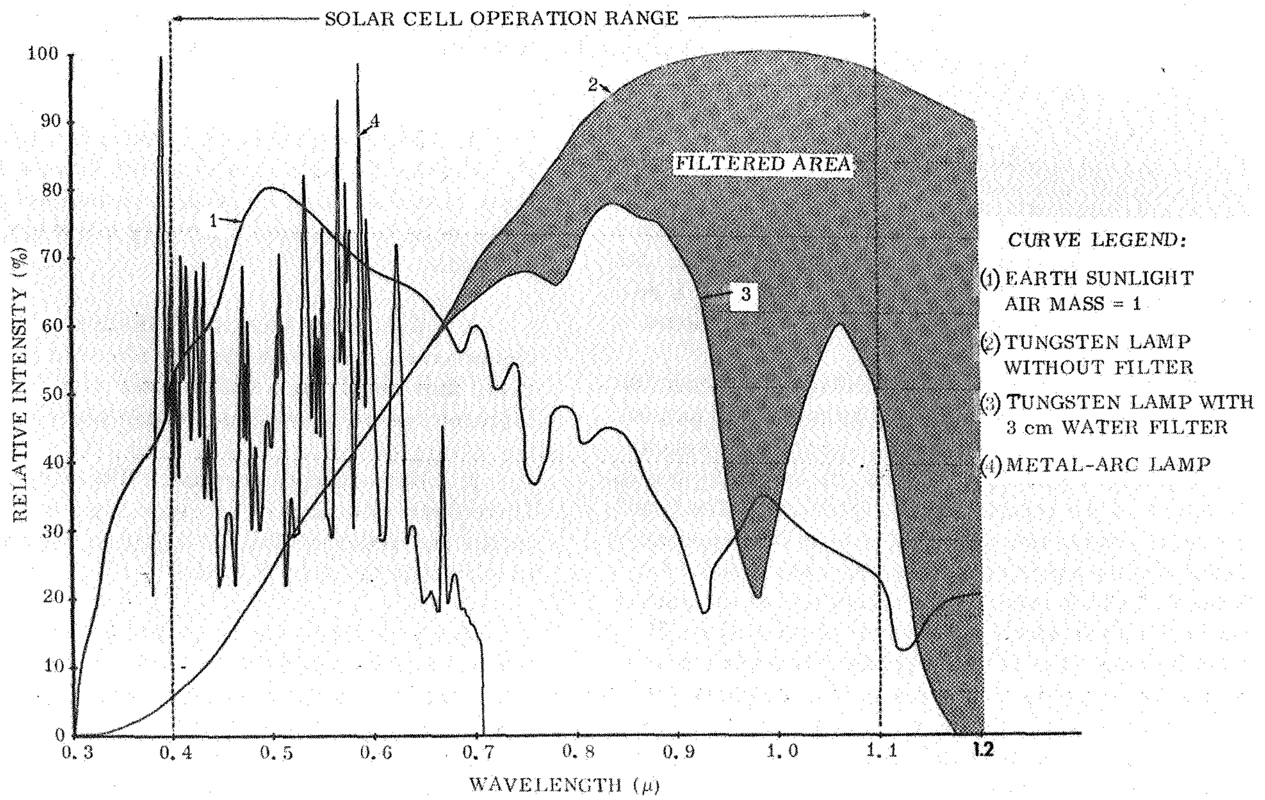

FIGURE 2. NORMALIZED SPECTRAL INTENSITY CURVES

the tungsten spectrum through 3 cm of distilled water. The spiked curve is the spectrum of the rare metal halide; the spikes represent the characteristics of the rare metal halide in its ionized state and are distinctive to the elements contained in the inner quartz envelope. The object is to simulate the "Air Mass 1" curve in the solar cell response region, which is also outlined in Figure 2.

Figures 3 and 4 show the lamps mounted for initial testing and are indicative of the early stages of development underway. Figure 3 shows a close-up of the five lamps used in the tests.

A secondary standard solar cell (Fig. 4), calibrated to a primary standard cell, is used to determine the magnitude and uniformity of intensity over the test plane area. Figure 5 shows the overall test set-up with the simulator in operation. This is done by using a digital voltmeter to measure the voltage drop across a one-ohm resistor to determine the short circuit current of the solar cell. The use of a one-ohm resistor enables the current to be read directly from the digital voltmeter. Since the short-circuit current of the cell is directly proportional to the intensity of the light impinging on its surface, it is only necessary to know the relationship between the short-circuit currents of the primary and secondary standards to determine the intensity of the light source. By moving the cell to various points on the test plane while observing the reading on the voltmeter, the uniformity of the intensity over the test plane area can also be determined.

An iron-constantan thermocouple temperature read-out device was used to determine the temperature of the secondary standard. Relatively constant temperature was maintained by circulating water through its base with a systaltic pump.

The ballasts required for each of the lights to establish the initial high arc and limit the current once it has been established are shown mounted on the sides of the simulator near the bottom (Fig. 5).

Although no specific attempt was made in these early tests to duplicate "Air Mass 1" intensities, or to establish uniform intensity over large areas, the five lamps shown produced 50% of the "Air Mass 1" intensity over an area 0.635 m × 0.635 m (25 in. ×

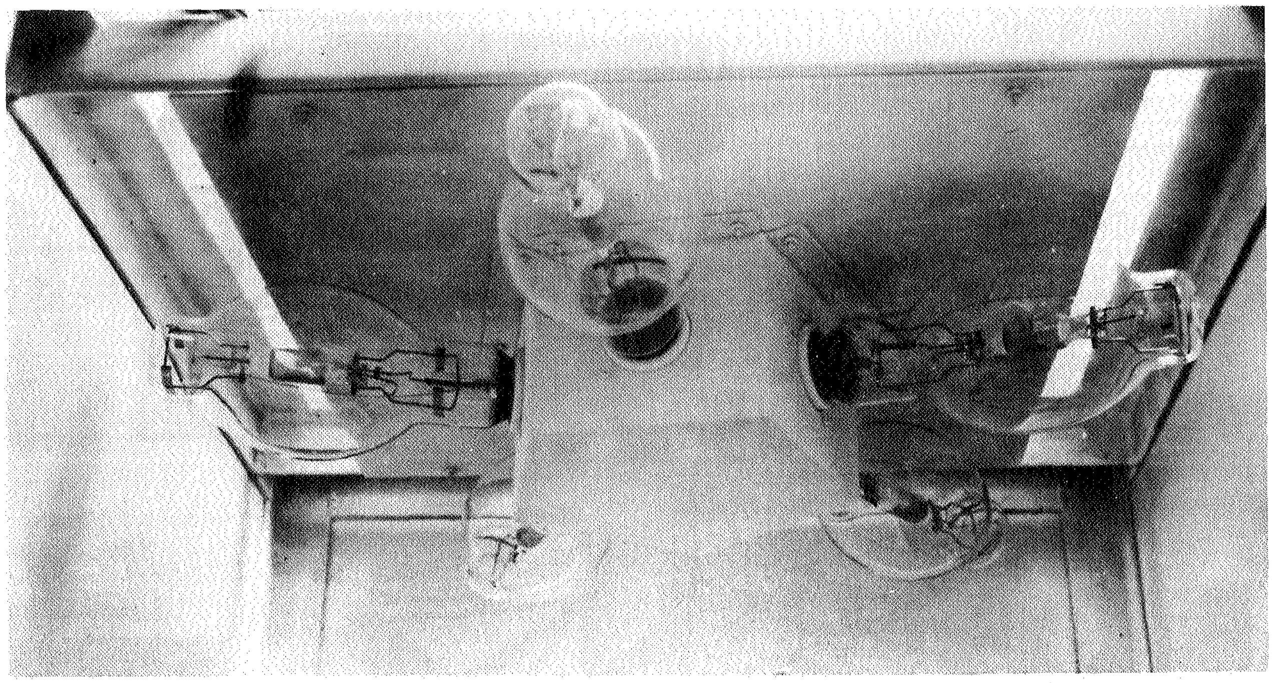

FIGURE 3. TUNGSTEN FILAMENT LAMPS

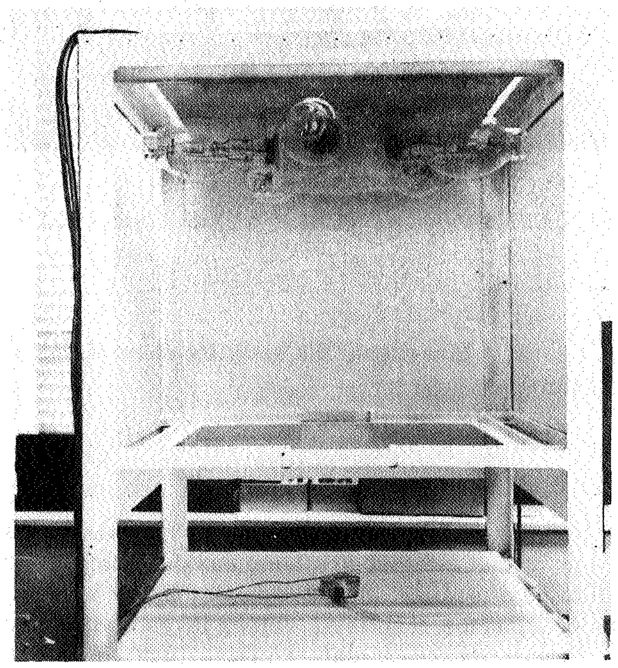

FIGURE 4. ILLUMINATION CHAMBER WITH SOLAR CELL

25 in.), with intensity gradients of ± 10%. No attempt was made to collimate the light during initial tests.

METAL-ARC LAMP SOURCE

Results of the present exploratory investigations indicate the following potential advantages of metal-arc:

1. Low heat generation at the lamp.
2. Reduced infrared radiation - eliminating the need for a water filter and the accompanying water cooling apparatus.
3. Increased radiation at shorter wave-lengths.
4. Long lifetime - The 7500 hr rated average lifetime of this source makes it particularly attractive for use in solar simulation.
5. Economy - The price of these lamps compares very favorably with that of tungsten lights because of their longer lifetime.

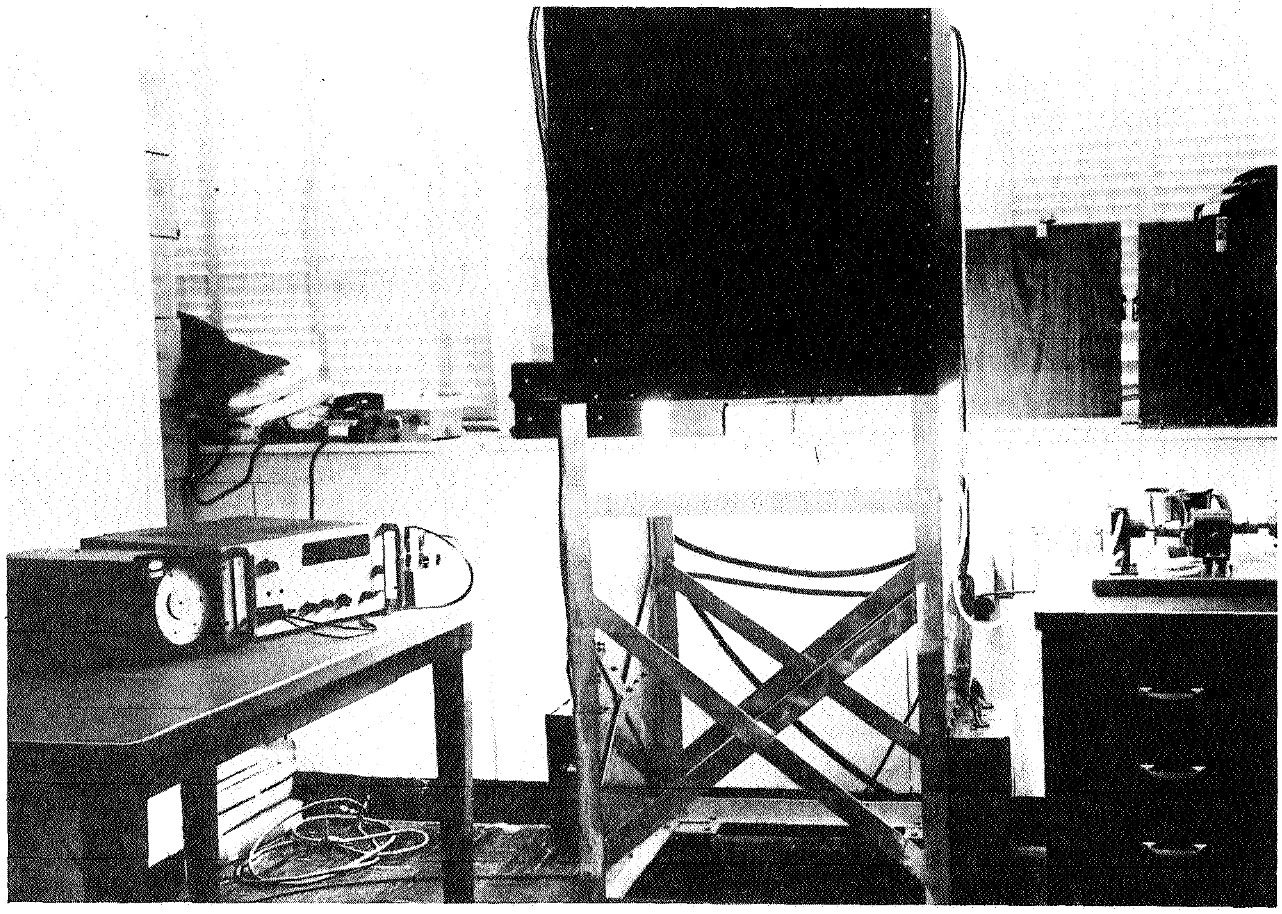

FIGURE 5. SOLAR ARRAY TEST METHOD USING ILLUMINATION SOURCE AND SOLAR CELLS

FUTURE PLANS

Future plans are as follows:

1. Obtain output in the 0.7 μ to 1.1 μ wavelength band to closer simulate the "Air Mass 1" curve in the solar cell response region. Sylvania, whose lamps were used for these tests, indicates that this is possible.

2. Illuminate an area 0.635 m × 0.635 m (25 in. × 25 in.) to "Air Mass 1" illumination level.

3. Reduce the intensity gradients at the test plane.

4. Investigate the stability of emission with time.

5. Investigate collimation.

Investigations have not yet proceeded to such a point that a metal-arc lamp can definitely be shown to be a feasible source for solar array testing. However, if the results of further investigations prove its feasibility, the metal-arc lamp could provide solar cell array design engineers with a source for array testing which is economical, has a long lifetime, and requires a minimum of auxiliary equipment for operation.

ELECTRICAL POWER CONVERSION SYSTEM FOR MANNED EARTH ORBITAL VEHICLE

By

Richard Acker

SUMMARY

An electrical power conversion system designed for a manned earth orbital vehicle is described. The mission considered is typical of future manned spacecraft flights.

INTRODUCTION

The design constraints established for the mission are listed in Table I. The spacecraft would be placed in a 481-km (260-nm) orbit oriented to the sun during the 18-month mission. The orbit period is 94 min (58 min of solar illumination and 36 min of earth occultation).

TABLE I. DESIGN CONSTRAINTS

- Solar Cell Array
  - Oriented to Sun
  - Temperature Range ~ 255 to 351°K
- Mission Length ~ 1 1/2 Years Maximum
- Orbital Period ~ 94 min
  - Night ~ 36 min
  - Daylight ~ 58 min
- Passive Cooling
- Electrical Loads ~ 3600 W Average
- No Single Point Failures
- Central Converters
- High Efficiency
- Minimum Weight
- Minimum Volume

The major spacecraft constraint is the requirement for passive cooling of the power system components. This constraint requires the electronic packages' view of space to be optimized as most of the heat must be dissipated by radiation. The resulting temperature is dependent upon the available radiating area. High power conversion and energy efficiencies are necessary to reduce the amount of heat generated.

Other constraints imposed on the power conversion system include minimum weight and volume, central converters, and no single point failure that will result in a system failure.

For the electrical load requirement of 3600 W average power, three types of power sources were considered: fuel cell, radioisotope thermoelectric generator (RTG), and solar cell array.

Fuel cell operation is limited by reactant storage and heat removal problems and by mission duration. Power systems of 2 to 4 kW capacity require an active coolant loop to remove the waste heat, and fuel cell systems with proven life capability of greater than 2000 hr are not yet available.

The RTG system has the limitations that fuel is not available for a large system and radiation danger to personnel could exist. The present RTG's are being developed with maximum power output capabilities of 500 W. Conversion efficiencies of approximately 5% demand active cooling.

A solar cell array sized electrically to 2-1/2 times the spacecraft load would be required to allow for charging secondary energy storage devices to supply power during earth occultation periods. Solar cells with proven performance and reliability are readily available, and the low earth orbit decreases degradation caused by energetic particle bombardment. Solar cells are particularly attractive on sun oriented missions because of the availability of 90 degree incident solar radiation without ancillary array pointing systems.

SELECTED POWER SYSTEM

The selected power system is depicted in Figure 1. The solar cell array is modular in design and, aside from cabling and bussing philosophy, each source is capable of operating independently of all others.

The charger/battery/regulator modules (CBRM) of the electrical power conversion system provide building block capability to make a flexible system that can be readily modified to accommodate changing power demands. The CBRM's are connected in parallel. Failure of a single module will cause the loss of only 1/N of the power conversion system and will not result in a system failure, thus satisfying the no single point failure requirement. Each CBRM will have individual overload protection in the form of current limited output. A droop characteristic in the CBRM output voltage will force all modules to share the load equally. Power available for charging the batteries will be shared by all batteries depending on individual charge requirements, and the battery chargers will provide power management by forcing the solar cell array to operate at or above a nominal 40 V. Protection, monitoring, and control circuits will be self-contained in each CBRM.

SOLAR CELL ARRAY OUTPUT CHARACTERISTICS

The solar cell array (Fig. 2) is required to supply 9 kW average power during daylight periods to maintain the electrical power conversion system output of 3.6 kW average power over the entire orbit. The array is divided into forty 225 W sources that are individually diode coupled to the solar cell bus. The loss of any one source (from micrometeoroid damage, cable damage, etc.) will cause a total power loss of 2-1/2%.

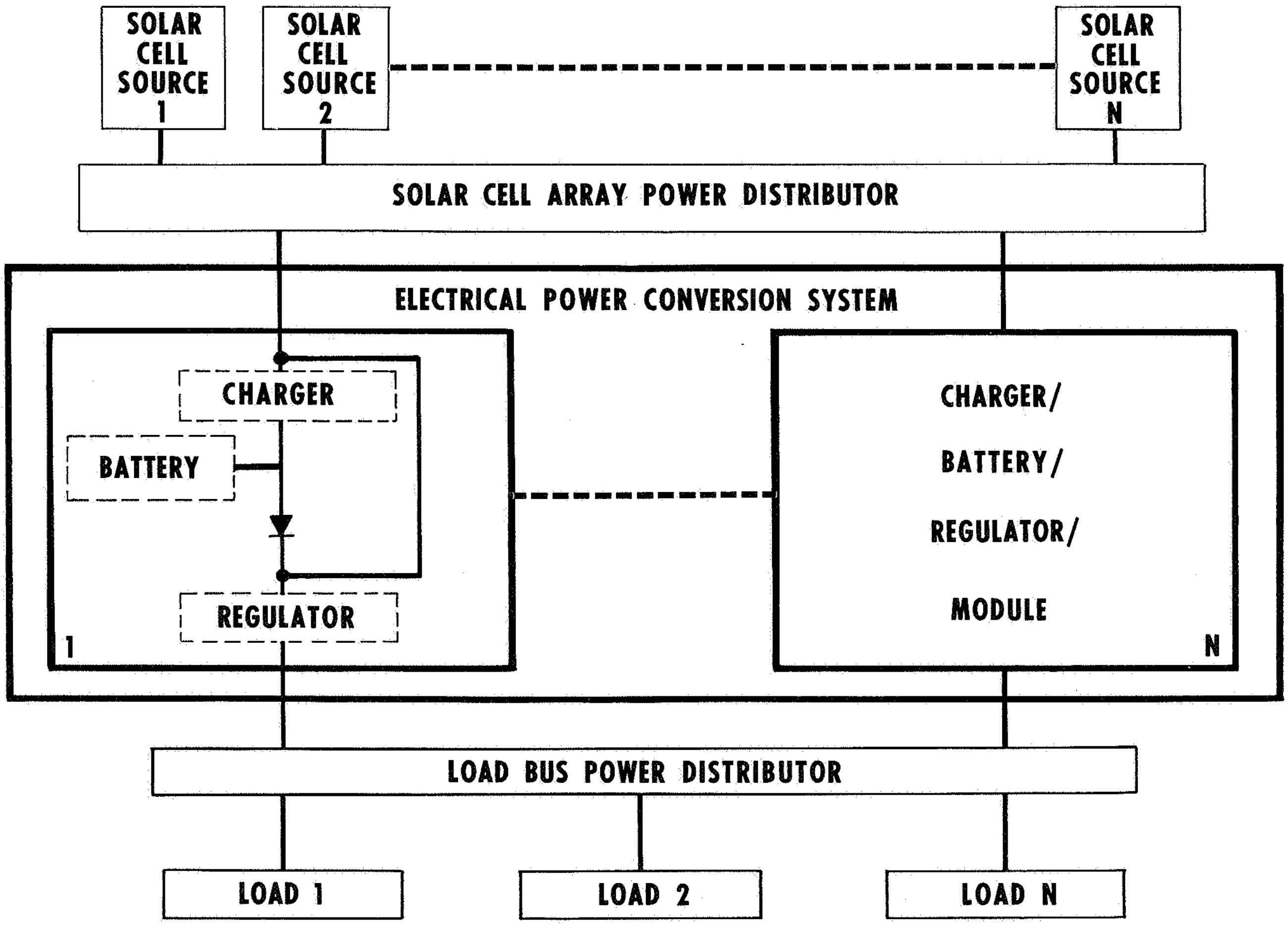

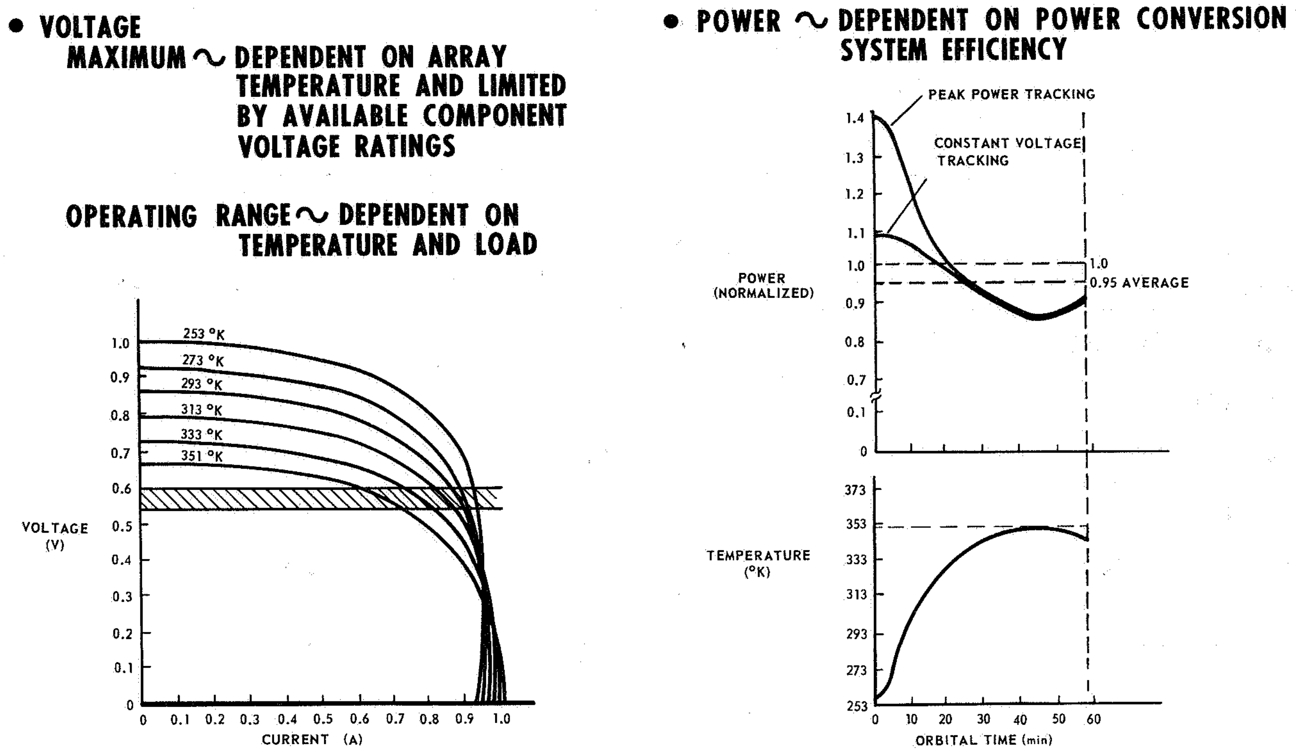

V-I CURVE NORMALIZED

POWER vs. TEMPERATURE NOMOGRAPH

FIGURE 2. SOLAR CELL ARRAY OUTPUT CHARACTERISTICS

The maximum output voltage for the solar cell array is dependent upon array temperature, and the array must be designed to limit this voltage to component voltage ratings. The operating voltage range is dependent upon temperature and electrical load.

The electrical power available for battery charging and spacecraft loads is dependent upon the power conversion system efficiency. The large area of the array precludes the use of peak-power point tracking because of temperature gradients across the array at any point in time. The battery charge rate is automatically controlled to force the array to operate at or above a constant voltage, which approximately coincides with the peak-power point at a chosen temperature. Constant voltage tracking utilizes 95% of the available solar cell array power as shown in Figure 2.

LOAD REGULATOR CIRCUIT COMPARISON

Three basic types of switching regulators and their comparative characteristics are shown in Figure 3. The step-up or -down type was chosen because it possessed inherent characteristics of (1) being able to operate with an input voltage below or above the output voltage, (2) source-load isolation, (3) absence of single point system failure (a single failure will not damage load or remaining regulators), (4) load current limiting, and (5) a respectable conversion efficiency.

The step-down regulator was chosen for the battery charger because high efficiency was the primary consideration. A shorted switching transistor, which would apply the normally high input

	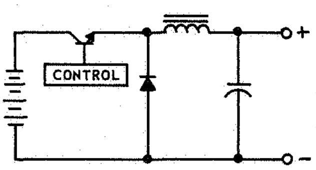	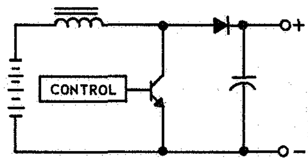	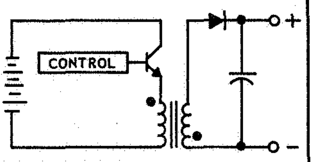
TYPE	**STEP-DOWN**	**STEP-UP**	**STEP-UP OR-DOWN**
SINGLE POINT FAILURE	**YES**	**NO**	**NO**
OVERLOAD PROTECTION	**YES**	**NO**	**YES**
INPUT VOLTAGE	**HIGH**	**LOW**	**HIGH OR LOW**
ISOLATION	**NO**	**NO**	**YES**
POWER (PER UNIT)	**1**	**1**	**0.5**
EFFICIENCY	**95**	**93**	**88**

FIGURE 3. LOAD REGULATOR CIRCUIT COMPARISON

voltage to the load, is effectively decoupled by the battery and the load regulator; therefore, the single point failure that would exist if the circuit were used for the load regulator would not apply to the battery charger.

SECONDARY BATTERY

The only proven secondary battery available with cycle life and capacity necessary for an 18-month mission is the nickel cadmium unit (Fig. 4). This battery is capable of operating for the required 8,400 cycles with its twenty-four, 20 A-hr cells connected in series.

- Battery Cycle Life Requirements ~ 8,400 Cycles
  Nickel Cadmium Selected ~ Twenty-Four,
  20 A-hr Cells per Battery
  At 298°K Battery Center Temperature and 10 A Charge Rate
- Energy Efficiency
  With Third Electrode ~ 80%
  Without Third Electrode ~ 64%
- Ampere-Hour Charge/Discharge Ratio
  With Third Electrode ~ 1.14
  Without Third Electrode ~ 1.41

FIGURE 4. SECONDARY BATTERY

Individual cell third electrodes are used to indicate the battery recharge state. The voltage potential at the third electrode rises sharply as the battery reaches a state of full charge, thus giving an accurate indication of the battery having reached its full capacity. This allows the charge to be terminated before the overcharge region is reached where a large portion of the electrical charging energy would be transformed into heat energy. With third electrode control, the energy efficiency is approximately 80% and the ampere-hour charge to discharge ratio is approximately 1.14, as opposed to control without third electrode with an energy efficiency of 64% and a charge to discharge ratio of 1.41.

CHARGER / BATTERY / REGULATOR MODULE

Figure 5 is a functional schematic of the CBRM showing the battery charger and load regulator characteristics. The battery charger performs a power management function by using only that power for battery charging that is not demanded by the load.

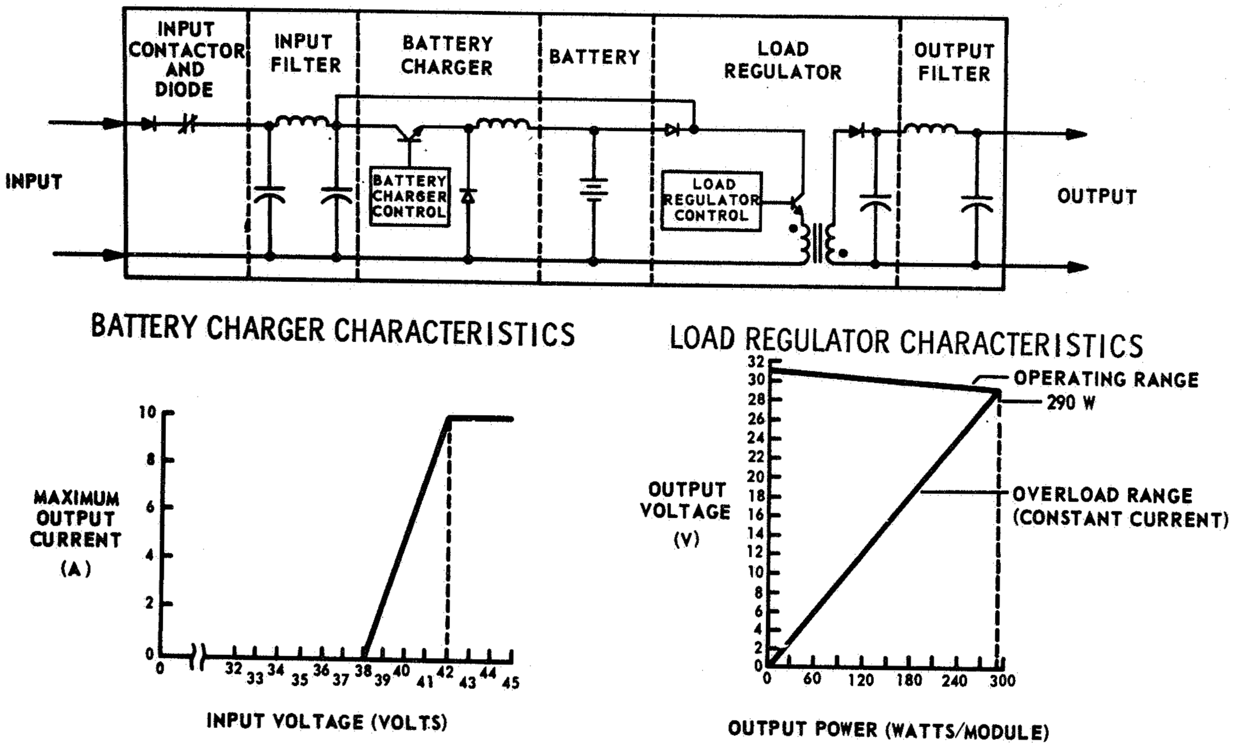

FIGURE 5. CHARGER/BATTERY/REGULATOR MODULE

The battery charger will be a step-down switching regulator, selected because of its high efficiency. The four signals used to control the battery charger are the module input voltage (solar cell array voltage), battery current, battery voltage as a function of temperature, and third electrode signal as a function of battery charge state.

The charger will charge the battery at a constant current until the battery terminal voltage reaches a predetermined level which is a function of battery temperature. The constant current level is 10 A when the solar cell array input voltage is greater than 42 V. At or above this voltage, enough power is available to charge the battery at 10 A and also supply the load. If the load increases substantially, the solar cell array voltage will drop below 42 V and the battery charger will limit the charge current to less than 10 A. At 38 V the battery charger will turn off, thus allowing the load regulator to supply all available power to the load. This sloping battery charger characteristic insures adequate power to the spacecraft's electrical loads. At the constant current charger cut-off point, the charger will commence charging the battery at a constant voltage, modified by battery temperature, until the third electrode signal level reaches a preselected level. When the selected third electrode potential is reached, the charger will cut off and remain off until reset. During the battery discharge period (earth occultation), the solar cell array voltage will drop below 38 V, resetting the charger for the next charge cycle.

The load regulator will be a step-up or -down switching regulator with an isolation transformer to isolate input from output. This configuration combines high efficiency with overload protection and maximum overvoltage protection to the output. Because of possible damage to the loads, a primary design goal is to hold the output voltage below 32 Vdc. The regulator will control the output voltage from 31 Vdc at no load to 29 Vdc at a full load of 10 A. The output voltage is controlled by feedback signals from the output voltage and current. The output voltage slope from 31 to 29 Vdc forces all CBRM's to share in supplying the spacecraft's electrical loads. In the event one regulator would attempt to supply a relatively larger amount of current than the others, its output voltage to the load bus would decrease and the other regulators would assume a proportionate share of the load.

POWER CONVERSION EFFICIENCY

The electrical parameters used to calculate the efficiency of the electrical power conversion system are given in Figure 6. Assuming 200 W per CBRM, 18 modules will be required to supply the spacecraft's electrical load of 3600 W. Using conversion efficiencies of 95% for the battery charger and 88% for the load regulator and an energy efficiency of 79.8% for the battery, the CBRM energy conversion efficiency is 70.2%. Allowing for distribution and decoupling losses, this conversion efficiency is 64.8% for the complete electrical power system. A solar cell array to spacecraft electrical load power ratio of 2.5 is achieved.

ELECTRICAL POWER CONVERSION SYSTEM SUMMARY

A summary of the electrical power conversion system characteristics and load handling capabilities is given in Figure 7. Eighteen CBRM's operating from a solar cell array of 9 kW average (58 min of a 94 min orbit) will supply a continuous spacecraft electrical load of 3600 W. A peak average daylight load of 5.22 kW (limited by load regulator maximum power output) can be supplied. For the batteries to be completely recharged within one orbit, this day load must be accompanied by a night load not exceeding 1.93 kW average power usage. The maximum discharge the battery receives is 26%, thus enhancing long battery life. For a mission of shorter duration requiring an average load of 3600 W, the number of CBR modules could be reduced by increasing the power output capability of each regulator and allowing for greater drain on the battery.

- NUMBER OF CBR MODULES REQUIRED . . . 18
- INPUT:
  - SOLAR ARRAY VOLTAGE . . . . 40-75 Vdc
  - SOLAR ARRAY POWER (P_{SA}) . . . . 9 kW AVERAGE (58 min/94 min ORBIT)
- BATTERY: MAXIMUM DISCHARGE 26%
- OUTPUT:
  - VOLTAGE
    - STEADY STATE. . . . . 29-31 Vdc
    - RIPPLE . . . . 0.1V_{PK-PK} MAX. @5-10 kHz
  - POWER
    - PEAK. . . . . 5.22 kW

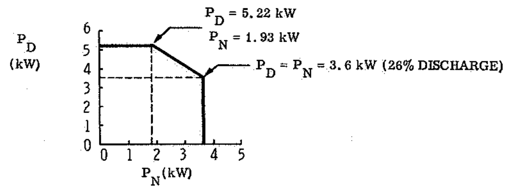

AVERAGE LOAD/ORBIT NOMOGRAPH

FIGURE 7. ELECTRICAL POWER CONVERSION SYSTEM SUMMARY

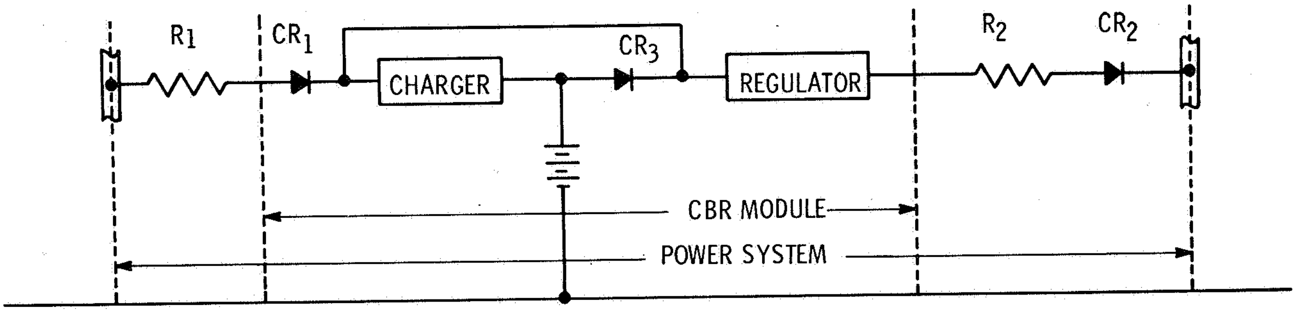

SYSTEM PARAMETERS

- 200 W/MODULE
- POWER CONVERSION EFFICIENCY - CHARGER ~ 95%, REGULATOR ~ 88%
- 24 CELL BATTERY
- $R_1 = 0.1\ \Omega$
- $R_2 = 0.05\ \Omega$
- $V_{CR1} = V_{CR2} = V_{CR3} = 1$ V DROP

SYSTEM ENERGY CONVERSION EFFICIENCY

- POWER SYSTEM ~ 64.8%
- CBR MODULE ~ 70.2%

POWER RATIO P_{SA}/P_O

- POWER SYSTEM ~ 2.5
- CBR MODULE ~ 2.3

FIGURE 6. POWER CONVERSION EFFICIENCY

INVERTERS FOR MOTORS

By

Roy Lanier

SUMMARY

Electric motors are used in many space vehicle systems. A comparison is made of several typical motors used to power auxiliary equipment up to 1.5 kW, and the advantages and disadvantages of each type motor are mentioned. The inherent simplicity and reliability of the ac induction motor are recognized and methods of overcoming its disadvantages are discussed. The development of inverters to drive ac induction motors, and techniques used to provide desired performance are described. Incorporation of these techniques makes the reliable ac induction motor ideal for most motor applications.

INTRODUCTION

A demand exists for reliable, long life motors to power the auxiliary equipment used in launch vehicles and spacecraft. Several types of electric motors are available for use in pumps, blowers, positioners, traction drives, tracking drives, and general drives. The requirements for motors for these applications vary with the specific load characteristic, but some general requirements are listed in Table I.

TABLE I. ELECTRIC MOTOR REQUIREMENTS

Supply Voltage	28 to 56 Vdc
Power Output	1 to 1500 W
Operating Life	Up to 10,000 hr
Speed	Constant or variable
Efficiency	High over wide speed range
Starting Torque	High
Surge Current	Limited
Motor Rotation	Reversal required
Environmental Operation	Vacuum, high temperature, low temperature, vibration

Generally an electric motor is selected based on the system requirements. Quite often this results in compromises in one or more areas. These compromises can be largely overcome by selecting a 3-phase ac squirrel cage induction motor with the proper power supply inverter as described in this paper.

COMPARISON OF MOTORS

Three types of electric motors widely used in the drive applications are the conventional (brush type) dc motor, the brushless (permanent magnet, electronically commutated) dc motor, and the inverter supplied squirrel cage ac induction motor. The commutator and brushes of a conventional dc motor severely limit its use since most of the applications require operation in a vacuum and/or in a severe vibration environment. The permanent magnet brushless dc motor can be designed to overcome these disadvantages. However, it has the disadvantages of being more complex and of having a permanent magnet rotor that may be demagnetized. The squirrel cage ac induction motor is the most rugged and reliable motor of the three, having neither the brushes and commutator nor the permanent magnet rotor. In the past, the induction motor, although more rugged, has been limited to the relatively low starting torque, constant speed applications when high efficiency was required. However, by using an inverter capable of sensing and controlling various motor parameters such as drive frequency, voltage, and current, the induction motor may be preferred for most applications. Sensing and control of the various parameters and the expected results are discussed in the following section.

INVERTER DRIVEN AC INDUCTION MOTOR

Even though the starting current is high, a basic ac induction motor designed for high efficiency has characteristics of relatively low starting torque and relatively constant operating speed. This is shown later in the speed-torque curve for a conventional ac induction motor. An inverter design capable of driving the motor in such a manner as to overcome these deficiencies plus provide the capability of motor reversal is the goal of this effort as described in the following.

A 3-phase inverter output stage with its transistor switching sequence is shown in Figure 1. The circuit shows a method of connecting a motor directly across

TRANSISTOR SEQUENCING

Q1	ON	ON	OFF	OFF	OFF	OFF
*Q2	OFF	OFF	OFF	ON	ON	OFF
Q3	OFF	OFF	ON	ON	OFF	OFF
*Q4	ON	OFF	OFF	OFF	OFF	ON
Q5	OFF	OFF	OFF	OFF	ON	ON
*Q6	OFF	ON	ON	OFF	OFF	OFF

0 60 120 180 240 300 360
PORTION OF CYCLE-DEGREES

*TRANSISTORS SWITCHED OFF AND ON DURING CONDUCTION TIME TO PROVIDE MODULATION

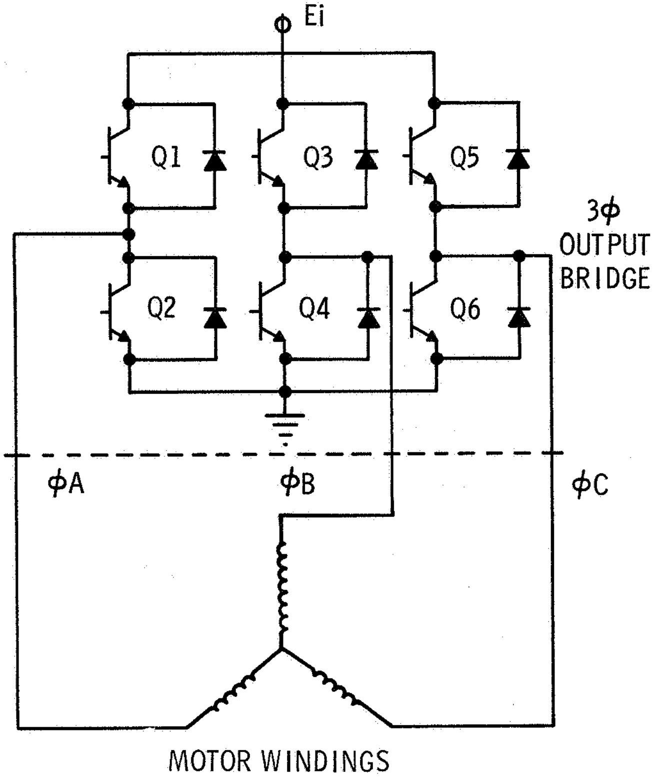

FIGURE 1. TYPICAL 3-PHASE OUTPUT BRIDGE AND MOTOR WINDINGS WITH TRANSISTOR SEQUENCING

a low voltage dc supply (28-56 V) without using a transformer, thus saving weight and improving efficiency and reliability. Transistors Q_2, Q_4, and Q_6 may be rapidly switched off and on during their conduction phases to provide efficient voltage control.

Figure 2 shows the control parameters used and the resulting voltage waveforms. The average voltage across the motor windings will be raised or lowered as the commutation off-time is decreased or increased, respectively. Thus with the necessary inputs to

CONTROL PARAMETERS

CONDUCTION TIME THUS ADJUSTING EFFECTIVE VOLTAGE

WAVEFORM PERIOD THUS ADJUSTING FREQUENCY

SWITCHING SEQUENCE THUS CHANGING DIRECTION OF MOTOR ROTATION

MOTOR WAVEFORMS

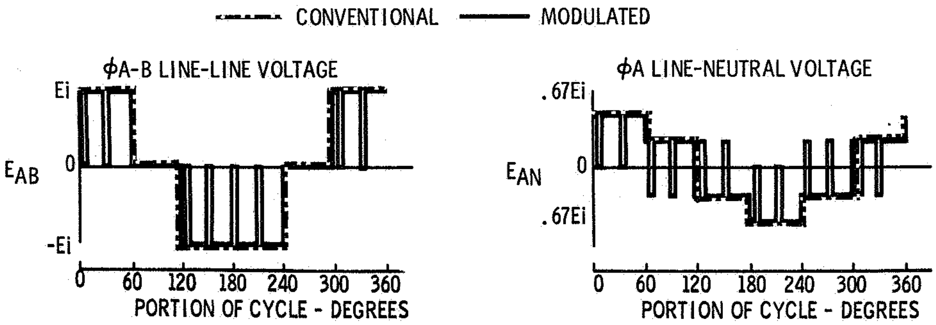

FIGURE 2. TYPICAL CONTROL PARAMETERS AND MOTOR WAVEFORMS

the 3-phase inverter bridge transistors, the effective voltage to the motor may be varied efficiently, the drive frequency to the motor may be changed by varying the cycle period, and the direction of rotation may be altered by varying the phase sequence. Proper use of this flexibility will result in the desired characteristics.

Figure 3 is a block diagram of an inverter driven ac induction motor with a current limiting feature. The curves show a typical transistor current peak with and without this feature. The oscillator, 3-phase logic, power source, and 3-phase power amplifier are typical for any inverter application. The current detector senses the input current from the power source and controls the voltage applied to the motor by modulating the 3-phase power amplifier and inverter bridge transistors as previously discussed. The result of the operation through the 3-phase logic is to reduce the voltage to prevent a peak current from being exceeded. The peak current is limited to protect the power transistors or the power supply.

Figure 4 is a block diagram of an inverter driven ac induction motor with a high starting torque. The torque speed curve of a conventional, single frequency driven motor and that of a slip frequency controlled motor are shown. In an efficient conventional motor the relative torque is low at zero speed (slip frequency equals operating frequency).

The starting torque per phase of a polyphase ac induction motor is:

$$T_{st} = \frac{K_1 p \, I_2^2 \, r_2}{4\pi \, f_1} \qquad (1)$$

where T_{st} = starting torque per phase
p = number of poles
I_2 = rotor current per phase
r_2 = effective rotor resistance per phase
f_1 = applied frequency
K_1 = a constant.

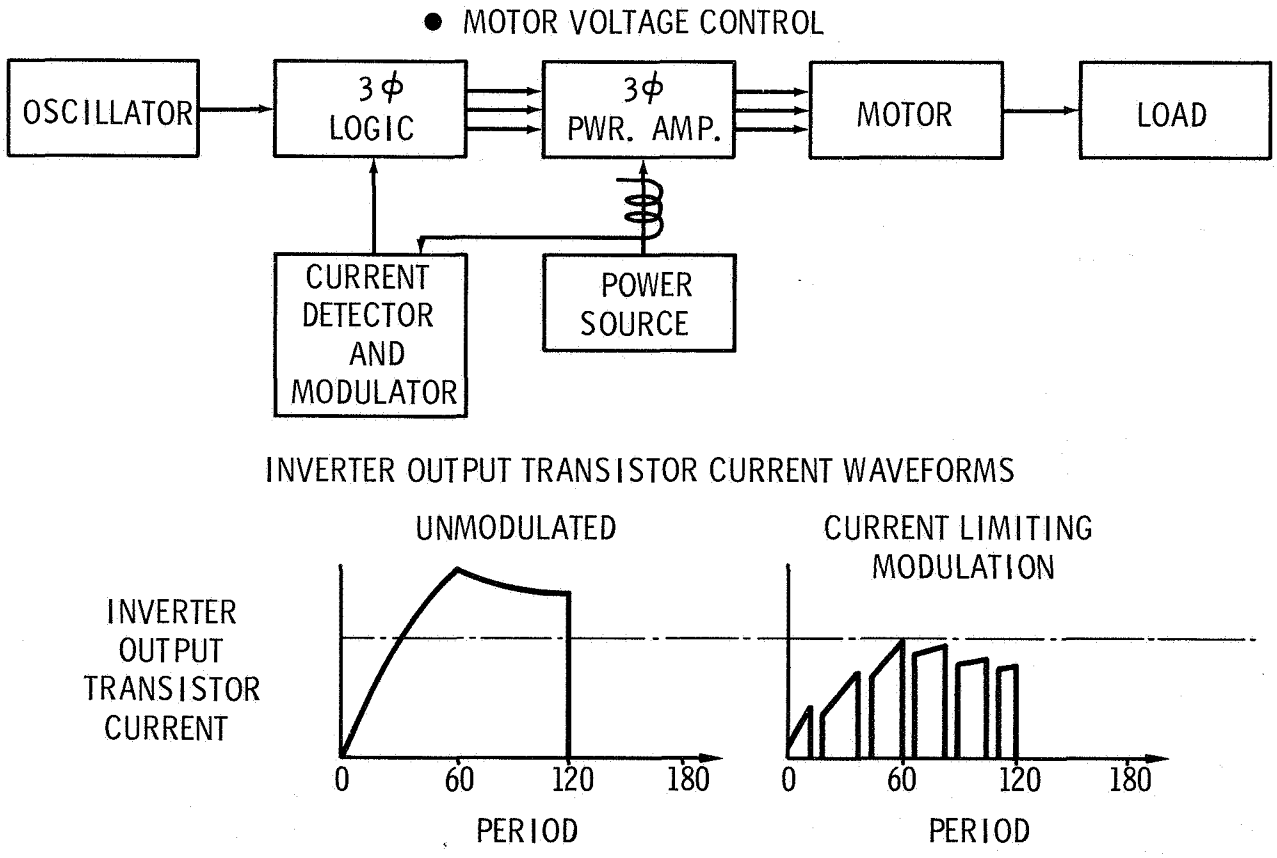

FIGURE 3. MOTOR - INVERTER SYSTEM FOR OBTAINING CURRENT LIMITING

• SLIP FREQUENCY CONTROL

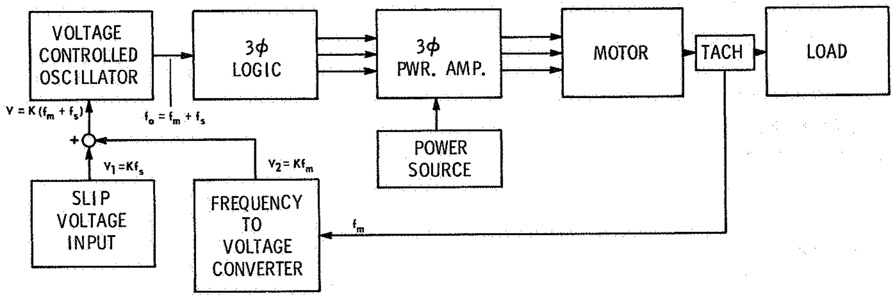

SPEED-TORQUE CURVES OF CONVENTIONAL AND SLIP FREQUENCY CONTROLLED AC INDUCTION MOTORS

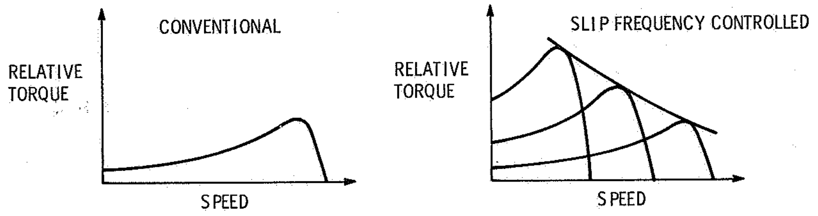

FIGURE 4. MOTOR-INVERTER SYSTEM FOR OBTAINING HIGH STARTING TORQUE

Equation 1 will reduce to

$$T_{st} = K_2 I_2^2/f_1 \qquad (2)$$

where K_2 = a constant for a given motor because the number of poles and rotor resistance are fixed.

Equation 2 shows that the starting torque of a motor may be controlled by controlling either of two parameters, rotor current or applied frequency. However, from an approximately equivalent circuit of an induction motor (neglecting the exciting current), the rotor current in terms of applied voltage at start is

$$I_2 = \frac{V_1}{\sqrt{(r_1 + r_2)^2 + 4\pi^2 f_1^2 (\chi_1 + \chi_2)^2}} \qquad (3)$$

where V_1 = applied voltage
r_1 = stator resistance
r_2 = rotor resistance reflected to the stator
χ_1 = stator reactance
χ_2 = rotor reactance reflected to the stator

The rotor current is then a function of both the applied voltage and the frequency, increasing with increasing voltage and decreasing frequency. Some practical lower frequency limit must be recognized because of magnetic circuit considerations. In addition, a maximum current limit must be recognized based on winding size and thermal considerations and/or inverter power transistors. This maximum current is observed by reducing the voltage as previously discussed or by reducing the source voltage which is normally constant. By decreasing the applied frequency, the motor will be forced to start at a lower slip frequency. As previously shown, frequency, although constant in many systems, is a parameter that may be conveniently controlled in an inverter. The circuit shown in Figure 4 provides the capability of obtaining a voltage proportional to the motor rotational frequency, f_m, and adding it to a voltage proportional to the desired slip frequency, f_s, selected on the basis of motor characteristics and load requirements. The sum of these voltages is proportional to the frequency required to drive the motor at f_m with the desired slip frequency at that instant. By using this voltage sum as the input to the voltage controlled oscillator, an output frequency, f_o, is obtained to drive the motor after proper logic operation. This forces the motor to operate at a frequency only slightly above its running frequency, even at start, thus assuring a high relative starting torque. Typically the frequency may be decreased to as little as one tenth the normal operating frequency, giving a starting torque of approximately ten times normal starting torque and up to five times rated load torque for a typical conventional motor. Equation 3 gives the relationship of applied voltage, frequency, and rotor current, and shows that there is an integral relationship among the three. Thus the feedback control of frequency and voltage are interrelated and require careful consideration for each case. However, with proper consideration, a torque-speed characteristic to match any practical load may be obtained, as may be deduced from this discussion and the curve shown in Figure 4. Work is continuing in this area.

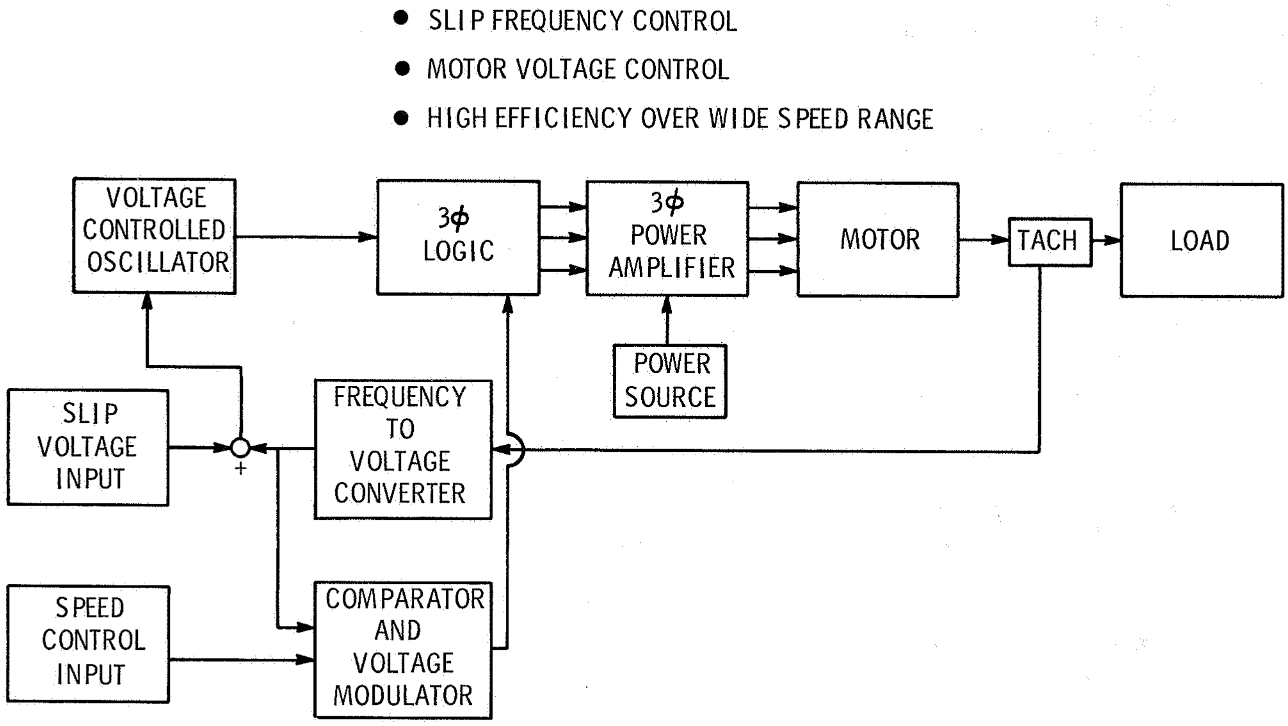

FIGURE 5. MOTOR - INVERTER SYSTEM FOR OBTAINING SPEED CONTROL

Figure 5 is a block diagram of an inverter driven ac induction motor capable of efficient operation over a wide range of speed. The operation is similar to that of the slip frequency controlled circuit in Figure 4, except an additional input to the 3-phase logic to provide voltage modulation is provided. This method may be used to provide a constant or multi-speed characteristic by furnishing one or more reference inputs to the comparator and voltage modulator, which in turn will generate the necessary digital signal input to the 3-phase logic to vary the voltage at any time an error between the actual and desired frequencies or speeds exists. However, its chief advantage would be the capability of operating at high efficiencies over a wide range of speed, thus making it desirable for traction drive applications.

A block diagram of an inverter driven ac induction motor with motor reversal capabilities is shown in Figure 6. The logic diagram shows a method of changing the phase sequence from A-B-C to B-A-C, thus reversing the motor rotation. The most important feature of this straightforward method is that the reversal is accomplished at a very low power level by operating on the low-level logic.

Figure 7 is a block diagram of a typical inverter driven ac induction motor system incorporating all of the features discussed. The system is capable of developing a high starting torque to current ratio, possesses a high efficiency over a wide range of speed, and has remote control of rotation direction and speed, torque or power.

FUTURE EFFORTS

Although all of the techniques discussed have been shown to be technically feasible, much work remains to be done to produce operational systems. Proper frequencies, modulation methods, materials, etc., must be determined to obtain optimum use of available capabilities. Most work to date has been with small (100 W) motors. Future efforts will develop capabilities in systems using motors with ratings up to 1.5 kW. In addition, the following efforts are planned for the future:

1. Continue investigation of inverter and control techniques.

2. Define detailed inverter configuration for various load requirements.

3. Define desired motor characteristics for various load requirements.

4. Design inverters for higher power applications.
5. Determine design criteria for various environmental considerations.
6. Investigate electronic components to determine proper characteristics for motor drive applications.
7. Design inverter control elements using integrated circuits for compactness and reliability.

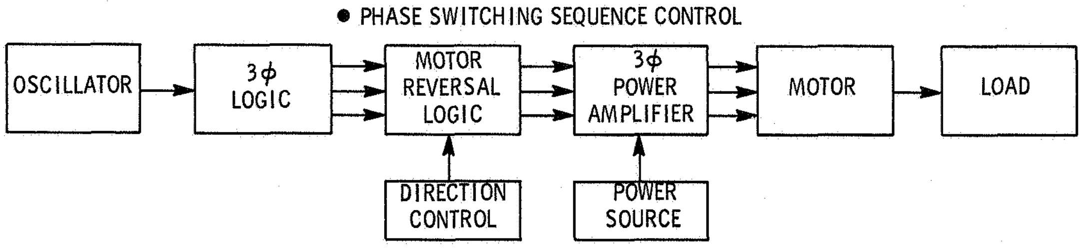

LOGIC DIAGRAM OF MOTOR REVERSAL BLOCK

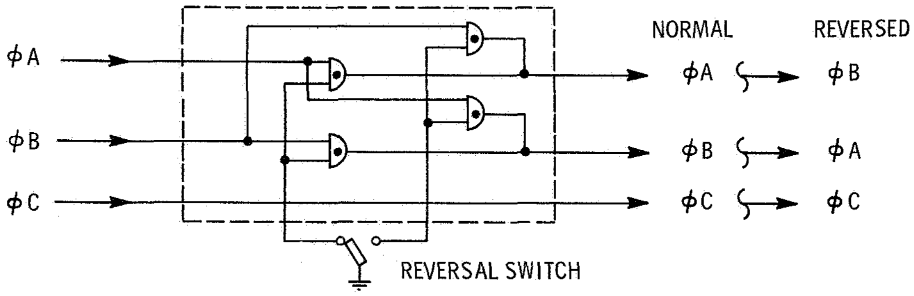

FIGURE 6. MOTOR - INVERTER SYSTEM FOR OBTAINING MOTOR REVERSAL

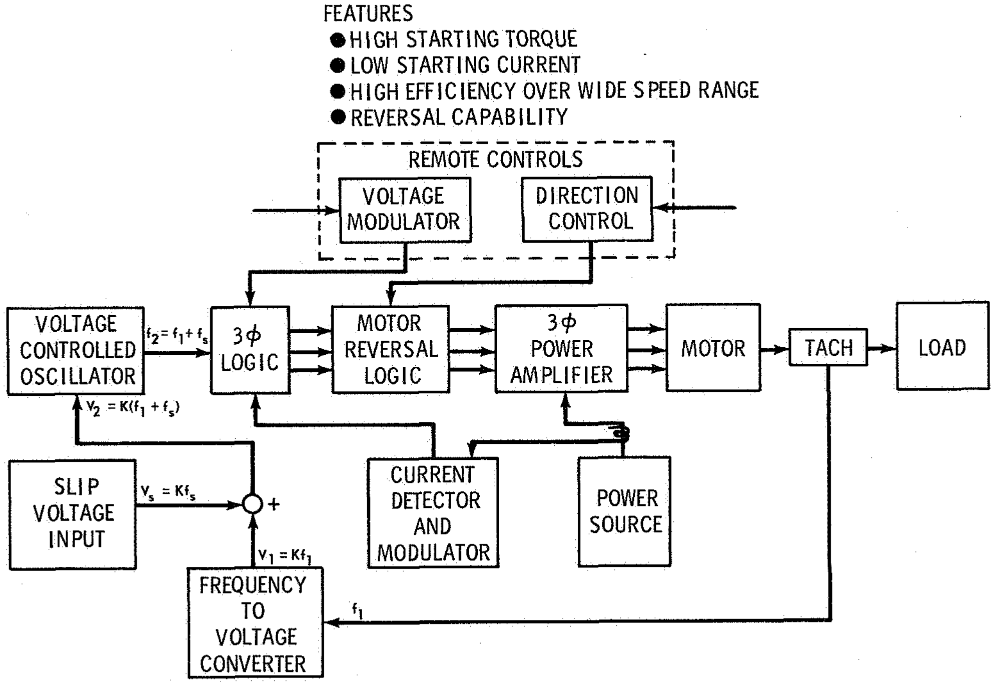

FIGURE 7. TYPICAL MOTOR - INVERTER SYSTEM